

AD-A078 678

WISCONSIN UNIV-MADISON
REMOTE MEASUREMENTS OF BOUNDARY LAYER VELOCITY PARAMETERS BY MO--ETC(U)
OCT 79 J T SROGA

F/G 17/8

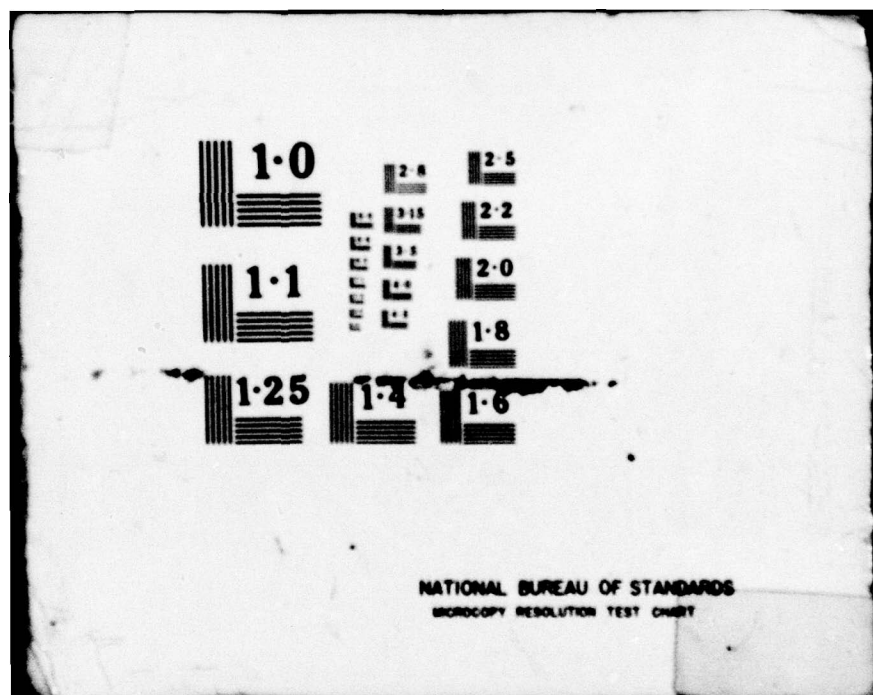
DAAG29-76-C-0136

ERADCOM/ASL-CR-79-0136-1 NL

UNCLASSIFIED

1 OF 2
AD-
A078678





ASL-CR-79-0136-1

AD

Reports Control Symbol
OSD 1366

12

ADA 078678

LEVEL
**REMOTE MEASUREMENTS OF BOUNDARY LAYER
VELOCITY PARAMETERS BY MONOSTATIC LIDAR**

OCTOBER 1979



Prepared by
JEFFERY THOMAS SROGA

University of Wisconsin
Madison, WI 53706

Under Contract DAAG-29-76-C-0136
CONTRACT MONITOR: TED BARBER

Approved for public release; distribution unlimited

DDC FILE COPY



US Army Electronics Research and Development Command
ATMOSPHERIC SCIENCES LABORATORY
White Sands Missile Range, NM 88002

79 12 20 012

NOTICES

Disclaimers

The findings in this report are not to be construed as an official Department of the Army position, unless so designated by other authorized documents.

The citation of trade names and names of manufacturers in this report is not to be construed as official Government endorsement or approval of commercial products or services referenced herein.

Disposition

Destory this report when it is no longer needed. Do not return it to the originator.

SECURITY CLASSIFICATION OF THIS PAGE (When Data Entered)		READ INSTRUCTIONS BEFORE COMPLETING FORM	
REPORT DOCUMENTATION PAGE			
1. REPORT NUMBER ASL-CR-79-0136-1		2. GOVT ACCESSION NO.	
4. TITLE (and subtitle) REMOTE MEASUREMENTS OF BOUNDARY LAYER VELOCITY PARAMETERS BY MONOSTATIC LIDAR		5. TYPE OF REPORT & PERIOD COVERED Technical Report	
7. AUTHOR(s) Jeffery Thomas Sroga		8. CONTRACT OR GRANT NUMBER(s) DAAG-29-76-C-0136	
9. PERFORMING ORGANIZATION NAME AND ADDRESS University of Wisconsin Madison, WI 53706		10. PROGRAM ELEMENT, PROJECT, WORK UNIT NUMBER DA Task 1T161102BH37	
11. CONTROLLING OFFICE NAME AND ADDRESS US Army Electronics Research and Development Command Adelphi, MD 20783		12. REPORT DATE Oct 1979	
13. MONITORING AGENCY NAME & ADDRESS (if different from Controlling Office) Atmospheric Sciences Laboratory White Sands Missile Range, NM 88002		14. NUMBER OF PAGES 115	
16. DISTRIBUTION STATEMENT (of this Report) Approved for public release; distribution unlimited		15. SECURITY CLASS. (of this report) UNCLASSIFIED	
17. DISTRIBUTION STATEMENT (of the abstract entered in Block 20, if different from Report) CR-79-0136-1		18. DECLASSIFICATION/DOWNGRADING SCHEDULE	
18. SUPPLEMENTARY NOTES Contract Monitor: Ted Barber			
19. KEY WORDS (Continue on reverse side if necessary and identify by block number) Meteorology Boundary layer Lidar Turbulence Remote wind Aerosols			
20. ABSTRACT (Continue on reverse side if necessary and identify by block number) Wind velocity parameters in the planetary boundary layer are measured using spatial inhomogeneities in the natural aerosol content as tracers. Lidar measurements of these spatial inhomogeneities are correlated in time and space to remotely estimate the mean speed, direction and the rms speed variance of the wind velocity. Aerosol inhomogeneities with horizontal dimensions of 60m-0.1km were found to be efficient tracers of the wind. The coherence between spatially and temporally separated lidar profiles of these spatial			

20. ABSTRACT (cont)

aerosol inhomogeneities is used to determine the perpendicular components along and across the beam pattern of the horizontal wind velocity. The decrease in coherence with increasing time and spatial separation is used to estimate the rms windspeed over the wavenumber region $.001^{(m^{-1})} - .07(m^{-1})$. Comparisons between lidar horizontal wind measurements with tower anemometers and pilot balloons show that lidar can remotely sense the boundary layer flow.

Accession For	
NTIS GRA&I	<input checked="" type="checkbox"/>
DDC TAB	<input type="checkbox"/>
Unknown and	<input type="checkbox"/>
Justification	<input type="checkbox"/>
By	
Dis	
Ave	
Dist	Mailed or Special
A	

Acknowledgements

I would like to express my appreciation to Professor James A. Weinman for his support, encouragement and suggestions during this study. I wish to thank Professors John A. Young and Charles R. Stearns for their helpful suggestions during the preparation of this manuscript. I would also like to thank Dr. Kenneth E. Kunkel for many discussions on this subject.

Dr. Scott T. Shipley deserves a special thanks for his moral encouragement and numerous helpful suggestions during the analysis and writing of the thesis.

Dr. Edwin W. Eloranta should be singled out for his contributions to this work. Most of the ideas presented in this thesis originated with him, and through his work and direction, the measurements by the U.W. lidar system were made possible. At all times, Ed played the "devil's advocate", questioning all aspects of this study. His interest and enthusiasm for this project is greatly appreciated.

I would also like to express my sincere gratitude, love, and respect to my parents for their continued support.

I would like to thank Ted Barber and the people at the White Sands Missile Range for their help in obtaining some of this data.

Finally, I wish to thank Eileen Fitzgerald for
typing this manuscript.

This research was funded under USAROD Grant
DAA-C29-76-C-0156.

Table of Contents

	Page
List of Symbols	v
List of Figures	xii
1.0 Introduction	1
2.0 Theoretical Method for Determining Velocity Parameters	6
2.1 Procedure	6
2.2 Signal to Noise and Filtering	16
2.3 Correction for Coherence Decay	25
2.4 Lidar Uncertainty Estimations	33
3.0 Instrumentation	36
3.1 The Wisconsin Lidar System	37
3.2 Remote Tower Instrumentation	41
3.3 Instrumentation at White Sands Missile Range	45
4.0 Experimental Results	49
4.1 Madison Experiments	50
4.2 White Sands Experiments	66
5.0 Conclusions	85
Appendices	
A Calculation of Spectra and Coherence	90
A.1 Calculation of Spectra and Cross Spectra by the Fast Fourier Transform Method	90
A.2 Calculation of the Coherence	94
B Calculation of the ratio of the Signal Spectrum to Noise Spectrum, Signal to Noise Ratio (SNR) and Optimal Linear Filter	96

	Page
Appendices (continued)	
C Derivation of an Analytical Form for Coherence Decay	101
D Error Analysis of Pilot Balloon and Tower Anemometer Wind Measurements	107
Bibliography	111

List of Symbols

A	Amplitude factor in non-linear regression
$A(k)$	Amplitude factor in filter estimation that is a function of wavenumber, k
A_r	Area of receiver telescope
$B(k)$	Wavenumber dependent parameter in filter calculation
c	Speed of light
C_1, C_2	Variances of time, space averaged auto-correlations in Gaussian derivation
C_{12}	Lag-cross covariance in Gaussian derivation
$Coh(k, \Delta x, \Delta t)$	Coherence of two spatial series with lateral separation, Δx , time separation Δt , at wavenumber, k
$\overline{Coh}(\Delta x, \Delta t)$	Weighted average coherence over wavenumber
D(x)	Spatial cosine taper data window
d	Normalization factor of variance due to data window
E_0	Transmitted laser pulse energy
edf	Number of equivalent degrees of freedom
$f(x)$	One dimensional spatial series
$\hat{f}(x)$	One dimensional spatial series convoluted with the data window
$f(\vec{q}, \vec{\bar{q}}, t)$	Three dimensional aerosol distribution in generalized coordinates, $\vec{q}, \vec{\bar{q}}, t$

$\mathcal{F}_f(k), \mathcal{F}_h(k)$	Fourier transform of $f(x), h(k)$
$G(\vec{q})$	Normalized three dimensional velocity distribution
$h(x)$	Optimal linear spatial filter
$H(k)$	Transfer function (Fourier transform) of the optimal linear filter, $h(x)$
J	Number of lidar returns averaged for smooth spectral estimates
K	Number of 5 minute average wind measurements in each Madison experiment
k	Wavenumber (m^{-1}) = $1/\text{wavelength}$
L	Length of data segment (m)
M	Number of discrete wavenumbers calculated from Fast Fourier Transform (FFT)
N	Number of data points in spatial series
N_T	Number of tower independent experimental measurements for Madison data
P	Probability of random coherence exceeding a certain limit
$P_r(R)$	Instantaneous received lidar return power at range R
$P(180)$	Backscatter phase function for single scattering
q_1, q_2, q_3	Generalized coordinates in coherence decay analysis

q_{1o}, q_{2o}, q_{3o}	Initial coordinate of centroid of Gaussian aerosol inhomogeneities
q_1, q_3	Position from origin of lidar returns in q_1, q_3 directions
$\dot{q}_1, \dot{q}_2, \dot{q}_3$	Generalized velocities in q_1, q_2, q_3 directions
$\Delta q_1, \Delta q_2,$	Spatial separation in q_1, q_2, q_3
Δq_3	
\bar{R}	Average pibal radial distance
R	Radial range along laser beam
R_h	Horizontal range; $R_h = R \cos \theta$
R_1	Digitized radial point ($R/15m$)
$\tilde{S}_1(\phi),$	Smoothed spectral estimate of series 1 (ϕ),
$\tilde{S}_2(\phi)$	series 2 (ϕ)
$\tilde{S}_{12}(\phi, \phi_1)$	Smoothed cross spectral estimate between series 1 (ϕ) and series 2 (ϕ_1)
\tilde{S}_n	Estimate of noise spectrum
\tilde{S}_s	Estimate of signal spectrum
SNR	Signal variance to noise variance ratio for spatially filtered series
T	Time period for spectral averaging
t	Time variable
t_n	Time of n^{th} laser pulse
Δt	Time lag separation
$\Delta t(k)$	Time lag as a function of wavenumber

Δt_m	Time lag for maximum weighted coherence
$\Delta t_m(k)$	Time lag for maximum coherence at wavenumber, k
$\bar{U}_1, \bar{U}_2, \bar{U}_3$	Average velocity in the q_1, q_2, q_3 directions
\bar{u}	Average cross component velocity
\bar{u}'	Apparent average cross component velocity
$U(k)$	Spectral cross component velocity
$V(k)$	Spectral velocity
$V_r(k)$	Radial spectral velocity component
\bar{V}	Wind speed magnitude
V_{lidar}	Lidar measured wind speed
V_{pibal}	Averaged pibal wind speed
V_{tower}	Tower measured wind speed
ΔV	Difference between lidar and tower (pibal) measured wind speeds
$\bar{\Delta V}$	Average speed difference
ΔV_{rms}	RMS speed difference from average
\bar{v}	Average radial velocity component
$W(k)$	Normalized weighting function for weighted average coherence
x	Eastward horizontal component of pilot balloons position
Δx	Cross beam spatial separation

$Y_\phi(t_n, R_1)$	Lidar return power at azimuth ϕ , time t_n , and range point R_1
$Y'_\phi(t_n, R_1)$	Deviations from a time centered, running mean profile in Y_ϕ at azimuth ϕ
$Y''_\phi(t_n, R_1)$	Deviations of Y'_ϕ from the average spatial value of Y'_ϕ
Y	Northward horizontal component of pilot balloon positions
Z	Height of laser beam at range R
α	Azimuth angular beam separation
β_e	Extinction cross section per unit volume
β_s	Scattering cross section per unit volume
β_{s180}	Volume backscatter coefficient
Γ'	Random series coherence limit for a probability P
δR	Range resolution of pibal tracking radar
δt	Average time interval used in pibal measurements
δU_{ew}	Maximum East-West pibal speed uncertainty
δV_{ns}	Maximum North-South pibal speed uncertainty
δV_c	Computationally estimated lidar speed uncertainty
δV_p	Maximum uncertainty in pibal wind speed
δV_g	Maximum lidar speed quantization uncertainty
δV_{rms}	Rms speed uncertainty of lidar and tower (pibal) measurements

x

$\delta\theta$	Elevation uncertainty in pibal tracking radar
$\delta\phi$	Azimuthal uncertainty in pibal tracking radar
$\delta\phi_p$	Maximum pibal azimuth uncertainty
$\delta\phi_l$	Maximum lidar azimuth quantization uncertainty
$\delta\phi_{avg}$	RMS azimuth uncertainty of lidar and tower (pibal) measurements
ϵ_v	Ratio of speed errors to RMS speed uncertainty
ϵ_ϕ	Ratio of azimuth errors to RMS azimuth uncertainty
$\overline{\epsilon^2}$	Mean square error between filtered series and signal
Θ	Elevation angle of lidar
K	Lidar system constant
V	Laser pulse frequency
ρ	Lag-cross correlation coefficient
$\hat{\rho}$	Ensemble average lag-cross correlation coefficient
σ_a	RMS width of aerosol distribution for isotropy
$\sigma_1, \sigma_2, \sigma_3$	RMS widths of aerosol distribution in q_1, q_2, q_3 directions
$\bar{\sigma}_{s,\phi}$	Statistical uncertainty in average tower measurements

$\tilde{\sigma}_v$	Standard deviation of tower \tilde{v} , value from
$\tilde{\sigma}_{vt}$	Velocity fluctuation for entire experimental time period
$\tilde{\sigma}_s$	RMS width of wind speed distribution assuming isotropy
$\tilde{\sigma}_{s_{lidar}}$	RMS speeds derived from lidar and tower measurements
$\tilde{\sigma}_{s_{tower}}$	
ϕ	Azimuth direction of wind from lidar
ϕ, ϕ, ϕ	Azimuth of lidar returns in three angle scan
$\bar{\phi}_l$	Average azimuth of lidar scan
ϕ_{pibal}	Azimuth of pilot balloon measurements
ϕ_{tower}	Average azimuth of tower measurements
$\Delta\phi$	Difference between lidar and tower (pibal) azimuth measurements
$\bar{\Delta\phi}$	Average azimuth difference
$\Delta\phi_{rms}$	RMS azimuth difference
$\Delta\psi(k)$	Relative phase in smoothed cross spectra
$\tilde{\tau}_e$	Eulerian time scale

List of Figures

Figure		Page
1	Schematic diagram of lidar winds from natural aerosols	3
2	Vertical and horizontal views of elevated three angle lidar scan	11
3	Graph of aerosol inhomogeneities spectrum for three cases of signal to noise ratio	20
4	Graph of estimated signal spectrum to noise spectrum for data of Fig. 2	21
5	Graph of square of optimal transfer function for data of Fig. 2	22
6	Filtered and unfiltered deviations from a running mean profile for data of Fig. 2	23
7	Weighted average coherence as a function of time lag (Δt) for three spatial separations (Δx). Least squares fit to equation 2.3.3 is also shown	29
8	Lidar quantization uncertainties as a function of speed and angle	35
9	Block diagram of University of Wisconsin lidar system	39
10	Map of Madison area	42
11	Map of White Sands Missile Range experimental site	46
12- 17	Time histories of lidar and tower anemometer parameters at Madison	55-60
18- 20	Comparisons of lidar and tower anemometer velocity parameters	62-64
21- 26	Height profiles of lidar and pilot balloon velocity parameters at White Sands Missile Range	68-73
27- 32	Time histories of lidar and pilot balloon speeds and azimuths at each height level	76-81

List of Figures (continued)

Figure		Page
33-	Comparisons of lidar and pilot	83-84
34	balloon speeds and azimuths	
35	Graphs of $\epsilon_r, \epsilon_\phi$ vs. SNR	88
C-1	Geometry for experimental correlations	103
D-1	Geometry of pilot balloon position in spherical coordinates	108

1.0 Introduction

Optical remote sensing of the boundary layer flow can potentially provide the spatial and temporal detail needed in meteorological application in this region. Convective boundary layer studies, air pollution monitoring, and aviation operations require knowledge of the wind velocity variability and atmospheric dispersal mechanisms to gain a better understanding of the physical principles acting in the boundary layer. The application of laser technology to measure the wind velocity can provide wind information with greater sampling statistics and negligible influence on the flow pattern over conventional wind measurements.

A number of different techniques have been investigated for remote determination of wind velocities using optical methods. Heterodyne determination of the Doppler shift in the received scattered light from transmitted laser pulses have been used by Lawrence et al. (1972) and Benedetti-Michelangeli et al. (1972) to calculate the wind velocity component along the laser path. Kjelass and Ochs (1974) determined the mean horizontal velocity and divergence near the surface over a 300 m equilateral triangle by correlation of scintillation patterns. Zuev et al. (1977) have used the correlation of two spatially separated laser beam signals to determine scale sizes and life-times of aerosol

inhomogeneities. Correlation of lidar return signals scattered from aerosol density inhomogeneities have been used to estimate mean horizontal wind velocities. Armstrong et al. (1976) have obtained average wind measurements over a time scale of seconds from a distance of 250 m. Eloranta et al. (1975) have used this procedure to estimate the average wind velocity at distances of several kilometers. Lidar returns for large scale (60 m - 1.0 km) spatial inhomogeneities in naturally occurring aerosol content are used in this study to determine two horizontal wind velocity components and also an estimate of the rms wind speed.

Fig. 1 represents a schematic diagram of the procedure used in obtaining lidar measurements of the spatial aerosol inhomogeneities at different times and azimuth directions. These spatial aerosol inhomogeneities are primarily due to nonuniform aerosol sources and turbulent mixing of particulate matter into the atmosphere. Motion of the wind can be inferred by detecting the movements of these aerosol inhomogeneities as they are advected through one lidar sample volume to the next. Previous studies by Eloranta et al. (1975) and Leuthner (1976) have shown that velocity information can be obtained by correlation between two lidar radial aerosol inhomogeneity profiles separated in time and space. They calculated a two-dimensional

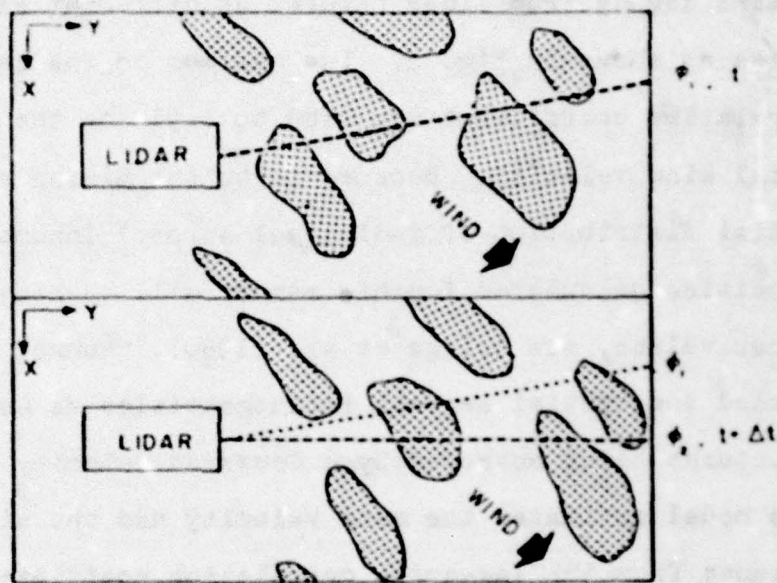


Figure 1: Schematic diagram of lidar wind measurements using natural aerosol as tracers. Diagrams are at time t and $t + \Delta t$, lidar beam has moved in azimuth direction in this time. Aerosol motion is estimated by correlating the lidar inhomogeneity profiles between two different beams, ϕ_i , t and ϕ_j , $t + \Delta t$.

lag-cross correlation coefficient in time lag Δt and radial spatial lag Δy from lidar returns at different azimuth angles as shown in Fig. 1. The maximum in the lag-cross correlation coefficient was used to estimate the mean horizontal wind velocity. Because turbulent mixing changes the spatial distribution of individual aerosol inhomogeneities, velocities calculated in this manner will be biased toward higher values, see Briggs et al. (1950). Kunkel (1978) modeled the spatial aerosol inhomogeneities as Gaussian structures being advected by a Gaussian velocity distribution. This model estimates the mean velocity and the wind speed variance from the lag-cross correlation coefficient values for different lateral separations using the method developed by Leuthner (1976).

The coherence which describes the correlation at various radial wavenumbers k is used in this study for velocity calculations. Spectral radial velocity components are calculated from the spatial phase difference at each spectral wavenumber between inhomogeneity profiles due to their radial drift. The lateral spectral velocity components are calculated from the time lag for each wavenumber component to drift from one azimuth direction to the next, cf. Fig. 1. The mean value of each velocity component is obtained by averaging over wavenumbers. A model similar to that of Kunkel (1978) is used to correct for the effects of

turbulence and estimate the rms wind speed.

An increase in computational efficiency is obtained in transforming to radial wavenumbers k by using Fast Fourier Transform (FFT) in calculation of spectra and coherence of spatial aerosol inhomogeneity profiles. The FFT computes discrete wavenumbers which depend on the data segment length and point separation. (For this study $k_i = i/960$ m, $i = 1, 32$.) This method can be 5 to 50 times more efficient computationally over the Blackman-Tukey method, see Cooley et al. (1970). Filtering the spatial series to reduce the effects of noise is also more efficient in wavenumber space. A method has been developed to optimize the filtering of the spatial series to maximize the signal to noise ratio in changing atmospheric conditions.

This study has been organized in the following manner. The theoretical procedure used to determine the wind velocity parameters is presented in Chapter 2. Derivations and computational details are left to the appendices for those with further interest. Chapter 3 describes the instrumentation used during this study. The results of experiments conducted at Madison, Wisconsin and the White Sands Missile Range, New Mexico are shown in Chapter 4. The conclusions are stated in Chapter 5.

2.0 Theoretical Method for Wind Velocity Measurement

This chapter presents the theoretical method used in this thesis for remote horizontal wind velocity measurements using a monostatic lidar. It is divided into four sections: the procedure for obtaining measurements and processes required to calculate coherence values and spectral velocities, estimation of the spectral signal to noise ratio and optimal filtering, wind velocity parameters calculated from the correction for turbulence, and uncertainties in lidar wind measurements. Mathematical details and derivations are contained in the appendices.

2.1 Procedure: Obtaining Lidar Wind Measurements

The procedure to obtain measurements used to infer horizontal wind velocity from the motion of spatial aerosol inhomogeneities is described in this section. A method is presented to calculate these spatial inhomogeneities in the mean aerosol content from lidar measurements. The experimental arrangement for obtaining these measurements is also shown. Horizontal wind velocity information is calculated from the coherence between lidar measured radial profiles of spatial aerosol inhomogeneities.

Lidar is an active remote sensing device used to probe the atmosphere. A laser pulse is transmitted into the atmosphere and measurements are made of the photons scattered

through 180 degrees by atmospheric constituents into a receiver whose axis is aligned parallel to the laser axis. These detected scattered photons are converted into an electrical signal which is proportional to the amount of scattered laser light. The equation for singly scattered monostatic lidar return power is¹

$$P_r(R) = E_0 \frac{c}{R^4} A_r \beta_s(R) \frac{P(180^\circ)}{\gamma \pi} e^{-\int_{R'}^R \beta_e(\epsilon') d\epsilon'} \quad 2.1.1$$

where R is the radial distance along the propagation path

R' is the integration variable along R

P_r(R) is the instantaneous received power from range R

E₀ is the transmitted laser pulse energy

A_r is the area of the receiver telescope

c is the speed of light

$\beta_s(R)$ is the scattering cross-section per unit volume

$\beta_e(R)$ is the extinction cross-section per unit volume

$P(180^\circ)$ is the backscatter phase function

¹ A modified form of the lidar equation presented by Collis (1969).

A description of the University of Wisconsin lidar system is presented in section 3.1. Lidar returns are pre-processed by this system in the following manner. Logarithmic amplification compresses the dynamic range of the signal. The signal is digitized into 10 bit words at a 10MHz rate which yields a 15 m resolution along the laser beam path. Lidar returns are corrected for the "range square attenuation" and normalized by the transmitted laser pulse energy using a PDP 11/40 minicomputer. Lidar returns analyzed in this study are given by $y_\phi(t_n, R_1)$, the natural logarithm of the quantity $(P_r(R) R^2/E_0)$;

$$y_\phi(t_n, R_1) = \ln(K \beta_{s, r_0}(R_1)) - 2 \int_0^{R_1} \beta_s(R') dR' \quad 2.1.2$$

where t_n is the time at which the nth laser shot occurred

R_1 is the range to the 1th data point

$y_\phi(t_n, R_1)$ is the lidar return analyzed at azimuth angle ϕ

K is a systems parameter constant

$\beta_{s, r_0}(R_1)$ is the volume backscatter coefficient

$$\frac{P(180^\circ)}{4\pi} \beta_s(R_1)$$

Spatial inhomogeneities of the atmospheric aerosol content can be obtained from lidar measurements. Spatial fluctuations in concentration, size and shape of aerosol particles produce spatial variations in the backscatter coefficient β_{5180} . The attenuation term in Eq. 2.1.2 ($-2 \int \beta_a(r) dr$) is a monotonically increasing function with range and is assumed to be only slowly varying in time. Estimation of the spatial inhomogeneities in the mean aerosol distribution can be obtained by calculating radial deviations from a time centered running mean radial profile of Eq. 2.1.2. for each azimuth angle. Spatial deviations from the mean aerosol profile calculated in this manner remove the effects of slow temporal variations in the extinction (cf. Eq. 2.1.2.) in correlation between profiles. These deviations from the mean aerosol profile are given by

$$Y'_\phi(t_n, R_t) = Y_\phi(t_n, R_t) - \frac{1}{N_T} \sum_{i=1}^{N_T} Y_\phi(t_i, R_i) \quad 2.1.3$$

where N_T is the number of lidar profiles used to calculate the average lidar profile

$Y_\phi(t_n, R_t)$ is the deviation in Y_ϕ from the average profile

The average value of $Y_\phi'(t_n, R_1)$ along the range R_1 is removed before harmonic analysis to reduce the leakage of zero wavenumber component into other wavenumber bands. Radial profiles of the spatial aerosol inhomogeneities analyzed in this thesis are defined as

$$Y_\phi''(t_n, R_i) = Y_\phi'(t_n, R_i) - \frac{1}{N} \sum_{j=1}^{N-1} Y_\phi'(t_n, R_j) \quad 2.1.4$$

where N is the number of data points along the radial range i , i is the first data point of this segment.

This procedure also suppresses spurious harmonics generated by discontinuities in the aerosol structure.

Lidar measurements of the spatial distribution in aerosol content are obtained from a sequential three angle azimuth PPI scan at a fixed elevation angle, see Fig. 2. The sequential scanning procedure obtains lidar profiles of the aerosol content at azimuth angles $\phi, \phi_1, \phi_2, \phi_3, \phi_4, \phi_5$, etc.. Short data segments along two beam paths can be treated as if they are parallel for small angular separation, $\Delta\phi = \phi_2 - \phi_1$, and the change in the lateral separation at the endpoints is small compared to the average lateral separation. The lateral separation distance Δx is defined as

$$\Delta x = 2 R \sin (\Delta\phi/2)$$

2.1.5

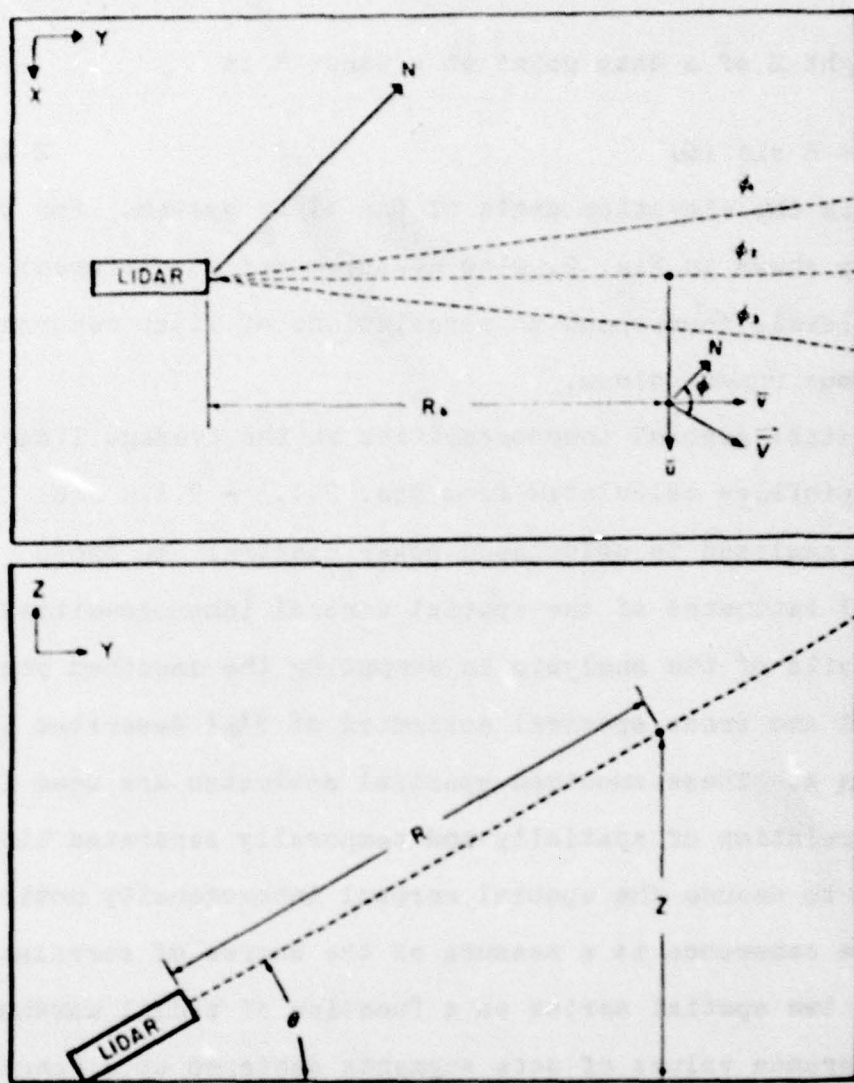


Figure 2: Vertical and horizontal views of lidar wind measurement scheme. Lidar measurements are obtained at three azimuth angles (ϕ_1, ϕ_2, ϕ_3) with an elevation angle, Θ . The wind velocity has components perpendicular and parallel to the center azimuth (ϕ_2) of \bar{u} and \bar{v} . The horizontal range is given as $R_h = R\cos(\Theta)$.

The height Z of a data point at a range R is

$$Z = R \sin (\theta)$$

2.1.6

where θ is the elevation angle of the lidar system. For the geometry shown in Fig. 2, wind measurements at different height levels correspond to correlations of lidar returns at various range values.

Spatial aerosol inhomogeneities in the average lidar radial profiles calculated from Eqs. 2.1.3 - 2.1.4 are Fourier analyzed to calculate power spectral and cross spectral estimates of the spatial aerosol inhomogeneities. The details of the analysis in computing the smoothed power spectral and cross spectral estimates of Y'_{ρ_1} described in Appendix A. These smoothed spectral estimates are used in the correlation of spatially and temporally separated lidar returns to deduce the spatial aerosol inhomogeneity motion.

The coherence is a measure of the degree of correlation between two spatial series as a function of radial wavenumber k . Coherence values of data segments centered at a range R are calculated for various time lags, Δt and for three lateral separations, $\Delta x = 0m$, $\Delta x = 2 R \sin((\phi_2 - \phi_1)/2)$ and $\Delta x = 2 R \sin((\phi_3 - \phi_1)/2)$. The coherence between a number of radial profiles of the aerosol inhomogeneities is, cf.

Eq. A.2.1

$$Coh(k, \Delta x, \Delta t) = \frac{\tilde{S}_{\phi_1 \phi_m}^*(k, \Delta x, \Delta t) \cdot \tilde{S}_{\phi_1 \phi_m}(k, \Delta x, \Delta t)}{\tilde{S}_{\phi_1}(k) \cdot \tilde{S}_{\phi_m}(k)} \quad 2.1.7$$

where * denotes complex conjugation

k is the radial wavenumber (m^{-1})

Δt is the time lag between radial profiles at ϕ_1, ϕ_m

Δx is the average lateral separation between radial profiles at ϕ_1, ϕ_m

$\tilde{S}_{\phi_1}(k)$ is the smoothed spectral estimate of the radial profiles of the spatial aerosol inhomogeneities, Y'_{ϕ_1}

$\tilde{S}_{\phi_m}(k)$ is the smoothed spectral estimate of the radial profiles of the spatial aerosol inhomogeneities Y'_{ϕ_m}

$\tilde{S}_{\phi_1 \phi_m}^{(k, \Delta x, \Delta t)}$ is the smoothed cross spectral estimate between radial profiles of the spatial aerosol inhomogeneities measured by Y'_{ϕ_1} and Y'_{ϕ_m} . Y'_{ϕ_1} and Y'_{ϕ_m} are separated by an average lateral distance Δx and time lag Δt

The process of smoothing the spectral estimates is important in calculating reliable measurements of the coherence. Smoothing the spectral estimates decreases the

probability that random data will yield a given coherence value. The probability of random data having a given coherence value is (cf. Eq. A.2.2)

$$P = (1-\rho^2)^{\text{edf}-2} \quad 2.1.8$$

where P is the probability

ρ is the coherence value

edf is the equivalent number of degrees of freedom
The probability of random data having a coherence value of 1.0 is 100% in the limiting value for an equivalent number of degrees of freedom equal to 2. For data presented in this study coherence values greater than .17 have a 5% probability of being random.

Estimation of the horizontal wind velocity can be obtained by reliable measurements of the coherence between lidar radial profiles of the aerosol inhomogeneities. Individual spectral components are assumed to be propagating with a spectral velocity $\vec{v}(k)$. The relative phase difference $\Delta\psi$ in the smoothed aerosol inhomogeneity cross spectrum is proportional to the distance over which the spectral component has drifted radially.

$$\frac{\Delta\psi}{2\pi} = v_r(k) \cdot \Delta r \cdot k \quad 2.1.9$$

where $v_r(k)$ is the spectral velocity component along the beam path, cf. Fig. 2. The solution for the radial spectral

velocity is

$$v_r(k) = \frac{\Delta \varphi(\Delta)}{2\pi \Delta \cdot \Delta t} \quad 2.1.10$$

The lateral spectral velocity component $u(k)$ can be estimated from the coherence calculations between lidar aerosol inhomogeneity profiles at different azimuth angles, cf. Fig. 2. A maximum coherence value in time lag Δt determines approximately the time for a spectral component to drift the average lateral separation distance Δx . An approximate lateral spectral velocity component $u'(k)$ is given by

$$u'(k) = \Delta x / \Delta t_m(k) \quad 2.1.11$$

where $\Delta t_m(k)$ is the time lag value for maximum spectral coherence. Random changes in the spatial aerosol inhomogeneity profiles due to turbulent mixing cause the degree of correlation (coherence) to decrease with increasing Δx and Δt , cf. Briggs et al. (1950). Section 2.3 presents an approximation to estimate the mean lateral velocity from the coherence decay.

2.2 Signal Spectrum to Noise Spectrum Estimation and Filtering

This section describes the estimation of an optimal linear filter based upon the spectral characteristics of the lidar radial aerosols profiles. A method to calculate this optimal filter from lidar coherence measurements with no lateral separation is also developed. The derivation of this procedure is detailed in Appendix B. This procedure allows the spectral characteristics of the data being processed to dictate the filtering characteristics. Examples of the effectiveness of this procedure are included at the end of this section.

A number of sources contribute to noise in lidar measurements. Background light and statistical fluctuations in detecting scattered photon are sources of noise in lidar measurements. Electronics and digitization noise also contribute to the total noise in lidar returns. Rapidly evolving small aerosol density structures are also part of the background noise. Spatial filtering of lidar radial profiles is necessary to reduce these noise contributions from the signal of the spatial aerosol inhomogeneities.

A filter that reproduces the signal from the aerosol inhomogeneities with a minimum in error can be calculated from knowledge of the spectral characteristics of both the signal $\tilde{S}_s(k)$ and noise $\tilde{S}_n(k)$ contributions, cf. Wainstein

and Zubakov (1962). The Fourier transform $H(k)$ of the optimal linear filter $h(x)$ is given by, cf. Eq. B.7.

$$H(k) = \frac{\tilde{S}_s(k)}{\tilde{S}_s(k) + \tilde{S}_N(k)} \quad 2.2.1$$

This optimal transfer function $H(k)$ is derived for measurements where the signal and noise contributions are not correlated. The noise contributions to lidar returns are assumed to correlate only with the same return and any correlation between different lidar profiles is primarily due to signal contributions. Power spectral and cross spectral estimates of the aerosol inhomogeneity signals are sufficiently smoothed to decrease the probability of random statistical correlations (see discussion in section 2.1 p.13).

An estimate of the ratio of the signal spectrum to the noise spectrum can be obtained from coherence measurements between spatial series in the limit as the time separation approaches zero. The derivation of this procedure for estimating the signal spectrum to noise spectrum ratio from coherence measurements is detailed in Appendix B. Coherence values are calculated from experimental lidar measurements of aerosol inhomogeneities for the lateral separation $\Delta x = 0$, see Fig. 2. These coherence values are functions of wavenumber and time lag only. They are observed from Fig. 7 to be approximately Gaussian in time lag Δt . Extrapolation

of coherence measurements at each wavenumber k to $\Delta t = 0$ is estimated by a least squares regression to a Gaussian of the form

$$\text{Coh}(k, 0, \Delta t) = A(k) \cdot \exp(-B(k) \cdot \Delta t^2) \quad 2.2.2$$

where $A(k)$ and $B(k)$ are the regression parameters at each wavenumber. The extrapolated coherence value for $\Delta t = 0$ is just the amplitude factor $A(k)$ (note that $A(k) = 1$ for noise free measurements). The ratio of the signal spectrum to the noise spectrum can be estimated by

$$\frac{S_s(k)}{S_N(k)} = (A^{\frac{1}{2}}(k) - 1)^{-1} \quad 2.2.3$$

where this equation is derived in appendix B as Eq. B.6. The transfer function of the optimal linear filter can be calculated from knowledge of the signal spectrum to noise spectrum ratio, cf. Eqs. B.5 and B.7.

$$H(k) = (\text{Coh}(k, 0, 0))^{\frac{1}{2}} = A^{\frac{1}{2}}(k) \quad 2.2.4$$

The filter corresponding to this transfer function will optimize the recovery of signal information of spatial aerosol inhomogeneities from lidar aerosol profiles.

An estimate of the ratio of the total filtered signal variance to noise variance (SNR) is calculated here by replacing the integrals in Eq. B.10 by sums over all

wavenumbers

$$\text{SNR} = \frac{\sum_{\text{w}} H^2(\text{w}) \cdot (\tilde{S}_s(\text{w})/\tilde{S}_n(\text{w}))}{\sum_{\text{w}} H^2(\text{w})} \quad 2.2.5$$

where the sums are over the M discrete wavenumbers obtained from the Fast Fourier Transform (FFT).

Figs. 3-6 show experimental results from lidar data obtained on January 19, 1978 at White Sands Missile Range, New Mexico. Three cases are shown for different values of SNR to illustrate the effects of noise upon the data. The cases of high (SNR=2.90), intermediate (SNR=1.19) and low (SNR=0.65) signal to noise ratio nearly encompass the total range observed in the data presented in this thesis.

The power spectra of the spatial aerosol inhomogeneities calculated from Eq. 2.1.4 are shown in Fig. 3. These spectra are not expected to follow the -5/3 power law since the logarithm of the lidar returns are used in analysis for increased computational efficiency and to remove the effect of slowly varying extinction.

Figs. 4 and 5 are similar graphs for the estimated signal spectrum to noise spectrum ratio (Eq. 2.2.3) and the optimal transfer function (Eq. 2.2.4) for the data presented in Fig. 3. Fig. 4 shows that larger values of signal to noise ratio spectrum occur for lower wavenumbers. These wavenumbers are the spectral components that contain

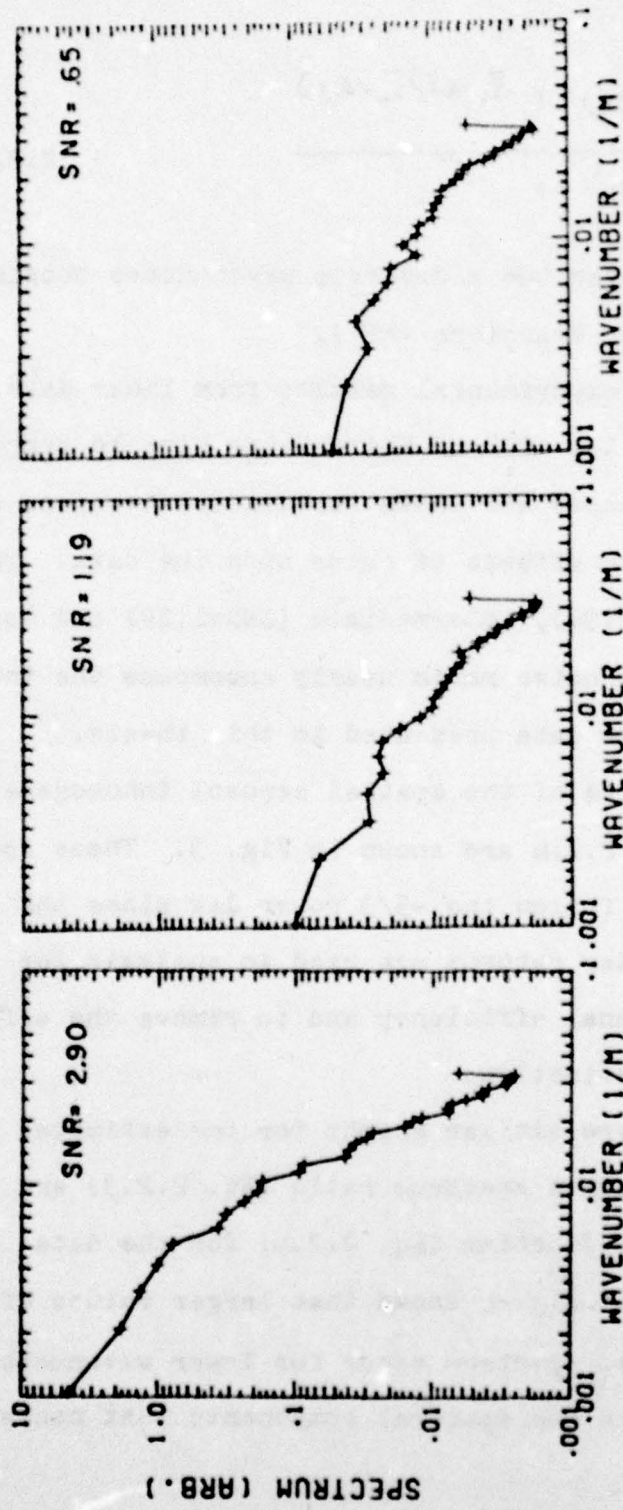


Figure 3: Graph of the spatial aerosol fluctuation spectrum (arbitrary units) as a function of wavenumber (m^{-1}) for cases of a) high (2.90), b) intermediate (1.19) and c) low (.65) signal/noise variance ratio (SNR). Data was obtained on January 19, 1978 at White Sands Missile Range during a light snow storm.

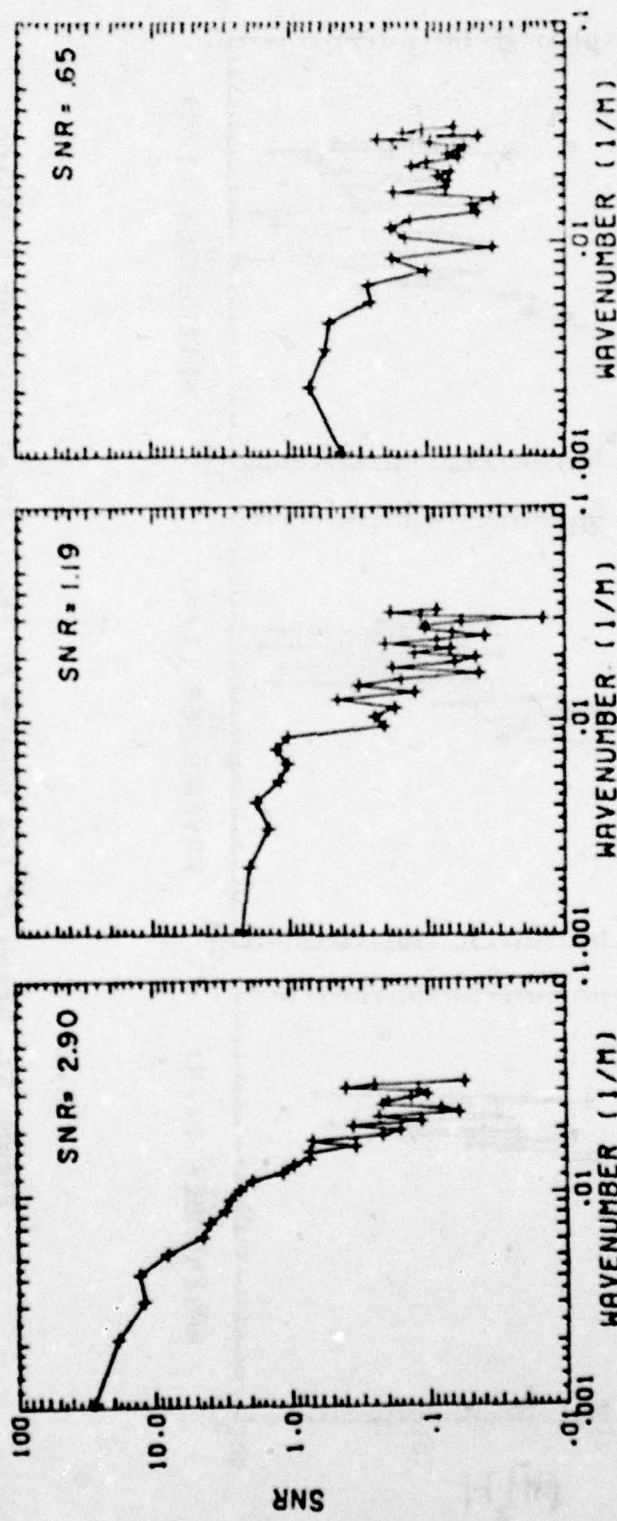


Figure 4: Graph of the estimated signal spectrum to noise spectrum ratio for the same data used in Figure 3 for cases of high (a), intermediate (b), and low (c) values of SNR. Note high variance in the estimation of the spectral signal/noise for values less than approximately 0.5.

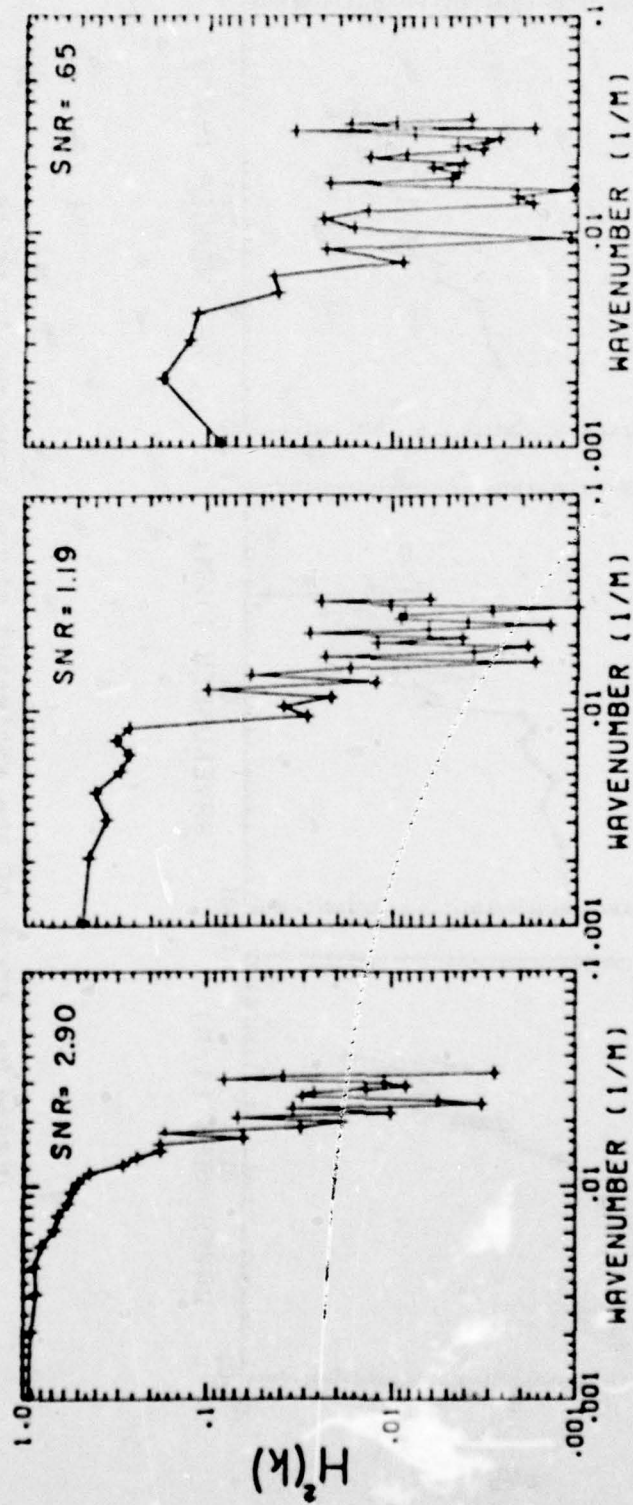


Figure 5: Graph of the square of the optimal transfer function calculated from the spectral signal/noise of Figure 4. Note decrease in magnitude and bandwidth for decreasing SNR.

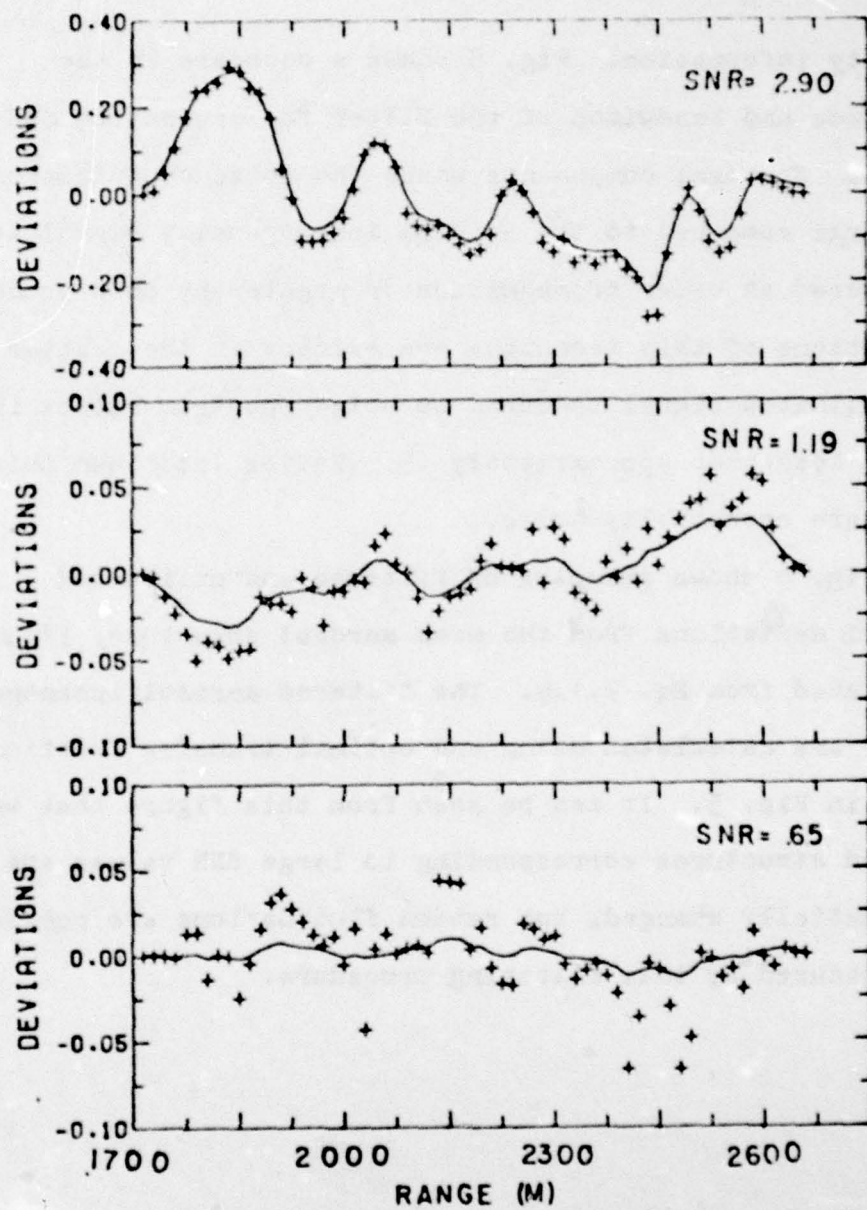


Figure 6: Graphs of filtered (lines) and unfiltered (+) deviations (Y'_d (t_n, R_1) from equation 2.1.4) in the mean aerosol content for data of Fig. 3. Note the scale change for large SNR values (2.90).

velocity information. Fig. 5 shows a decrease in the magnitude and bandwidth of the filter for decreasing SNR values. Spectral components where the noise contributions are large compared to the aerosol inhomogeneity signal are suppressed an order of magnitude or greater by this process. Limitations of this technique are evident in the scatter of the estimated signal spectrum to noise spectrum ratios for values less than approximately .5. Ratios less than this value are essentially noise.

Fig. 6 shows examples of filtered and unfiltered spatial deviations from the mean aerosol structure, \bar{Y}'' , calculated from Eq. 2.1.4. The filtered aerosol inhomogeneities are calculated using the optimal transfer functions shown in Fig. 5. It can be seen from this figure that well defined structures corresponding to large SNR values are not substantially changed, but random fluctuations are considerably reduced by this filtering procedure.

2.3 Velocity Correction for Coherence Decay

A method is developed in this section to estimate the mean value of the horizontal wind velocity and the rms wind speed modeling the spatial aerosol inhomogeneities observed by lidar measurements by a Gaussian approximation. A derivation of the functional form of the model is given in Appendix C. The final form of this model includes optimal filtering characteristics derived in the previous section to maximize the information in the profiles of aerosol inhomogeneities.

The spectral velocity component perpendicular to the beam pattern $u(k)$ (see Fig. 2) is calculated from the coherence of lidar measurements at various times and spatial separations. Random changes in the aerosol inhomogeneity pattern caused by turbulent velocity variations, decreases the maximum value of the coherence with increasing time lag and lateral separation. Briggs et al. (1950), Briggs (1968a, b) and Gossard (1969) have devised first order approximations to obtain the mean ionospheric drift velocity from reflected radio waves in the presence of random fluctuations. They observed that the correlations and cross spectra were nearly Gaussian in time and spatial separation.

A model derived in similar manner to that of Kunkel (1978) is used to estimate the mean lateral wind speed of all spectral components and the rms wind speed. Appendix C

presents a derivation of the functional form of the coherence decay with increasing temporal and spatial separations for an ensemble of Gaussian aerosol inhomogeneities being advected by a Gaussian velocity distribution. The functional form of the coherence under these assumptions is (Eq. C.11)

$$\text{Coh}(\Delta x, \Delta t) = \left[\frac{\sigma_{\bar{u}}^2}{2\bar{C}_s^2 + \bar{C}_s^2 \Delta t^2} \right]^2 \cdot \exp \left[- \frac{(\Delta x - \bar{u} \Delta t)^2}{2\bar{C}_s^2 + \bar{C}_s^2 \Delta t^2} \right] \cdot \exp(-4\pi^2 k^2 \bar{C}_s^2 \Delta t^2)$$

2.3.1

where k represents wavenumber (m^{-1})

\bar{u} is the mean lateral wind velocity component (m/s)

Δx is the average lateral spatial separation between lidar measurements (m)

\bar{C}_s is the rms width of the horizontal extent of the spatial aerosol inhomogeneities (m)

\bar{C}_s is the standard deviation of the velocity distribution (m/s)

To emphasize the spectral components where the signal spectrum is detectable over the background noise and to increase the statistical significance, a weighted average coherence over wavenumber ($\text{Coh}(\Delta x, \Delta t)$) is computed. The weighting function used to optimize the information in the signal spectrum over the noise spectrum is the square of

the optimal transfer function from Eq. 2.2.4. since factors of the optimal transfer function occur in spectral estimates. This weighting function is normalized such that the sum of all the weights is unity.

$$W(k) = H^2(k) / \sum_{k=1}^{k_m} H^2(k) \quad 2.3.2$$

The final functional form of the model is the weighted average of Eq. 2.3.1 over all wavenumbers

$$\bar{Coh}(4x, \Delta t) = A \left[\frac{\omega \sigma_a^2}{\omega \sigma_x^2 + \sigma_s^2 \Delta t^2} \right]^2 \exp \left[-(\omega \cdot \Delta t)^2 / (2\sigma_x^2 + \sigma_s^2 \Delta t^2) \right] \\ \cdot \sum_{k=1}^{k_m} W(k) \exp(-4\pi^2 k^2 \sigma_s^2 \Delta t^2) \quad 2.3.3$$

where $W(k)$ is the weighting function given in Eq. 2.3.2 and the amplitude factor A is included to account for finite ratios of signal to noise.

Experimentally measured weighted coherence calculations from lidar aerosol inhomogeneity profiles are fitted to the functional form of Eq. 2.3.3 using the nonlinear regression routines provided by the Madison Academic Computing Center (Marquardt 1963). The four parameters regressed against are

A the amplitude factor to account for finite signal to noise ratios

\bar{u} the mean lateral wind speed

σ_a the rms horizontal width of the aerosol inhomogeneities

σ_s the standard deviation of the wind speed distribution

Experimental data points for nonlinear regression are chosen about the maximum weighted coherence value for each of the three lateral separations described in Section 2.1. An example of these weighted coherence measurements for different time and spatial separation along with a least squares fit to Eq. 2.3.3 is shown in Fig. 7.

An initial estimate of these regression parameters is needed to speed convergence of the nonlinear regression to the optimal values. The initial estimate of the amplitude factor is the weighted coherence extrapolated to zero time lag for $\Delta x=0$.

$$A = \overline{\text{Coh}}(0, 0) = \sum_{k=1}^K W(k) \cdot A(k) \quad 2.3.4$$

The weighted coherence are assumed to have a maximum value in A_t near the time interval needed for the aerosol inhomogeneities to drift the lateral separation distance Δx . (Eq. 2.1.5). This assumption is valid only for lateral velocities much greater than the magnitude of the wind speed fluctuations. Data presented in this thesis meet

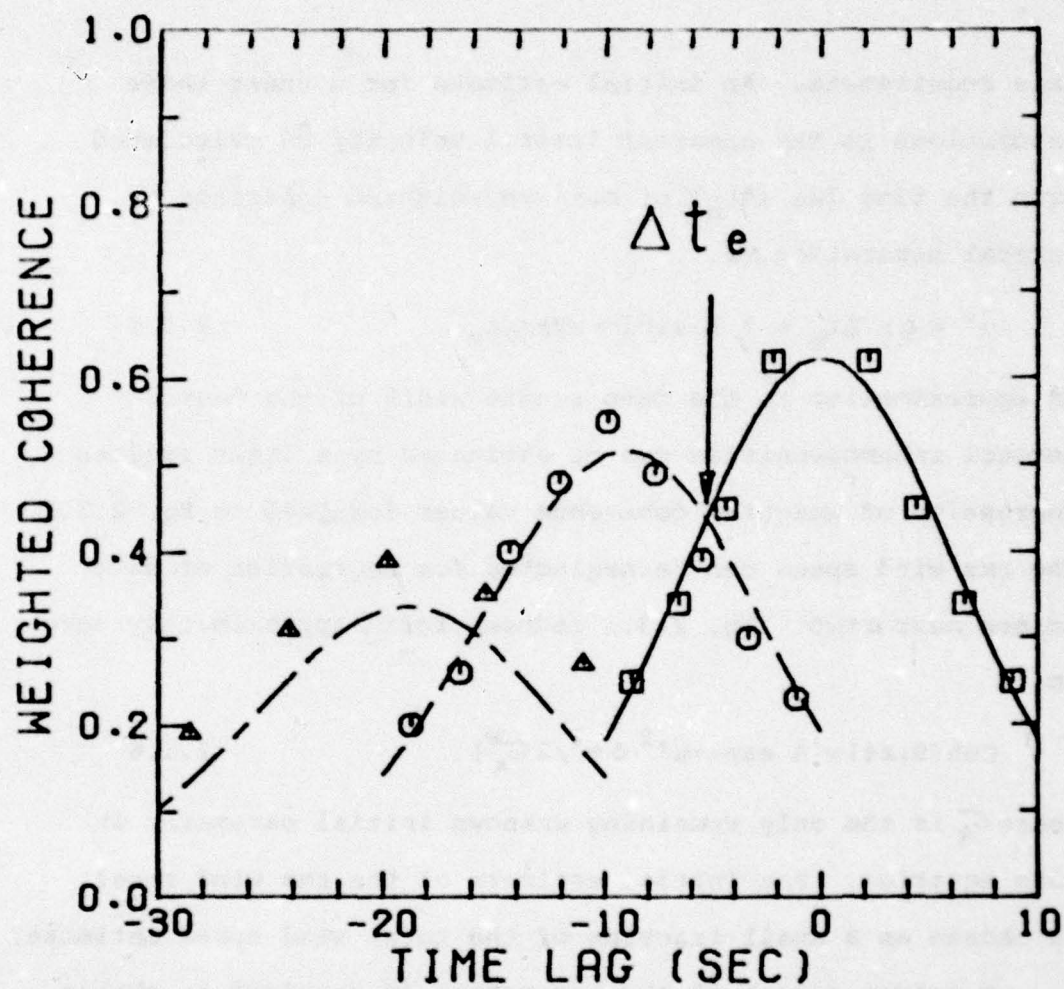


Figure 7: Weighted coherence as a function of time lag for three lateral separations ($\Delta x = 0\text{m}$ (\square)), $\Delta x = 38\text{m}$ (\circ), $\Delta x = 76\text{m}$ (\triangle)) from data obtained on January 19, 1978. Lines are a least squares fit to Eq. 2.3.3. Relatively poor fit for $\Delta x = 76\text{m}$ is a result of weighting the outside coherence value by $\frac{1}{3}$. These values are weighted because fewer spectra are used to estimate the coherence.

this requirement. An initial estimate for \bar{u} under these assumptions is the apparent lateral velocity \bar{u}' calculated from the time lag (Δt_m) of maximum weighted coherence at lateral separation Δx .

$$\bar{u}' = \Delta x / \Delta t_m = 2 \bar{R} \sin(\alpha/2) / \Delta t_m \quad 2.3.5$$

An approximation to the mean square width of the Gaussian aerosol inhomogeneities can be estimated by a least squares regression of weighted coherence values for $\Delta x=0$ to Eq. 2.3.3. The rms wind speed can be neglected for regression of data points near $\Delta t=0$. Eq. 2.3.3 reduces for C_g approximately zero to

$$\text{Coh}(0, \Delta t) = A \exp(-u'^2 \Delta t^2 / 2 C_g^2) \quad 2.3.6$$

where C_g is the only remaining unknown initial parameter in this equation. The initial estimate of the rms wind speed is chosen as a small fraction of the total wind speed estimate.

A coarse search of the parameters is required to obtain a close estimate for a true minimum and not a local minima. The weighted coherence measurements curves are regressed to Eq. 2.3.3 for each parameter while holding the other parameters constant. This procedure is iterated until the change in each parameter is less than some intermediate error tolerance. A final simultaneous regression on all parameters is

performed to establish their optimal values. The model parameters to be compared with conventional wind velocity measurements are the mean lateral velocity component \bar{u} and the rms wind speed σ_s .

The curve fitting procedure described above is used to estimate a correction from the apparent velocity caused by turbulent changes in the aerosol patterns. The magnitude of this correction depends upon the magnitude of the maximum time lag and the lateral separation distance. This correction can be as much as 10-20% of the mean lateral wind speed and can change the mean wind direction estimation 3 to 8 degrees.

The average radial velocity (\bar{v}_r) of all spectral components is

$$\bar{v}_r = \frac{1}{M} \sum_{k=1}^{M-1} v_r(k) \quad 2.3.7$$

Radial velocity components calculated from Eq. 2.1.9 are averaged until a relative phase shift in the cross spectral estimate greater than 180 degrees is encountered. This process decreases the influence on the mean radial wind speed estimate of random noise phase shift in higher spectral components.

The horizontal projection of the mean radial velocity

component is

$$\bar{v} = \bar{v}_r \cos(\theta) \quad 2.3.8$$

Data presented here were obtained at small elevation angles ($< 10^\circ$) and therefore $\cos(\theta) \approx 1$. The mean wind speed (v_{lidar}) and azimuth direction (ϕ_{lidar}) are calculated from the following formulas:

$$v_{\text{lidar}} = (\bar{u}^2 + \bar{v}^2)^{\frac{1}{2}} \quad 2.3.9$$

$$\phi_{\text{lidar}} = 180 + \phi_1 + \tan^{-1}(\bar{u}/\bar{v}) \quad 2.3.10$$

where ϕ_1 is the central azimuth angle in the three angle scan of Fig. 2.

2.4 Lidar Uncertainty Estimates in Wind Measurements

An estimate in the experimental uncertainties is needed to judge the reliability of any measurement. Knowledge of the factors contributing to measurement uncertainties can be used to improve experimental procedures. Lidar wind measurement uncertainties are based upon the discreteness of lidar data. Lidar measurements of aerosol profiles are digitized for ease in data manipulation and represent measurements averaged over a range interval of 15m (see Section 3.1). These measurements are acquired at discrete time intervals limited by the laser pulse repetition rate.

The wind speed and azimuth angle (ϕ') between the wind azimuth (ϕ) and the average lidar azimuth (ϕ_{lidar}) (i.e., $\phi' = \phi - \phi_{\text{lidar}}$) can be estimated from the approximate formulas for the velocity components $\bar{u} = \Delta x / \Delta t_m$ and $\bar{v} = \Delta y / \Delta t_m$ by

$$\bar{v} = \sqrt{\bar{u}^2 + \bar{v}^2} = \frac{\Delta x}{\Delta t_m \sin \phi'}$$

2.4.1

$$\phi' = \tan^{-1}(\bar{u}/\bar{v}) = \tan^{-1}(\Delta x / \Delta y)$$

2.4.2

where Δx is the average lateral separation
 Δy is the radial spatial change (units of 15m) of
maximum correlation

Δt_m is the time lag for maximum correlation which is the approximate time interval for the aerosol inhomogeneities to drift the lateral distance Δx .

Quantization uncertainties in lidar wind velocity measurements for fixed value of Δx can be estimated from the following equations. The maximum azimuth quantization uncertainty ($\delta \phi$) is estimated from Eq. 2.4.2 for changes in Δy .

$$\delta \phi = \frac{1}{2} [\phi_{(s)} - \phi_{(s)}] = \frac{1}{2} [t_m^{-1}(\Delta x / 4y_s) - t_m^{-1}(\Delta x / 4y_s)] \quad 2.4.3$$

The maximum quantization uncertainty in the wind speed (δv_g) is estimated from Eq. 2.4.1 for discrete changes in the maximum time lag Δt_m .

$$\delta v_g = \frac{1}{2} [v_{(s)} - v_{(s)}] = \frac{1}{2} \left[\frac{\Delta x}{s_{avg}} \cdot \left(\frac{1}{4c_m} - \frac{1}{4c_m} \right) \right] \quad 2.4.4$$

A schematic diagram of quantization uncertainties in speed and azimuth is shown in Fig. 8. The uncertainties are plotted as functions of wind speed and azimuth angle (ϕ') with respect to the average lidar azimuth direction. The graph represents lidar quantization uncertainties for $\Delta x = 47.9\text{m}$ and a 1 hz laser pulse repetition rate.

Uncertainties in the lidar rms wind speed measurements are estimated by the nonlinear regression (see section 2.3). The nonlinear regression routines estimates the 95% confidence

limits of the regression parameter C_5 . The magnitude of these values are used for lidar rms wind speed uncertainties.

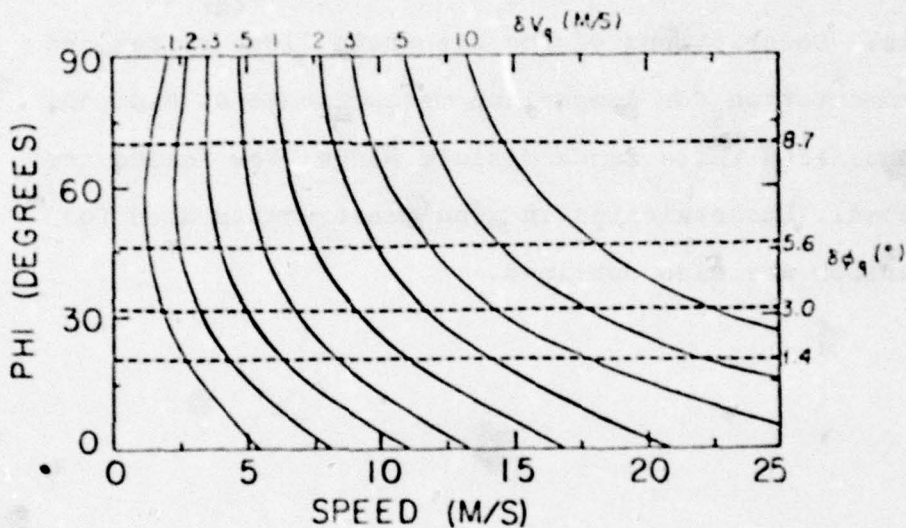


Figure 8: Maximum lidar quantization uncertainties (Eqs. 2.4.3 and 2.4.4) for $\Delta x=47.9\text{m}$ and a 1.0 Hz laser pulse repetition rate. Solid lines are maximum speed quantization uncertainties (m/ssc) and dashed lines are maximum azimuth direction uncertainties (degrees).

3.0 Instrumentation

This chapter gives a brief description of the instrumentation used in obtaining measurements presented in this thesis. Descriptions of the Wisconsin lidar system and instrumentation for comparison measurements at Madison, Wisconsin and White Sands Missile Range, New Mexico are included. Uncertainties in wind measurements used for comparison are also outlined.

3.1 The Wisconsin Lidar System

The Wisconsin Lidar system is operated in a monostatic configuration. A ruby laser pulse is transmitted into the atmosphere and the energy output is measured. The laser radiation scattered through 180 degrees by aerosols and molecules is detected by a receiver telescope aligned parallel to the laser axis. A 1.0 nm bandpass interference filter is used in the receiver optics to suppress the background radiation.

The field of view of the telescope is variable and full overlap of the receiver field of view and the laser beam divergence occurs at approximately 1 km. A red sensitive photomultiplier converts the backscattered laser photons into an electrical signal. The photomultiplier signal is logarithmically amplified to compress the dynamic range and digitized at a 10MHz rate by a Biomation model 1010 10-bit analog to digital converter. The 10MHz rate yields a range resolution of 15 m. The Wisconsin lidar system parameters are listed in Table 1. A block diagram of the system (Fig. 9) is also included.

A PDP 11/40 minicomputer is used for data preprocessing and displaying. Individual lidar returns are corrected for the range square attenuation by adding twice the natural logarithm of the range to each data point. Returns are

Table 1 University of Wisconsin Lidar System Parameters

Transmitter

Wavelength ----- 694.3nm (ruby)
Output Energy ----- 1.0-1.5 J/pulse
Pulse Duration ----- 20ns (Pockels cell Q-switched)
Beam Divergence ----- 1 mrad

Receiver

Telescope ----- .31 Newtonian
Field of View ----- Adjustable (1.5-7 mrad)
Detector ----- RCA C70942K PMT
Quantum Efficiency ----- 0.84 @ 694.3nm
Spectral Bandpass ----- 1.0nm (Interference filter)

Mount positioning

Elevation/Resolution ----- 0.0°-50.0°/(0.1°)
Azimuth/Resolution ----- 0.0°-70.0°/(0.1°)

Data Logging

Amplifier ----- logarithmic (80db)
Digitization ----- Biomation 1010 (10 bit)
Sampling Rate ----- 10 MHz
Range Resolution ----- 15m
Preprocessing ----- PDP11/40 Minicomputer
Output ----- Scope, Digital Magnetic Tape

Trailer Dimensions ----- 8.1 m - Length
2.4 m - Wide
3.3 m - High

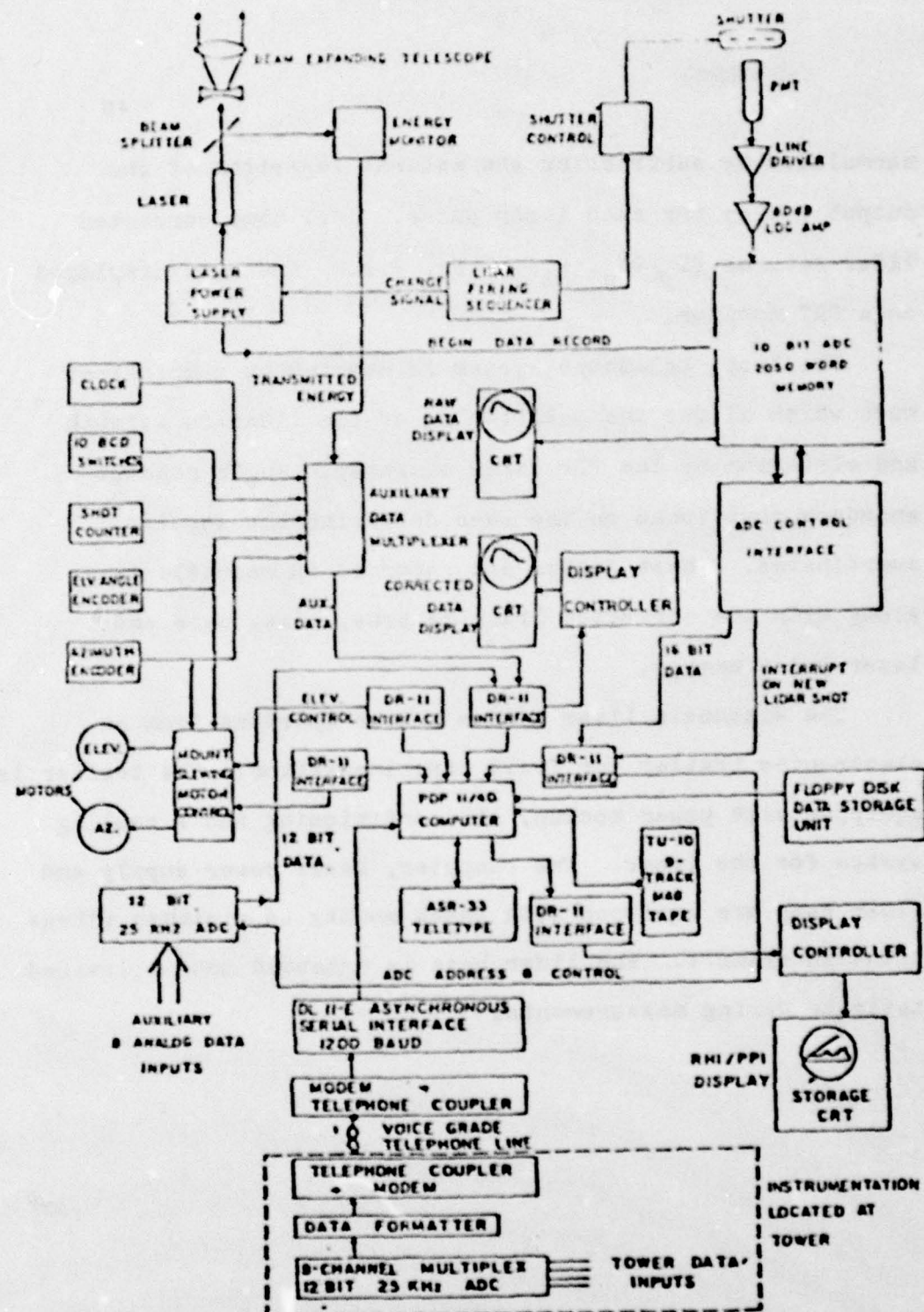


Figure 9: Lidar system block diagram.

normalized by subtracting the natural logarithm of the output energy for each laser pulse. Real time corrected lidar returns ($Y_\phi(t_n, R_1)$ of Eq. 2.1.2) are then displayed on a CRT monitor.

The laser telescope system is mounted on a motorized base which allows the positioning of the lidar in azimuth and elevation by the PDP 11/40 computer. Angle readout encoders positioned on the base determine the angular coordinates. These angles are recorded on magnetic tape along with the corrected lidar returns, time, date and laser pulse energy.

The Wisconsin lidar system can be operated from an electronics trailer for field experimentation. The trailer is equipped with power hookup, air conditioning and a cooling system for the laser. The computer, laser power supply and lidar base are equipped with shock mounts to minimize vibrations in transit. The lidar base is extended onto a lowered tailgate during measurements.

3.2. Tower Wind Measurement Instrumentation

Independent wind measurements in experiments conducted at Madison, Wisconsin were obtained for comparison with lidar derived quantities. A Gill four blade anemometer (R.M. Young model 21002) was mounted at a height of 77m from the base of a radio tower located 2.7 km west of the Meteorology and Space Science Building at the University of Wisconsin, Madison (see Fig. 10). A 12-bit A to D converter is used to digitize the wind speed, azimuth and elevation angles of the bivane sequentially, each at a 1.0 Hz rate. Data transfer to the PDP 11/40 based data logging system (Section 3.1) is done via a telephone modem link. Tower wind data are stored on digital magnetic tape along with concurrent lidar measurements.

A number of factors contribute to the uncertainty in comparison of tower anemometer wind measurements with lidar wind measurements. Sethuraman and Brown (1976) estimate that prop response errors in wind speed measurements are less than approximately 2%. Aerodynamic lifting of the bivane tail produces errors in the angular positioning smaller than two degrees, cf. Pendergast (1975). The supportive tower structure can also influence wind measurements. Wind speed measurements can deviate up to 15% from the mean speed for sensors downwind from the tower according to Izumi and Barad

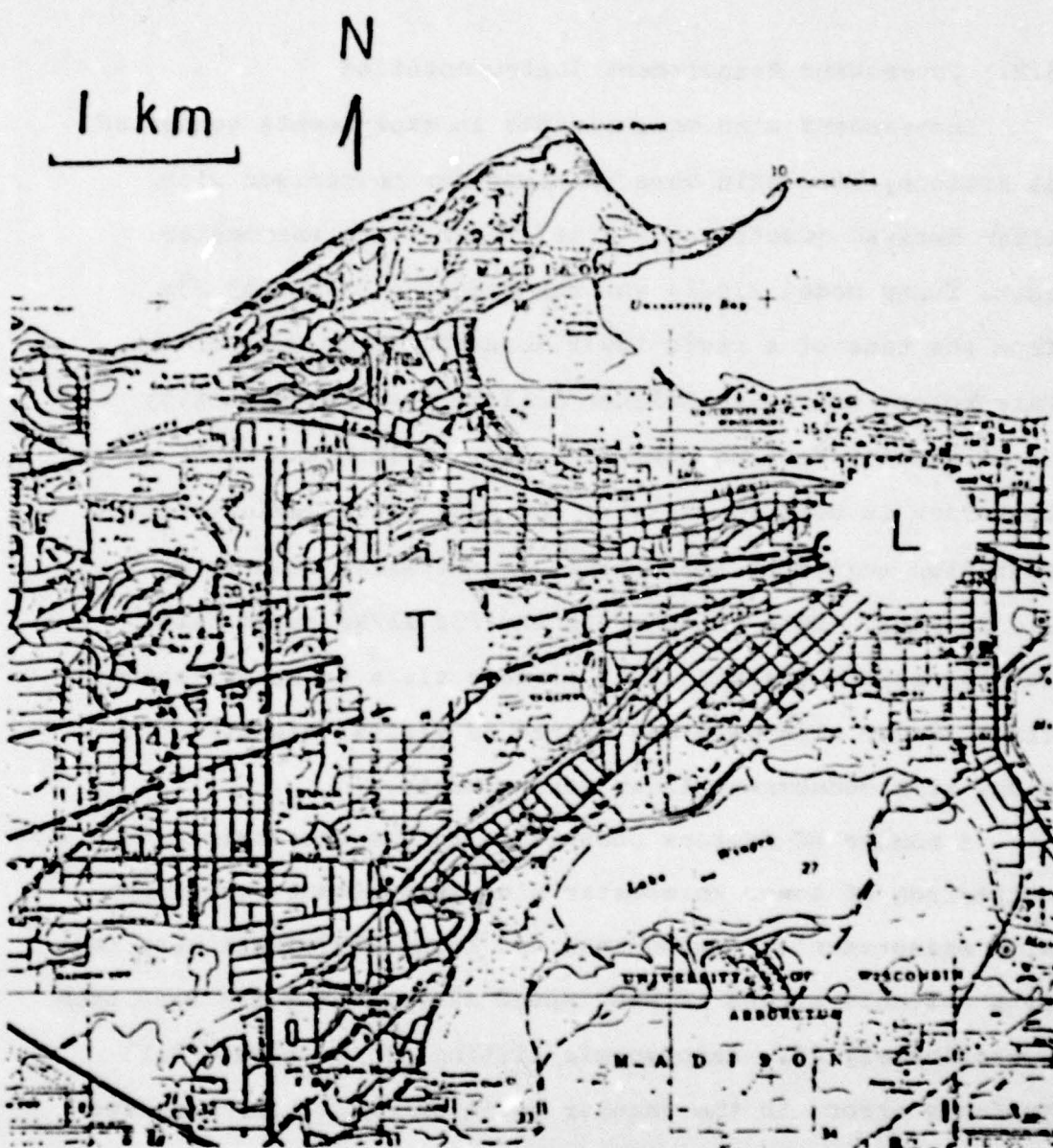


Figure 10: Map of western section of Madison, Wisconsin.
Sites marked T and L are the tower and lidar positions.

(1970). Upwind sensors can be affected up to 8% in a similar manner according to Angell and Bernstein (1976). Tower structure influences upon anemometer wind measurements are estimated to be much smaller than these extreme values in this study. Lidar and tower anemometer wind measurements represent averages over different sample volumes and therefore different statistical sampling. Tower wind measurement uncertainties are based upon the statistical fluctuations in these measurements.

Estimation of tower anemometer wind velocity uncertainties depend upon the correlation of these measurements in time. Error analysis based upon a statistical description is detailed in Appendix D.2. An independent measurement of the average wind field is assumed to be made during a time period equal to the Eulerian time scale (τ_e) for stationary isotropic turbulence. The uncertainty in the measure of the mean value of a wind parameter is estimated by Eq. D.2.3 to be

$$\bar{\sigma}_p' = \sigma_p / (N_r)^{1/2} \quad 3.2.1$$

where $\bar{\sigma}_p$ is the standard deviation of the parent population for parameter p

σ_p' is the uncertainty in the mean value of the parameter p

N_T is the number of independent measurements in a time interval of length T ($N_T = T/\bar{\tau}_e$, cf. Eq. D.2.2)

Uncertainties in the tower wind measurements are listed in Section 4.1 for each experimental day.

3.3 White Sands Missile Range Instrumentation

Independent wind measurements for comparison to lidar wind measurements were obtained for experiments conducted at the White Sands Missile Range, New Mexico. A map of the experimental site at White Sands Launch Complex #36(LC36) is shown in Fig. 11. Wind velocity measurements from an instrumented meteorological tower and radar tracked pilot balloons are used in this thesis for comparison. Experiments were conducted from December 7-17, 1977 and January 7-27, 1978.

The meteorological tower at the LC36 site was instrumented for wind measurements with the following equipment: cup anemometers were at eight height levels of the tower (7.6, 23, 38, 53, 69, 91, 122, 152 m). Measurements from the cup anemometers were averaged every 15 seconds and recorded on paper tape. Two U-V-W anemometers (R.M. Young model 27003) were located at heights of 14 and 137 m. Wind measurements from these two anemometers were acquired by the same data transfer system described in Section 3.2 and stored along with lidar measurements.

Wind measurements from automatically tracked pilot balloons were used for comparisons with lidar wind profile measurements above the tower. Pilot balloon measurements are vertically averaged over heights of 100 m. Averaging pilot balloon measurements in this manner yields the same vertical averaging

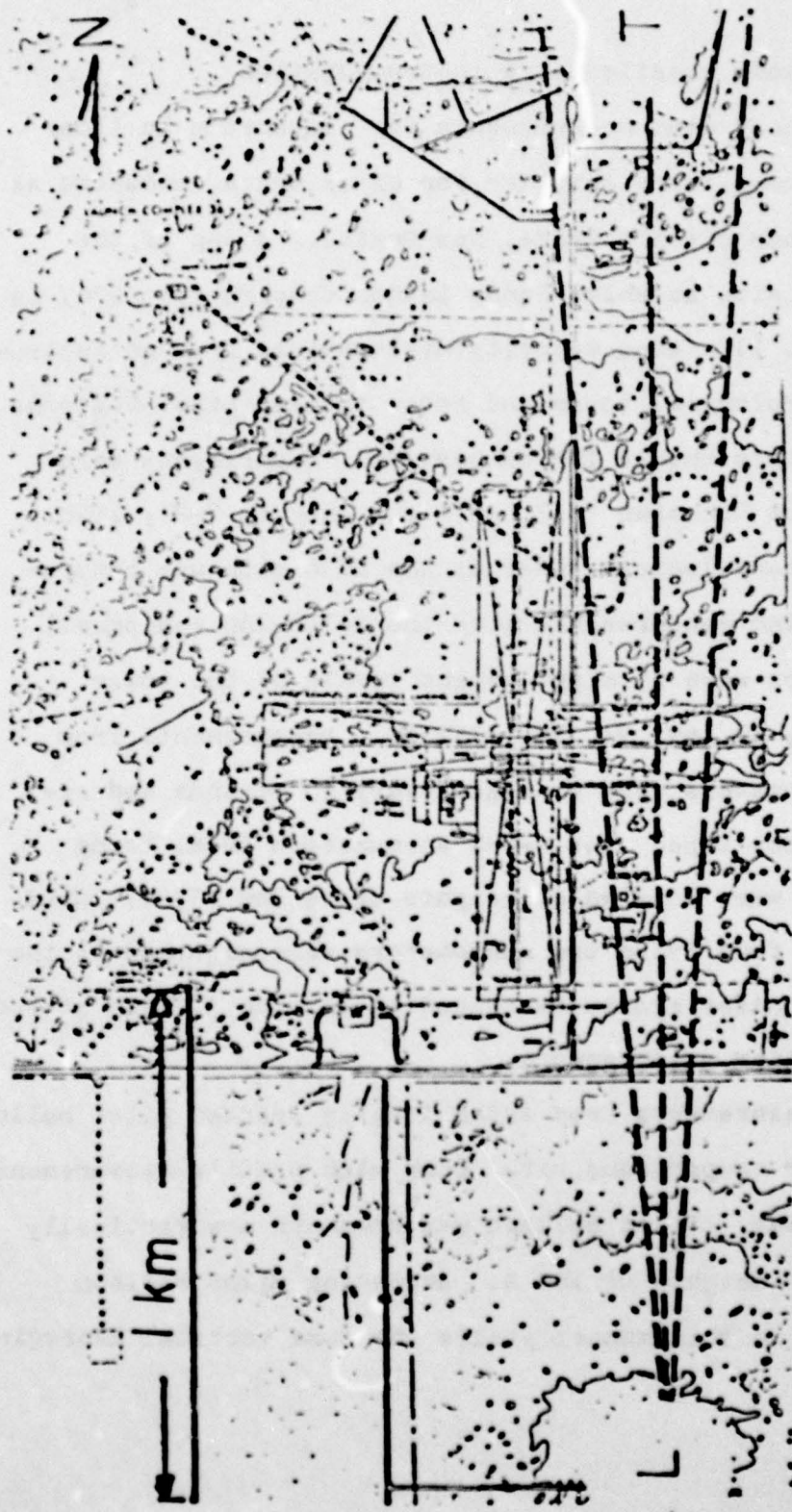


Figure 11: Map of Launch Complex #36(LC36), experimental site at White Sands Missile Range, New Mexico. Lidar and tower positions are marked L and T.

as lidar wind measurements and smooths over variations in wind velocities due to mutations in the radar dish. Pilot balloon measurements were obtained every 10 minutes for the data presented here.

Uncertainties in average pilot balloons wind measurements can be estimated from inaccuracies in the average spatial displacement of the balloons in time. Displacement errors can occur because of erratic motion of these balloons due to short time scale turbulent gusts and aerodynamic forces upon the balloon during ascent, cf. Rider and Armendariz (1968), Rogers and Camnitz (1966). Displacement errors also occur because of positioning inaccuracies due to equipment resolution, see Schaefer and Doswell (1978). Pilot balloon wind velocity uncertainties are estimated in this thesis from positioning errors in space.

Pilot balloon wind velocity measurement uncertainties are derived in Appendix D.1 for spatial positioning errors. The maximum uncertainty in each velocity component δU_{\max} , δV_{\max} is

$$\delta U_{\max}, \delta V_{\max} = a \frac{\delta R}{\delta t} + a \bar{R} \frac{\delta \theta + \delta \phi}{\delta t} \quad 3.3.1$$

where \bar{R} is the average slant range of the pilot balloon during the measurement

δR is the uncertainty in the slant range measurement

δt is the time interval of the measurement

$\delta\theta$ is the uncertainty in the elevation angle

$\delta\phi$ is the uncertainty in the azimuth angle

(This is Eq. D.1.4).

Information on the range and angular resolution of the radar units used in balloon tracking was not available at the time of this writing. An estimate of the angular resolution of 0.1 degrees was obtained from an estimate of the diffraction limit of the receiver. The differential range resolution was estimated to be no greater than 5 m. Eq. 3.3.1 reduces to the following for these resolution values.

$$\delta U_{max} : \delta V_{max} : 0.66 + 0.039 \bar{R} \text{ (m/s)} \quad 3.3.2$$

The uncertainties in pilot balloon wind speed and direction from the average wind profile can be estimated using Eq. 3.3.2. The average radial slant range (\bar{R}) can be calculated from the average height and horizontal displacement of the balloon from the mean wind profile. Variations in each wind velocity component are estimated from Eq. 3.3.2. Uncertainties in wind speed and direction are calculated from the variations in each component using Eqs. 2.3.9-10. Uncertainty estimates are listed in Section 4.2.

4.0 Experimental Results

Experiments were conducted in Madison, Wisconsin and at the White Sands Missile Range, New Mexico to test the theory presented in Chapter 2. Aerosol density inhomogeneity scale sizes from 60 m to 1 km were found to be efficient wind tracers. These experimental results represent the mean motion of the aerosol inhomogeneities over a five minute period. Uncertainty estimates of the wind velocity are listed for both lidar and comparisons measurements. Results show that lidar can measure the spatial and temporal variations in the wind velocity field.

4.1 Madison Experiments

Comparisons of lidar and tower anemometer wind velocity measurements were conducted in Madison, Wisconsin from April through August 1977. Remote lidar measurements were obtained over the western section of Madison (see Fig. 10). The Wisconsin lidar system was located on the ninth floor of the University of Wisconsin Meteorology and Space Science Building. Results of these experiments are for convective days with well defined inhomogeneities in the mean aerosol structure. Aerosol inhomogeneities are of sufficient magnitude under these conditions to be detectable above the background noise of the system. A signal to noise ratio (SNR) defined from Eq. 2.2.5 of greater than 0.5 occurred for the data presented in this section.

Lidar profiles of aerosol inhomogeneities were obtained in the three angle azimuth scan described in Section 2.1. Lidar measurements were acquired with a 1.0 degree azimuth beam separation at an elevation angle of 2.3 degrees for each day. The tower anemometer location (shown in Fig. 10) was located near the center of the azimuth scan pattern. A data segment length of 960 m (64 data points) centered about the tower distance (2.7 km) was used in analysis of wind information. The average lateral beam separation (Eq. 2.1.5) was 47.9 m. The period between successive lidar aerosol inhomogeneity profiles was limited by laser cooling requirements

to 1.1 seconds. Lidar wind measurements represent five minute time averages over a sample volume 960 m long by 47.9 m wide by 17 m high.

Lidar aerosol measurements were analyzed for wind velocity information by the method outlined in Chapter 2 and compared with concurrent tower anemometer wind measurements. The experimental time duration of each day varied between 20 to 45 minutes so that a number of five minute wind velocity averages could be computed. Uncertainties in lidar wind measurements are estimated according to Section 2.4.

Uncertainties in tower anemometer measurements (see Section 3.2) are estimated as follows. The Eulerian speed autocorrelation is calculated from the tower measurements over the entire time duration of the experiment. The Eulerian time scale is estimated as the time integration of the speed autocorrelation function to a time where this value is approximately zero. Uncertainties in the measurement of the average tower speed $\bar{S}V_T$ and azimuth direction $\bar{\phi}_T$ are estimated by, cf. Eq. 3.2.1.

$$\bar{S}V_T = \bar{\sigma}_v' = \bar{\sigma}_{vv} (\tau_e/\tau)^{1/2}$$

4.1.1

$$\bar{S}\phi_T = \bar{\sigma}_\phi' = \bar{\sigma}_{\phi\phi} (\tau_e/\tau)^{1/2}$$

4.1.2

where ζ_e is the Eulerian time scale

T is the time duration of the entire experiment

\bar{C}_{ST} is the tower rms wind speed calculated over the entire experimental time duration

$\delta V_T : C'_T$ is the uncertainty in the average tower wind speed measurement V

$\bar{C}_{\phi T}$ is the rms tower wind azimuth direction calculated over the entire experimental time duration

$\delta \phi_T : C'_\phi$ is the uncertainty in the average tower wind azimuth direction

The rms wind parameters determined for the experimental duration (T) are assumed to approximate the standard deviation of the parent populations. Uncertainties in the measurement of the five minute averaged tower rms wind speed estimates are calculated as the standard deviation of these measurements from the rms wind speed calculated for the entire time period (\bar{C}_{ST}).

$$\delta \bar{C}_{ST} = \frac{1}{M_T} \left[\sum_{i=1}^{M_T} (\bar{C}_{ST} - \bar{C}_{S_i})^2 \right]^{1/2} \quad 4.1.3$$

where M_T is the number of five minute average wind measurements for each experiment

\bar{C}_{S_i} is the tower rms wind speed measured over a five minute average

σ_{C_T} is the uncertainty in the tower estimation of for each experiment

These uncertainties in tower anemometer measurements are listed in Table 2.

The results of these experiments are summarized as time histories of wind speed, azimuth direction and rms wind speed of lidar and tower anemometer measurements in Figs. 12-17. Wind speeds and directions are calculated by Eqs. 2.3.9 and 2.3.10. The average difference between lidar and tower measurements of the mean wind speed and azimuth direction as well as the standard deviations of these errors are listed in Table 2 for each experimental day. These are calculated from the following formulas:

$$\Delta V = V_{\text{lidar}} - V_{\text{tower}} \quad 4.1.4$$

$$\Delta \phi = \phi_{\text{lidar}} - \phi_{\text{tower}} \quad 4.1.5$$

$$\bar{\Delta}V = \frac{1}{m_T} \sum_{i=1}^{m_T} \Delta V_i \quad 4.1.6$$

$$\bar{\Delta}\phi = \frac{1}{m_T} \sum_{i=1}^{m_T} \Delta \phi_i \quad 4.1.7$$

$$\Delta V_{\text{ens}} = \frac{1}{m_T-1} \left[\sum_{i=1}^{m_T} (\Delta V_i - \bar{\Delta}V)^2 \right]^{1/2} \quad 4.1.8$$

$$\Delta \phi_{\text{ens}} = \frac{1}{m_T-1} \left[\sum_{i=1}^{m_T} (\Delta \phi_i - \bar{\Delta}\phi)^2 \right]^{1/2} \quad 4.1.9$$

Table 2. Summary of Madison Experiments

Parameter/Date	4/22	5/23	6/20	6/23	6/27	7/26
\bar{V} (m/s) Average wind speed	8.0	3.8	7.0	6.6	4.4	2.2
$\bar{\sigma}_v$ (m/s) Standard deviation of wind speed for experiment	1.3	0.9	1.1	1.5	0.9	0.4
$\bar{\theta}^*(\circ)$ Average wind azimuth	48.	169.	13.	200.	203.	351.
$\bar{\sigma}_{\theta^*}$ (\circ) Standard deviation of wind azimuth for experiment	6.	11.	10.	10.	11.	6.
\bar{T} (sec) Euler-mean time scale	30.	16.	14.	35.	17.	31.
$\bar{\Delta V}$ (m/s) Average 0.2 speed difference between lidar and tower measurements	0.2	0.4	1.2	-0.8	0.7	0.2
ΔV_{avg} (m/s) RMS wind speed difference between lidar and tower	0.3	0.2	0.7	0.9	0.6	0.2
$\bar{\delta}V$ (m/s) Lidar quantization uncertainty in wind speed	1.5	0.7	2.8	0.9	0.7	0.2
$\bar{\delta}\theta^*$ (\circ) Uncertainty in tower wind speed	0.4	0.2	0.3	0.5	0.2	0.1
$\bar{\delta\theta^*}$ (\circ) Average lidar tower azimuth difference	-6.	7.	-4.	5.	8.	20.
$\bar{\delta\theta^*}$ (\circ) Wind azimuth difference between lidar and tower	4.	6.	3.	8.	4.	2.
$\bar{\delta\theta_q^*}$ (\circ) Lidar quantization azimuth uncertainty	5.	4.	9.	7.	7.	9.
$\bar{\delta\theta_t^*}$ (\circ) Uncertainty in tower wind direction	3.	3.	2.	4.	3.	3.
$\bar{\delta\theta_{avg}}$ (\circ) RMS tower wind speed uncertainty	0.2	0.4	0.2	0.6	0.2	0.1
$\bar{\delta\theta_{lidar}}$ (\circ) Lidar RMS speed uncertainty	0.1	0.2	0.2	0.1	0.1	0.1

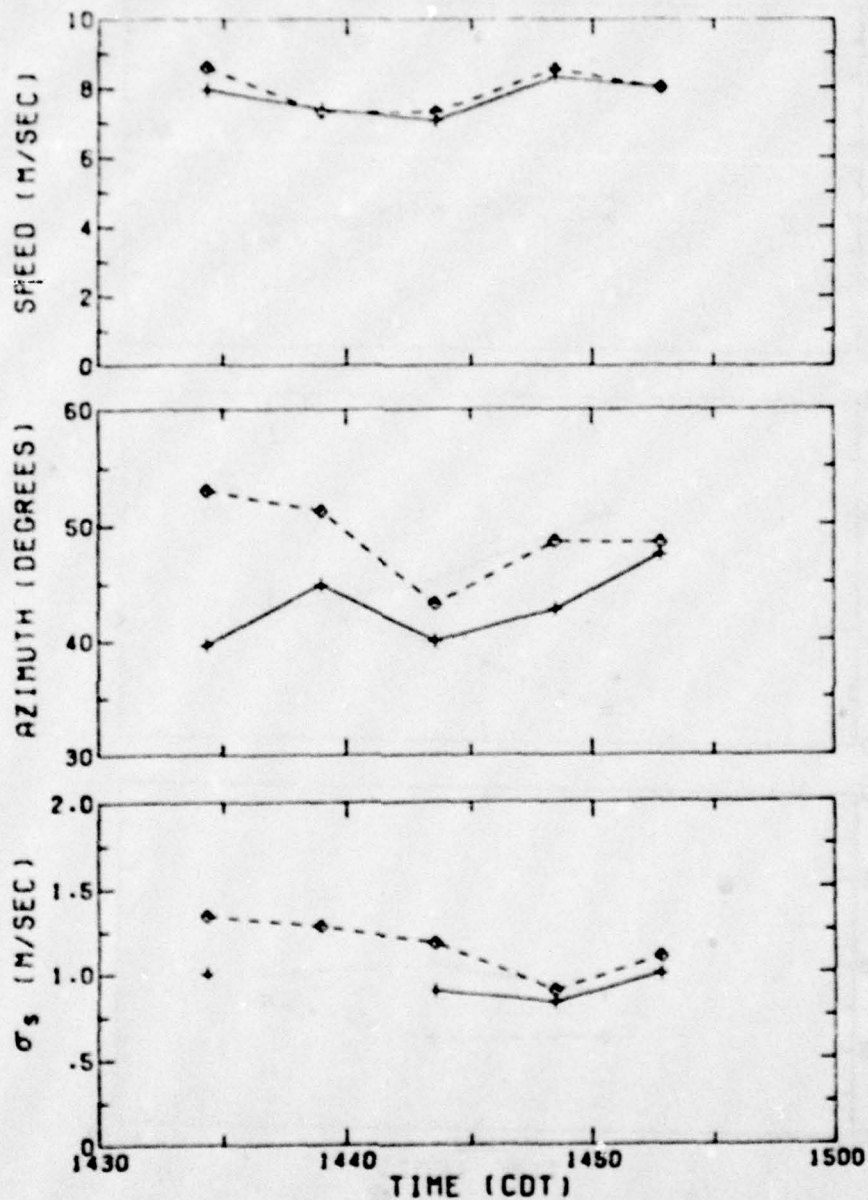


Figure 12: Comparisons of lidar (+, solid) and tower (o, dashed) a) speed, b)azimuth (from north) and c) σ_s versus time for 22 April 1977. Data obtained in Madison. All measurements made at the tower anemometer height (77m). RMS wind speed for the second data point is not plotted because the coherence maxima were nearly as low as those corresponding to a 5% random noise coherence (Eq. A2.2).

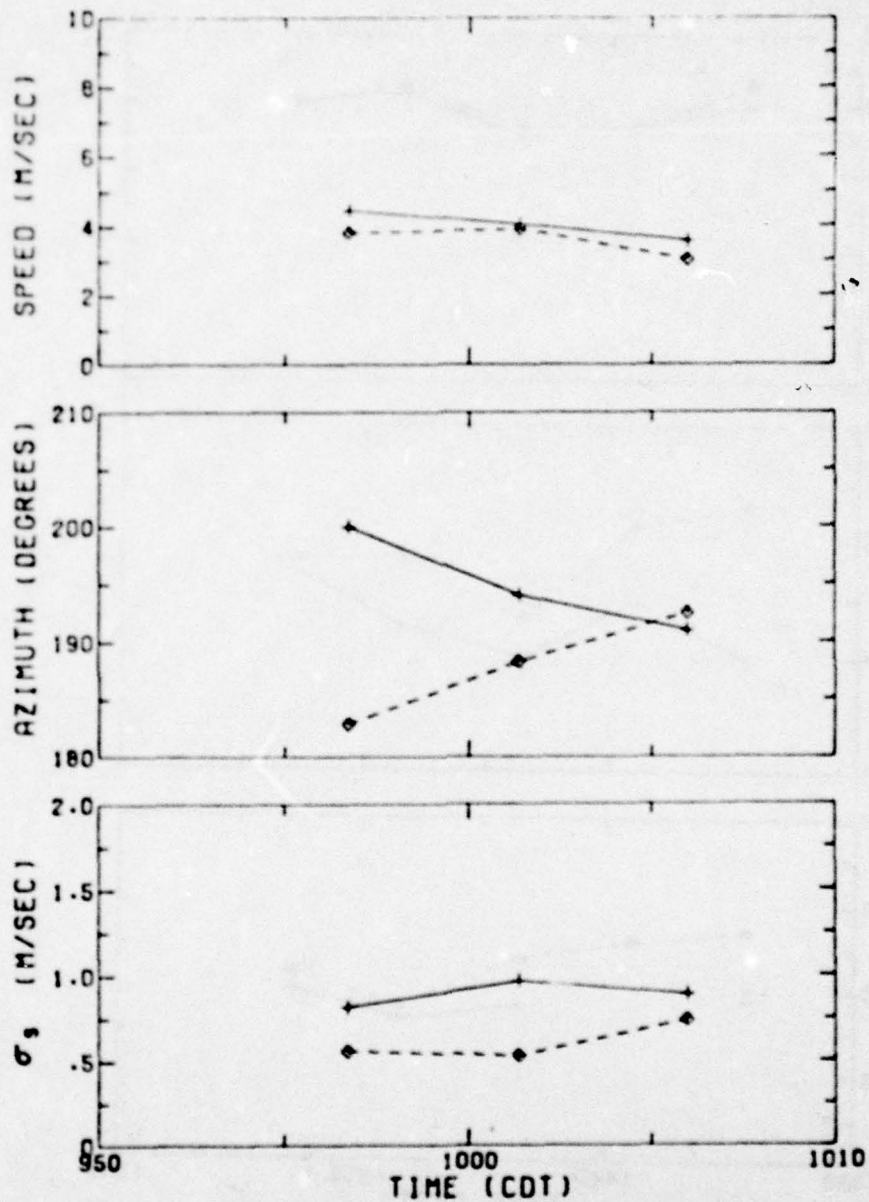


Figure 13: Similar graph as Figure 12 for data obtained on 23 May 1977 in Madison. Larger lidar measured radial wind speeds contribute to larger azimuth differences for first data point (further explanation on page 61).

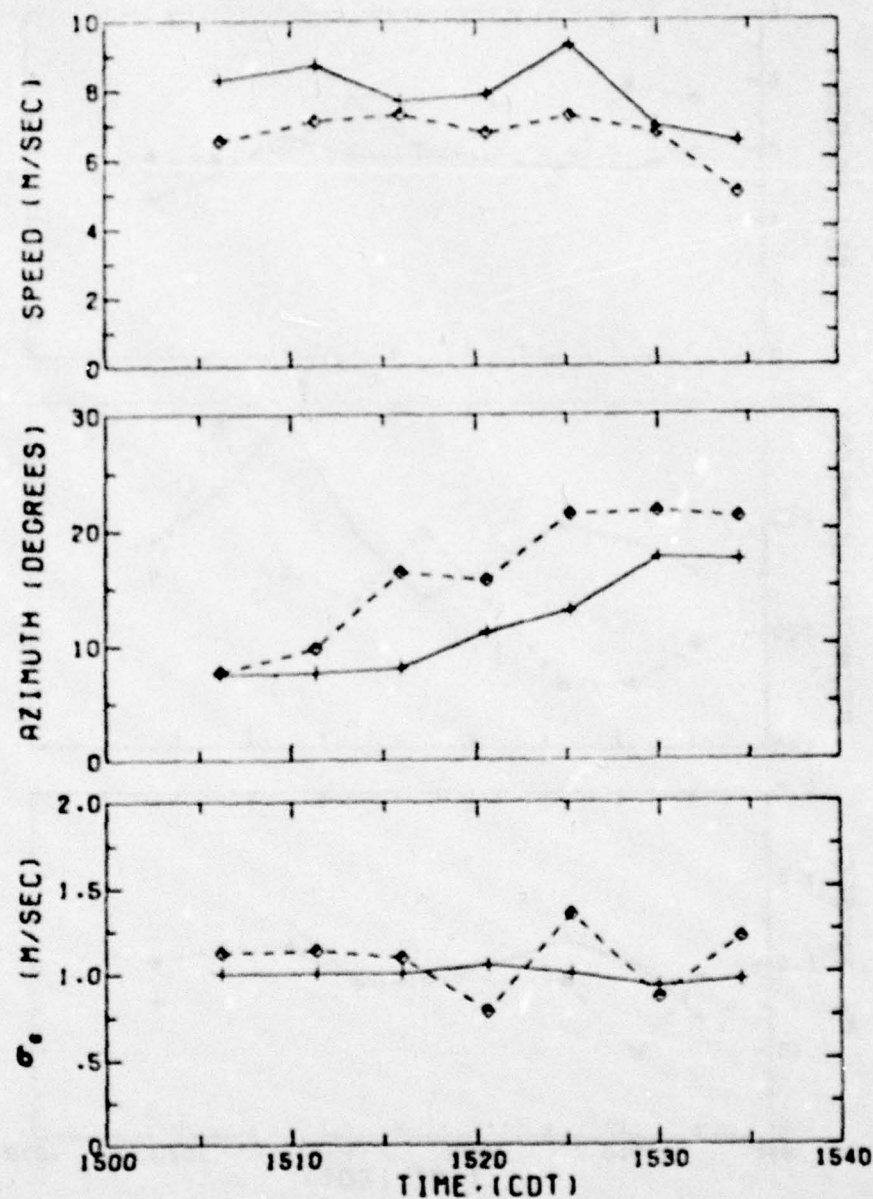


Figure 14: Same as Figure 12 for 20 June 1977.

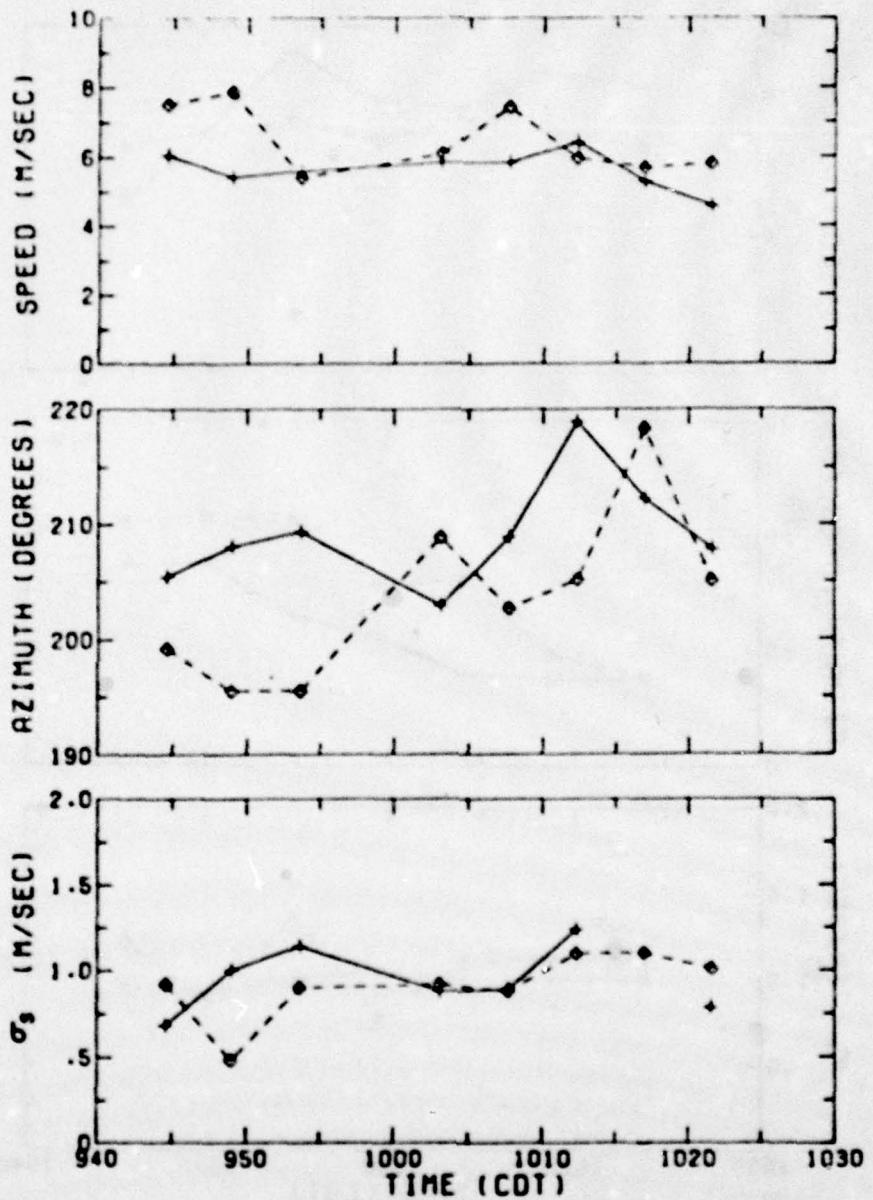


Figure 15: Similar plot of lidar and tower comparison for 23 June 1977. Note that non-linear regression converged to lower bound in sigma for second to last data point. This data point is not plotted (see page 61).

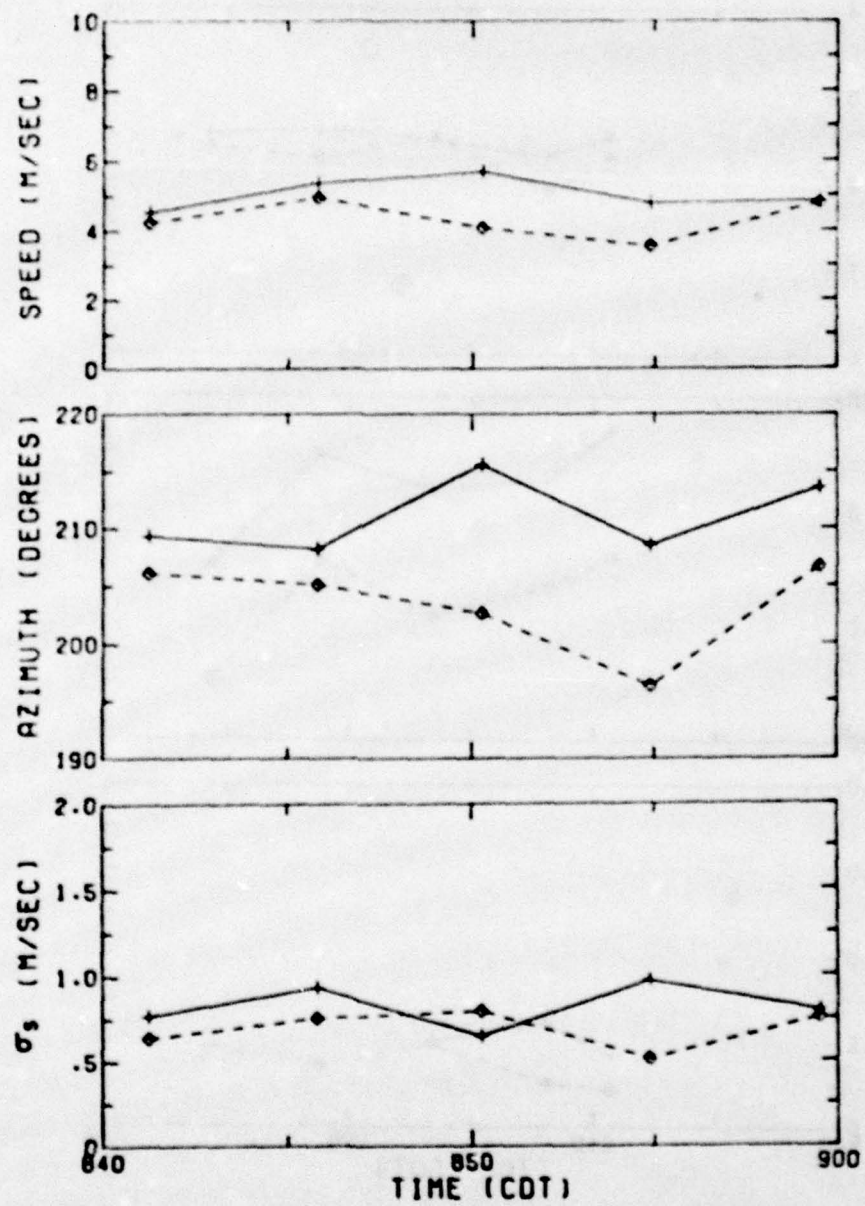


Figure 16: Similar graph as Figure 12 for data obtained in Madison on 27 June 1977.

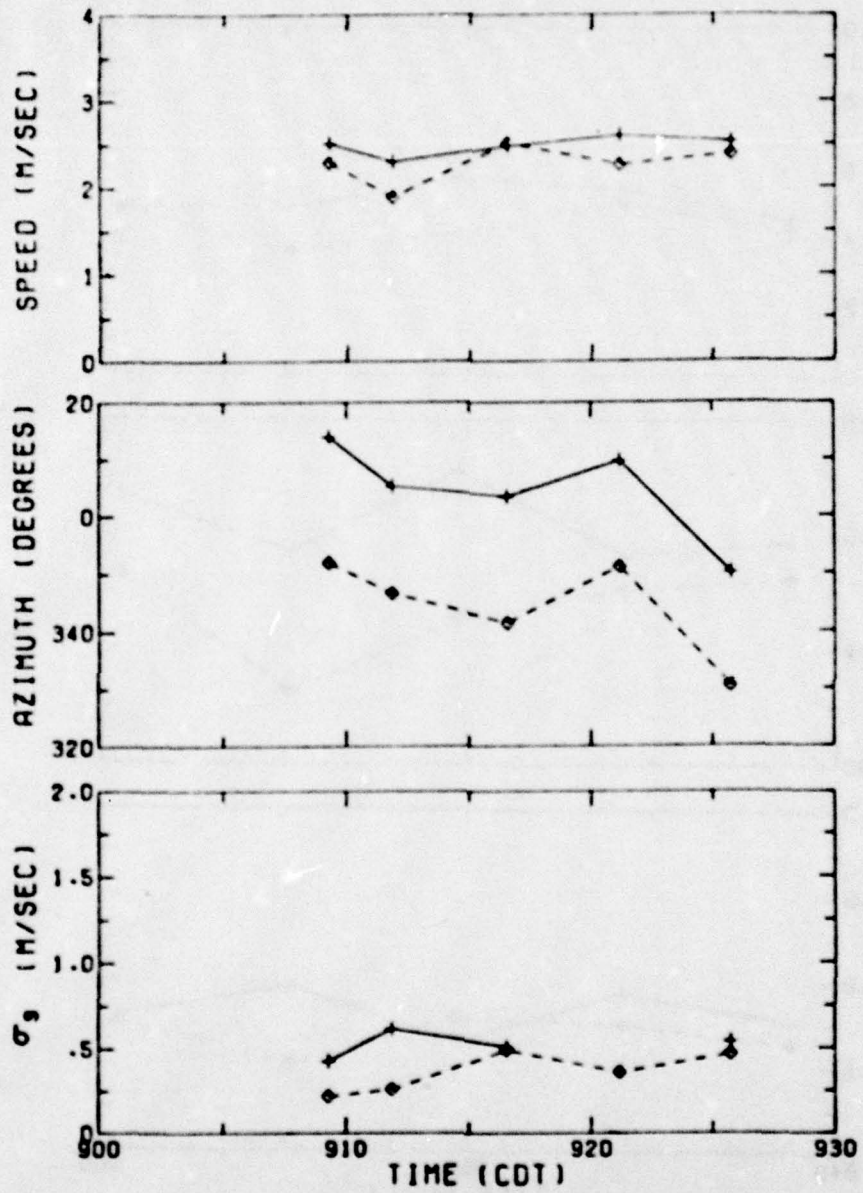


Figure 17: Similar to Figure 12 for 26 July 1977. Non-linear regression converged to lower bound in sigma due to low SNR for second to last point. This data point is not plotted. (see page 61).

where these parameters are described in Table 2. The average lidar quantization uncertainties are also listed in Table 2.

Figs. 18, 19, and 20 are comparisons of lidar and tower anemometer measurements of the wind speed, azimuth direction and the rms wind speed, respectively. Average uncertainties in both lidar and tower measurements for each experiment are also shown. These graphs show that lidar wind measurements are consistent with concurrent tower wind measurements.

Some limitations of this procedure for remote lidar wind measurements were discovered while investigating measurements with large discrepancies. The process of removing the mean aerosol structure (Eqs. 2.1.3-2.1.4) bias against detecting small radial displacements. Aerosol inhomogeneities do not have time to drift the radial distance between data points (15 m) in the time for them to drift laterally between beams. This occurs for radial wind speeds typically less than a meter per second. The large discrepancies in azimuth on May 23 and July 26 can be explained by the overestimation of lidar radial wind speeds. Lidar azimuth quantization uncertainties are large in these instances.

Extremely low values of lidar measured rms wind speeds on April 22, June 23 and July 27 were found to have low SNR values (.5-.7). The coherence maxima in these cases were the same order of magnitude as the 5% probability coherence for

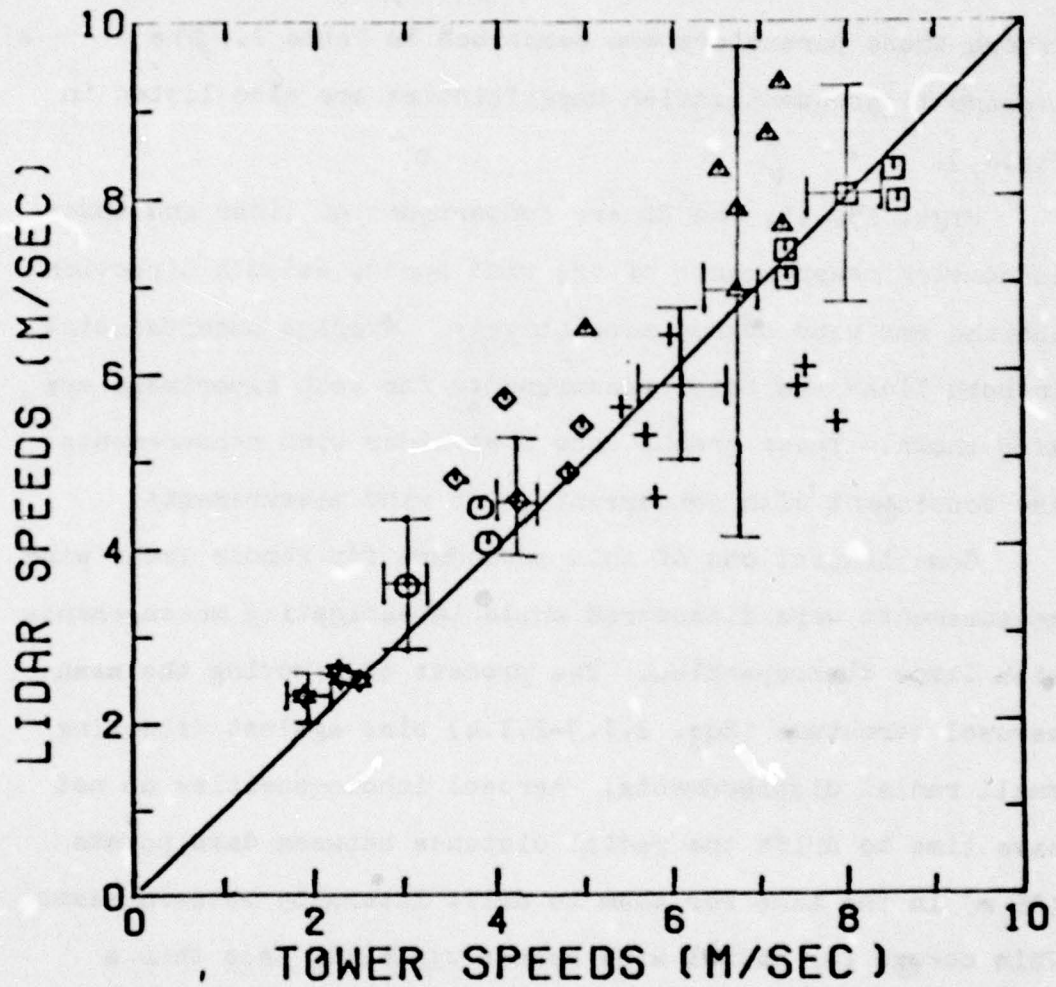


Figure 18: Comparisons of lidar and average tower anemometer wind speeds for April 22 (\square), May 23 (\circ), June 20 (Δ), June 23 (+), June 27 (\diamond), and July 27 (*), 1977. Data segments were obtained on clear, convective days. Lidar and tower uncertainties are shown for each experimental day.

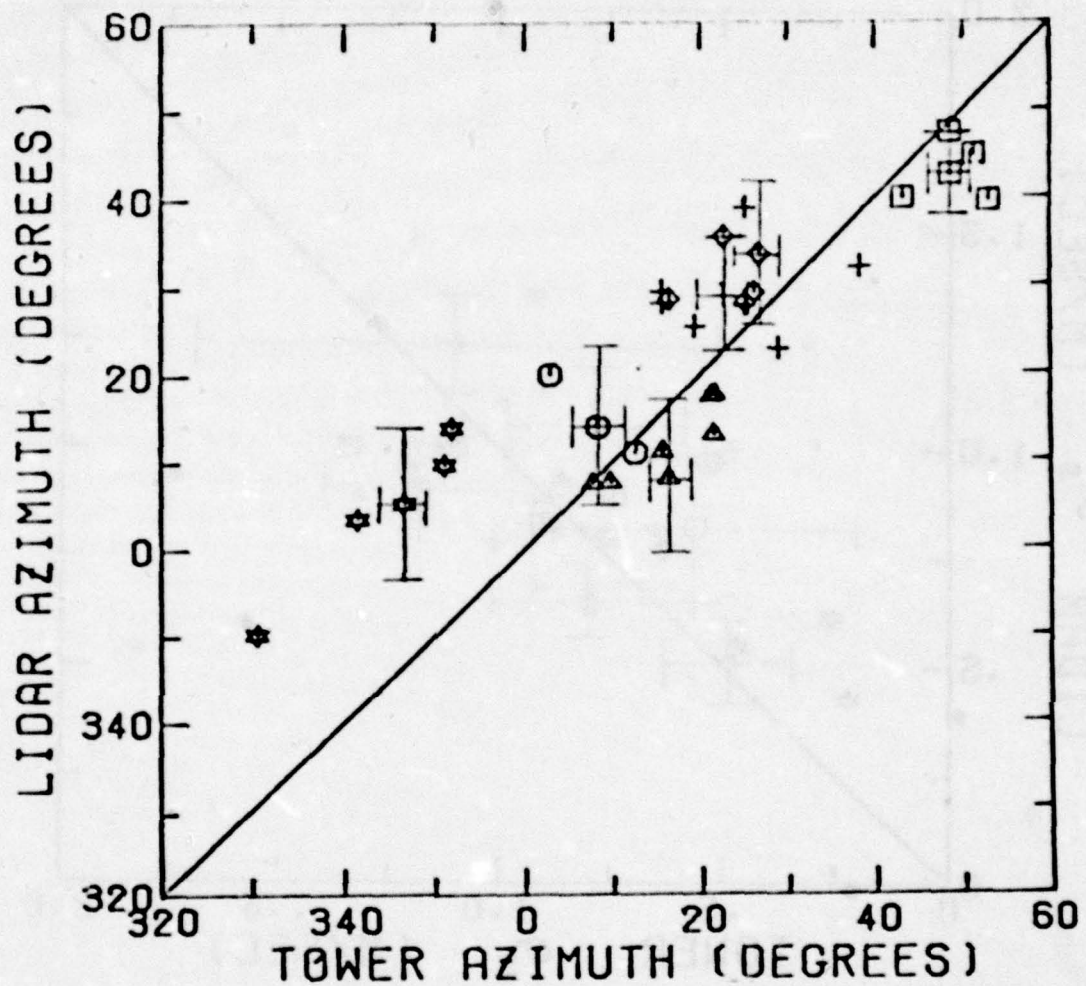


Figure 19: Similar plot to Figure 18 for the azimuth angle (degrees from North). Lidar and tower azimuth uncertainties are also shown. Note: Data on May 23, June 23, and June 27 are plotted for the opposite direction, i.e., 180 degree difference.

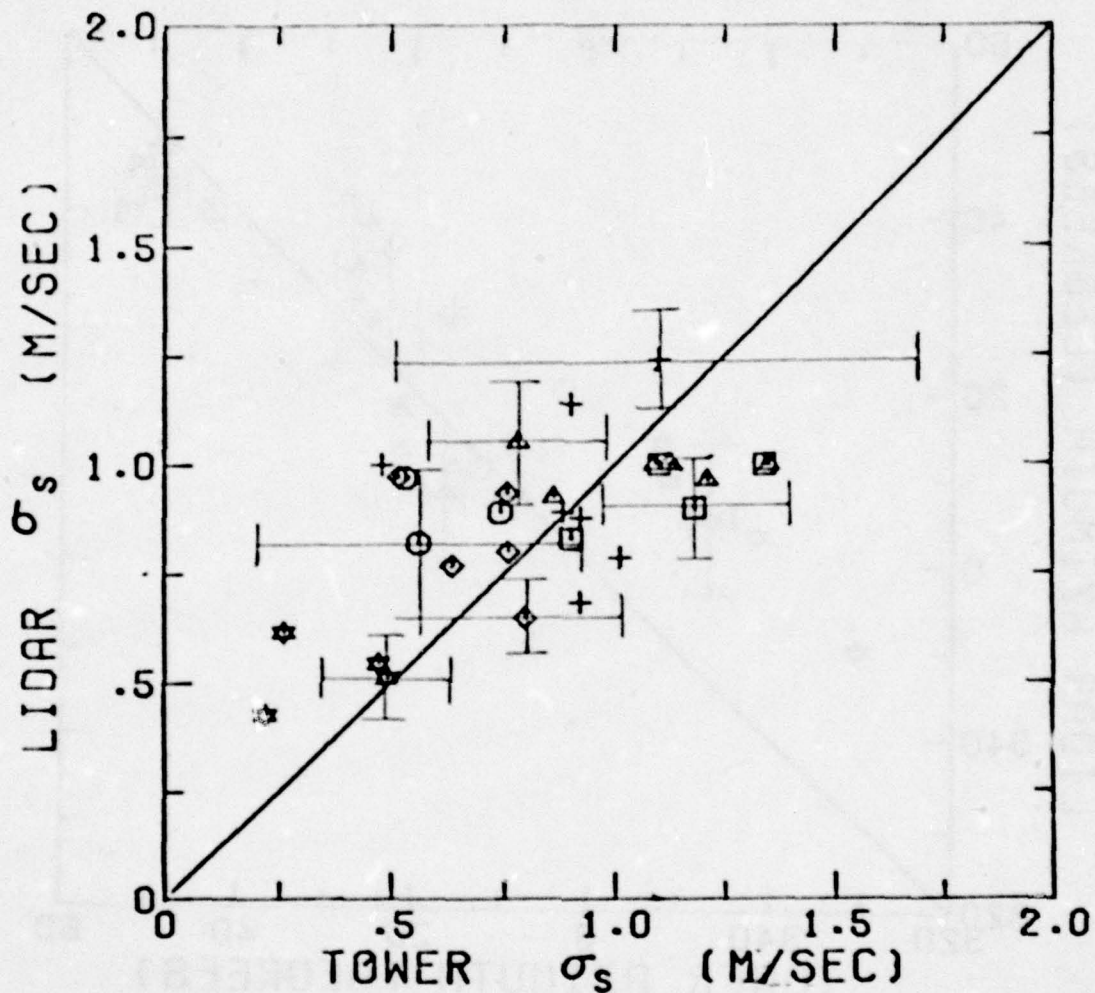


Figure 20: Similar plot of rms wind speed for the data of Figure 18. Lidar and tower uncertainties for each experimental day are also shown. Values where the non-linear regression converged to very low values because of low SNR values (see page 61) are not plotted.

random fluctuations predicted by Eq. A.2.2. These coherence maxima were found not to decrease with increasing lateral separation as in Fig. 7. Wind speeds and directions calculated from this data were found to be consistant with previous measurements, however the nonlinear regression converged to very low values to minimize the residue in the regression. These measurements of the rms wind speed are not plotted because of the large uncertainty in the regression of this parameter.

4.2. White Sands Experiments

A field experiment was conducted in conjunction with the Atmospheric Science Laboratory at the White Sands Missile Range, New Mexico. Remote lidar wind measurement experiments were conducted on the dates December 7-17, 1977 and January 7-22, 1978. Fig. 11 is a map of the experimental area. The Wisconsin lidar system was located 2.7 km south of the Launch Complex #36 (LC36) meteorological tower. Instrumentation for tower wind measurements are described in Section 3.3.

The experimental procedure for obtaining remote lidar wind measurements was similar to that used in the Madison experiments (Section 4.1). The three angle azimuth scan described in Section 2.1 is used with an azimuth separation between lidar return aerosol profiles of one degree. The lidar elevation angle was positioned at 6 degrees for height profiles of wind velocity. The length of the data segments (64 points, 960 m), laser firing period (1.1 seconds) and time duration for each measurement (5 minutes) are the same as those used in Section 4.1.

Height profiles of wind velocity correspond to lidar measurements at different ranges along the propagation path. Average height levels of lidar measurements are calculated from Eq. 2.1.6. The volume over which lidar wind measurements are averaged varies because the lateral separation increases

with increasing range. The average lateral separation varies from 21 m at a slant range of 1.2 km to 99 m at 5.7 km. The vertical and longitudinal lengths of the sampling volume are 100 m and 960 m, respectively, for all ranges.

Wind velocity measurements from lidar data are calculated using the theory in Chapter 2. Wind velocity height profiles are measured using nonoverlapping data segments. The lowest height level is limited by the range for complete overlap between the laser beam divergence and the field of view of the receiver. Uncertainties in lidar wind measurements are estimated according to Section 2.4.

Measurements presented in this section were obtained from 1620-1720 MST on January 19, 1978. Very light snow with large scattering cross section in the visible was observed to fall throughout the period (visibility 8 km). Large variations in the return lidar signal were observed to a range of 6 km. Lidar observations at higher elevation angles showed multiple cloud levels with the lowest at approximately 800 m. This data was chosen to illustrate the capabilities of lidar in cases of high signal to noise ratios (SNR).

Results from this data are shown in Figs. 21-26. Each graph consists of height profiles of wind speed, azimuth direction and rms wind speed for lidar and pilot balloon measurements. Pilot balloon measurements are plotted for balloons before, during, and after lidar measurements, when

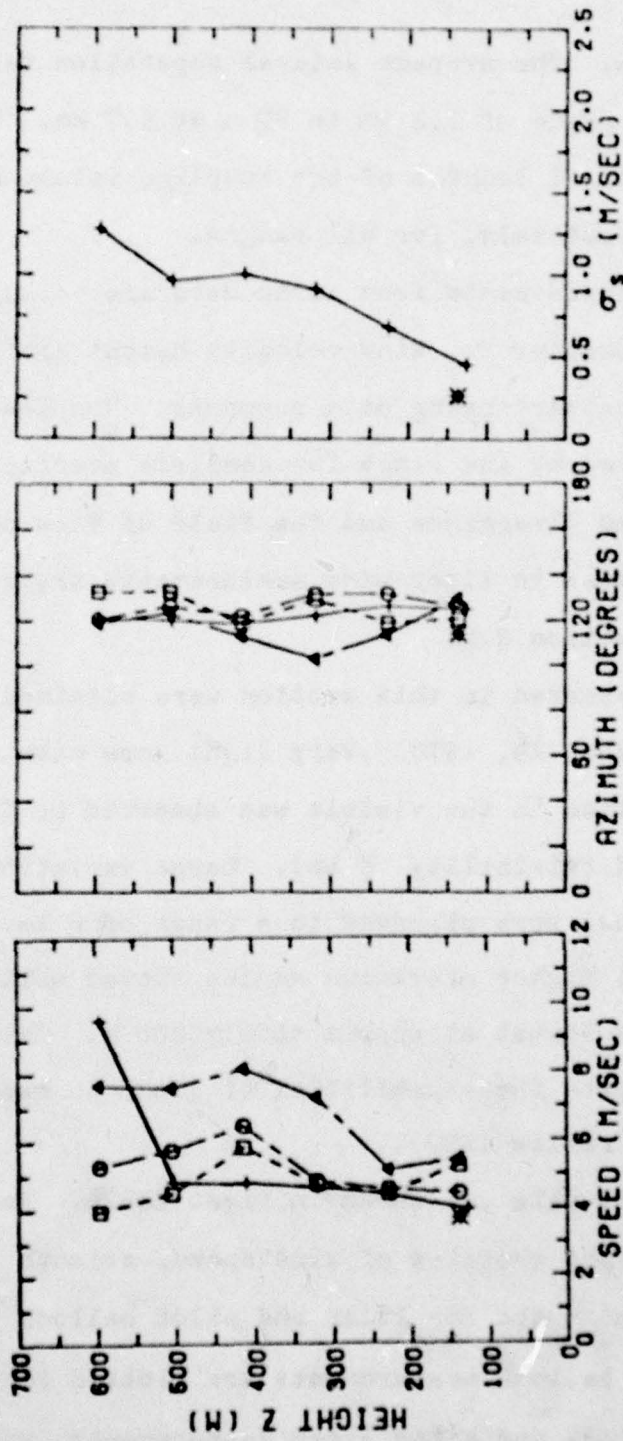


Figure 21: Comparisons of lidar (+, 1633-1638MST) and pilot balloon (\square , 1625-1627MST, \circ , 1635-1637MST, Δ , 1645-1647MST) for wind speed, azimuth and rms wind speed, G_s , as functions of height, Z (m). Data obtained under conditions of light snow on January 19, 1978 at White Sands Missile Range. Tower anemometer measurements (*) for the 137m level are also shown. The coherence measurements at the 594m level showed broad peaks with multiple maxima. High lidar wind speed at this level is discussed on page 74.

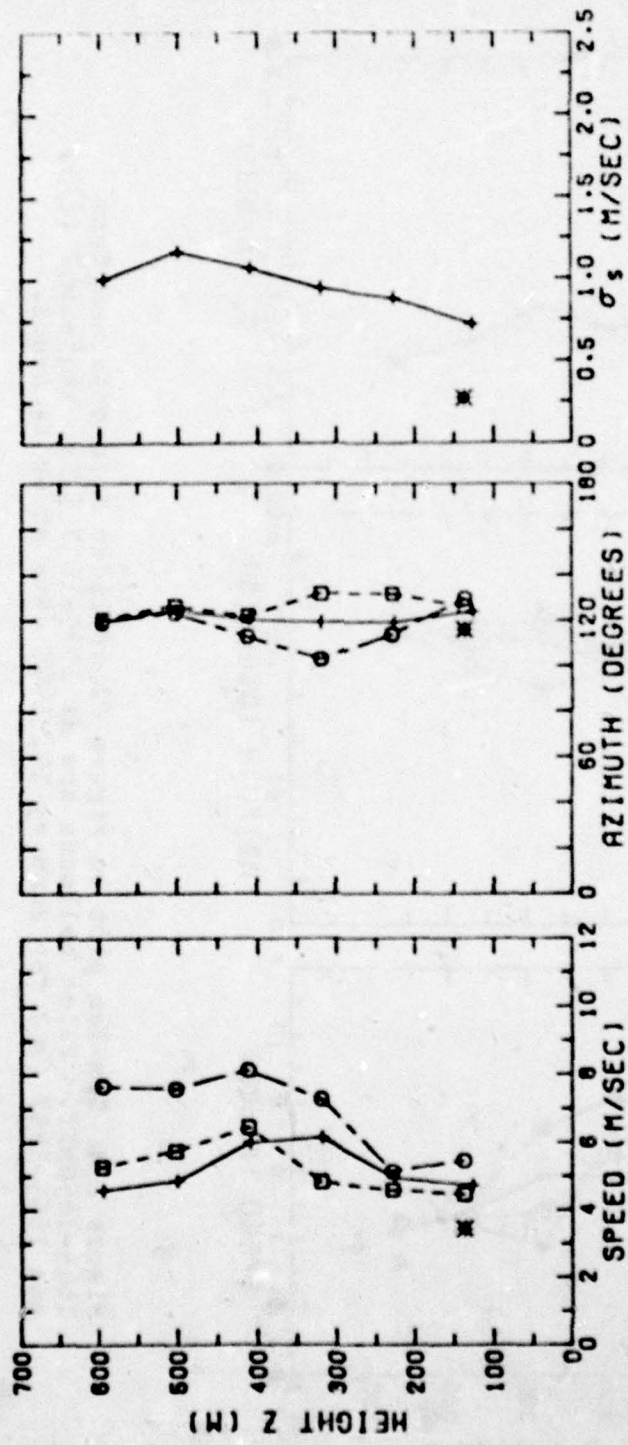


FIGURE 22: Similar plot to Figure 21 of lidar data obtained from 1639-1641MST. Pilot balloons are at 1635-1637 (\square) and 1645-1647 (\circ) for January 19, 1978 data at White Sands. Note that the tower anemometer at the 137m level had uncertain measurements in the north south sensor (see text, page 74).

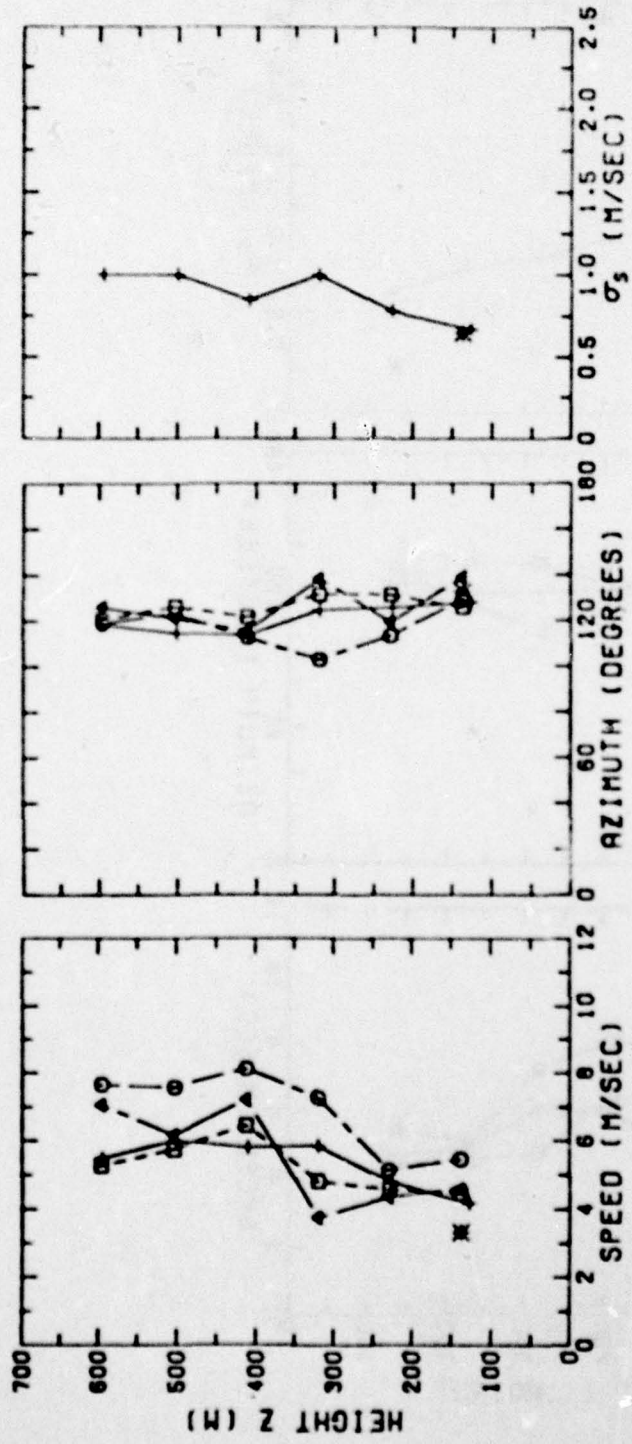


Figure 23. Similar plot to Figure 21 of lidar data obtained from 1645-1650 MST. Pilot balloons are at 1645-1637 (\square), 1645-1647 (\circ), and 1655-1657 (Δ) for January 19, 1978 data at White Sands.

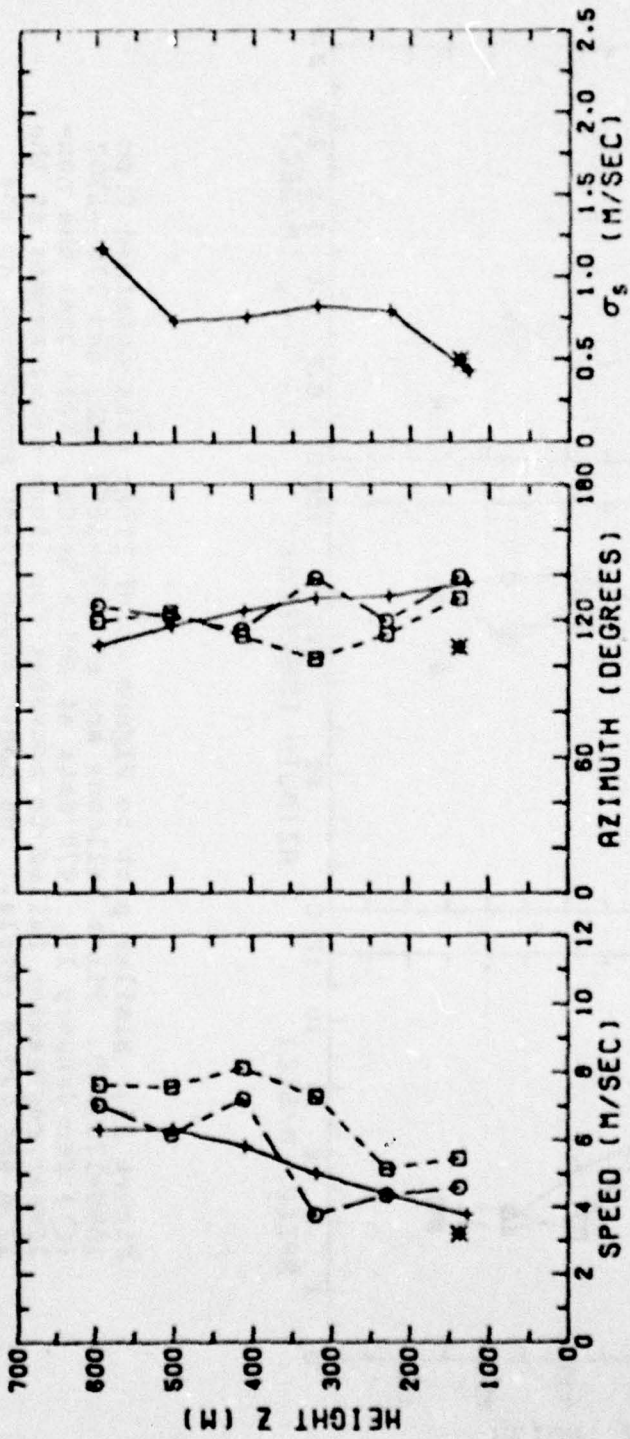


Figure 24: Similar plot to Figure 21 of lidar data obtained from 1652-1657MST. Pilot balloons are at 1645-1647 (\square) and 1655-1657 (\circ) for January 19, 1978 data at White Sands.

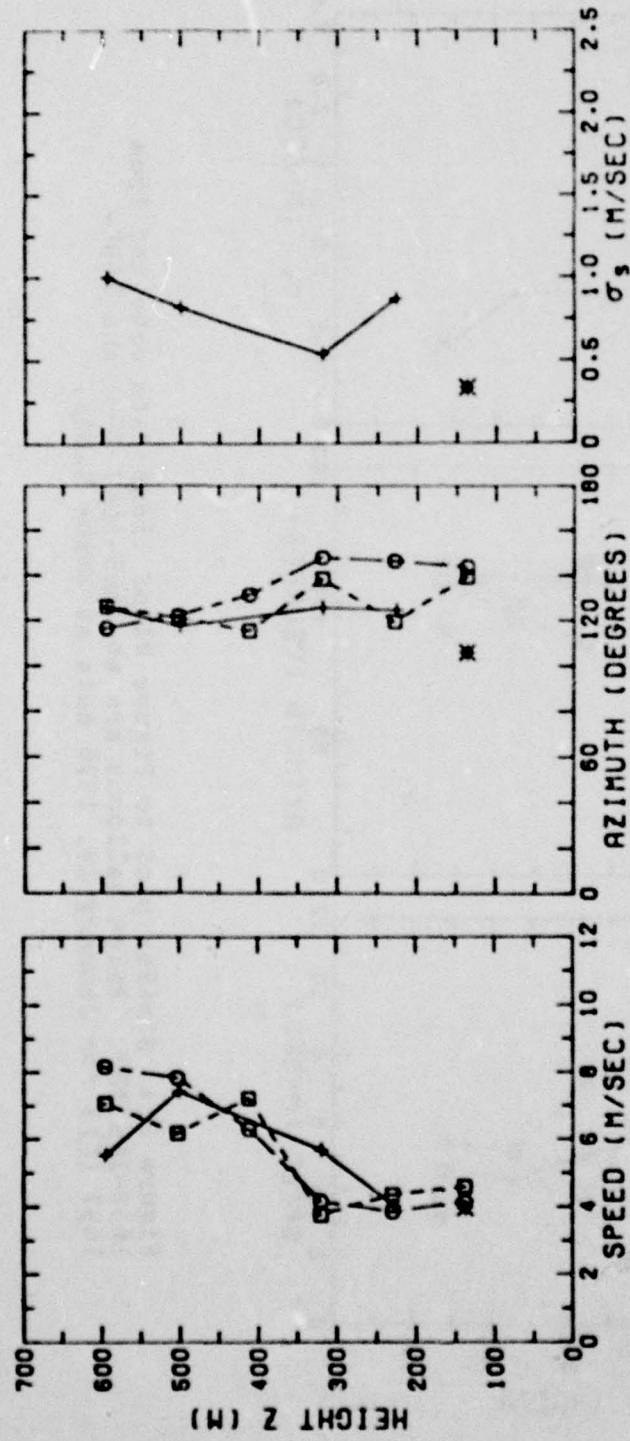


Figure 25: Similar plot to Figure 21 of lidar data obtained from 1658-1703MST. Pilot balloons are at 1655-1657 (\square) and 1705-1707 (\circ) for January 19, 1978 data at White Sands. Note that the non-linear regression failed to converge for lidar measurements at the 127m and 410 m levels. The north south tower anemometer at the 137m level was not consistent with lidar, pitot and cup anemometer measurements. Detailed discussion of this problem is given on page 74.

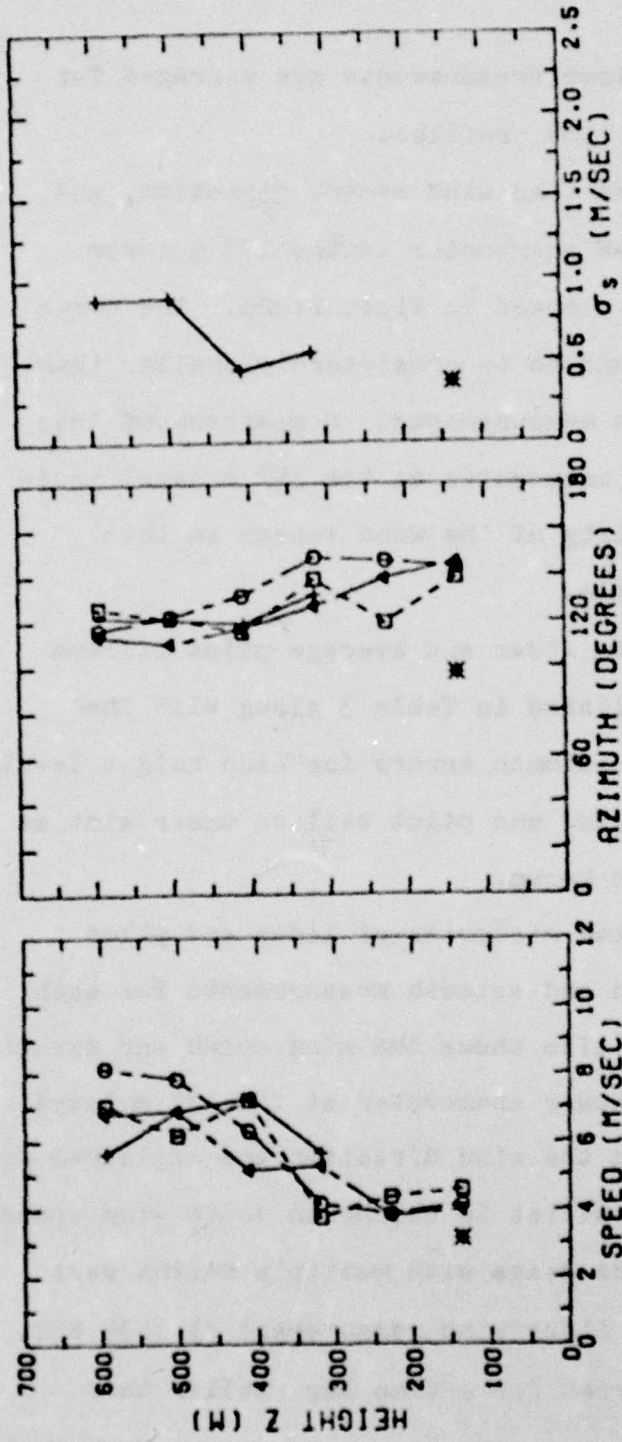


Figure 26: Similar plot to Figure 21 of lidar data obtained from 1704-1709MST. Pilot balloons are at 1655-1657 (\square), 1705-1707 (\bigcirc) and 1715-1717 (Δ) for January 19, 1978 data at White Sands. Note that the non-linear regression failed to converge for lidar measurements at the 127m and 227m levels. The north-south component of the U-V-W anemometer at the 137m level continued to have the same problem described on page 74.

applicable. These balloon measurements are averaged for comparisons with lidar wind profiles.

Measurements of the mean wind speed, direction, and rms speed from the U-V-W anemometer at the 137 m tower level at LC36 are also plotted in Figs. 21-26. The north south component was found to be consistently smaller than lidar and pilot balloon measurements. Comparison of this component with the cup anemometer at the 152 m level indicates that the reliability of the wind sensor in this direction is questionable.

Differences between lidar and average pilot balloon wind measurements are listed in Table 3 along with the mean and rms speed and azimuth errors for each height level. Average lidar quantization and pilot balloon uncertainties for each level are also known.

Figs. 27-32 are time histories of lidar and pilot balloon mean wind speed and azimuth measurements for each height level. Fig. 27 also shows the wind speed and direction measured by the U-V-W tower anemometer at the 137 m level. The large variations in the wind direction are explained by the instrumental difficulties in the north south wind speed sensor. Broad coherence peaks with multiple maxima were observed for the 594 m lidar wind measurement at 1635 MST. The maximum value occurred for a time lag smaller than

Table 3 Differences and Uncertainties for White Sands Data

z (m)	\bar{v}_l (m/s)	\bar{v}_{RDS} (m/s)	δv_L (m/s)	δv_q (m/s)	δv_p (m/s)	$\bar{\delta}v_l$ (m/s)	$\bar{\delta}v_q$ (m/s)	$\bar{\delta}v_p$ (m/s)	$\delta \delta v_L$ (%)	$\delta \delta v_q$ (%)	$\delta \delta v_p$ (%)
1270	-1.8	0.4	0.7	1.5	-0.9	-1.1	3.1	9.4	17.4	10.1	
2270	-1.1	0.3	0.6	0.6	-0.9	3.9	8.1	9.9	8.8	11.0	
3200	0.3	1.9	1.0	0	1.0	2.0	12.	9.9	6.3	10.6	
410	-1.8	1.5	0.9	0	1.0	-0.3	7.5	5.6	8.1		
501	-1.6	0.7	0.6	-0.6	1.1	-3.4	4.3	6.2	4.4	6.0	
594	-1.7	2.1	1.3	0	1.7	-1.0	6.7	7.9	3.7	9.5	

• Level with only 4 measurements

• Level with only 5 measurements

 δv_L and $\delta \delta v_L$ are lidar uncertainties δv_p and $\delta \delta v_p$ are pilot balloon uncertainties δv_q and $\delta \delta v_q$ are lidar quantization uncertainties

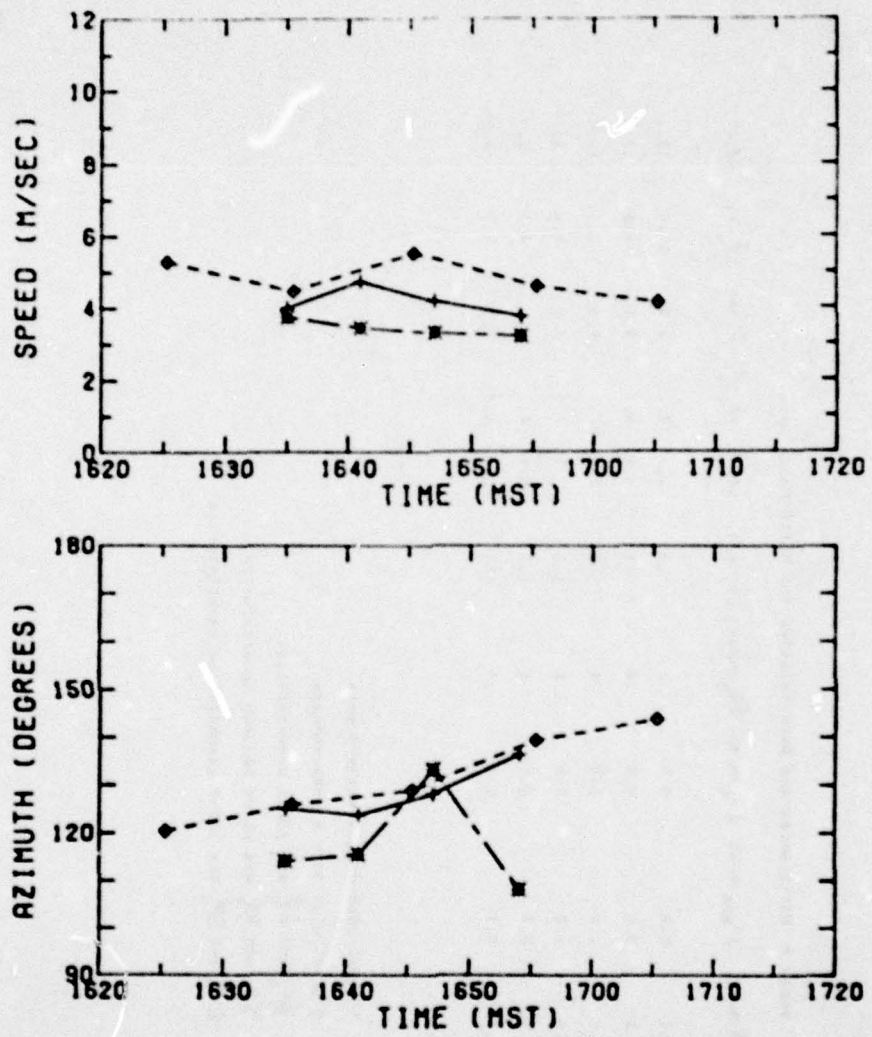


Figure 27: Time history of lidar (+), and pilot balloon (\diamond) measurements at the 127m level for data obtained on January 19, 1978 at White Sands Missile Range. Tower anemometer measurements (*) at the 137m level are also shown. The large variation in the tower azimuth is caused by discrepancies in the north south component, see page 74.

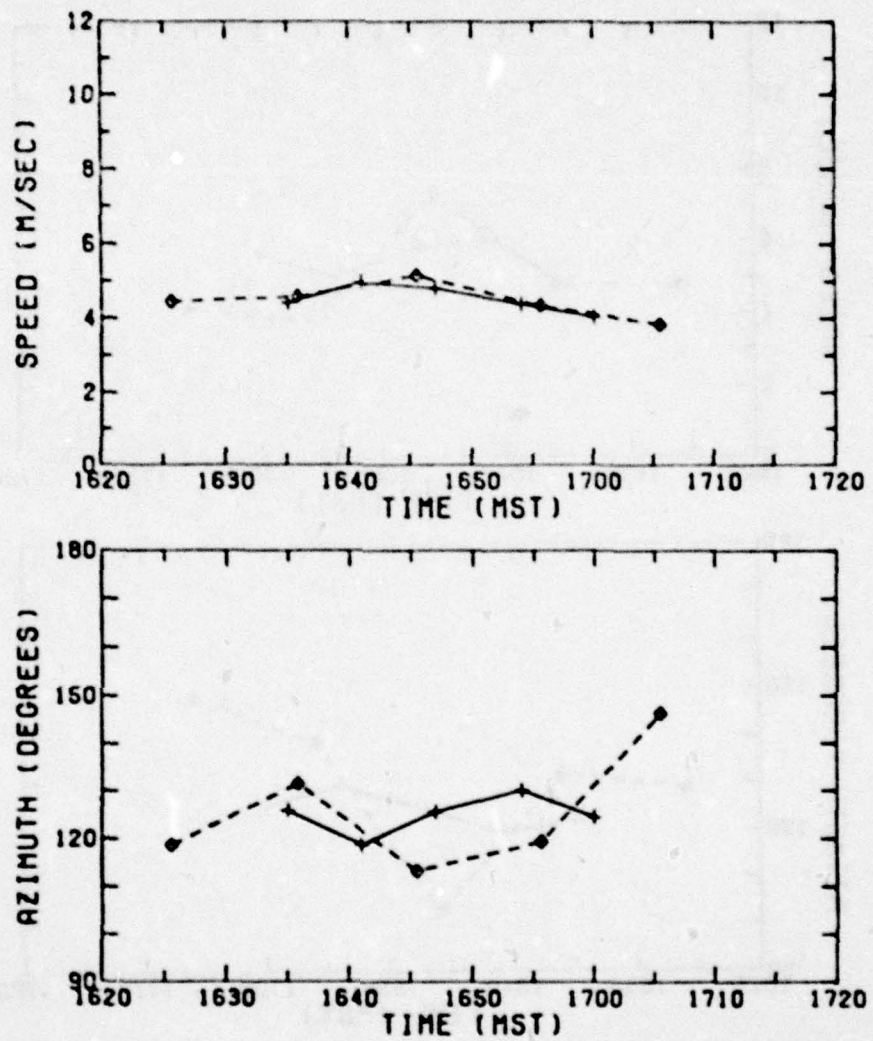


Figure 28: Similar graph of Figure 27 for the 227m level.

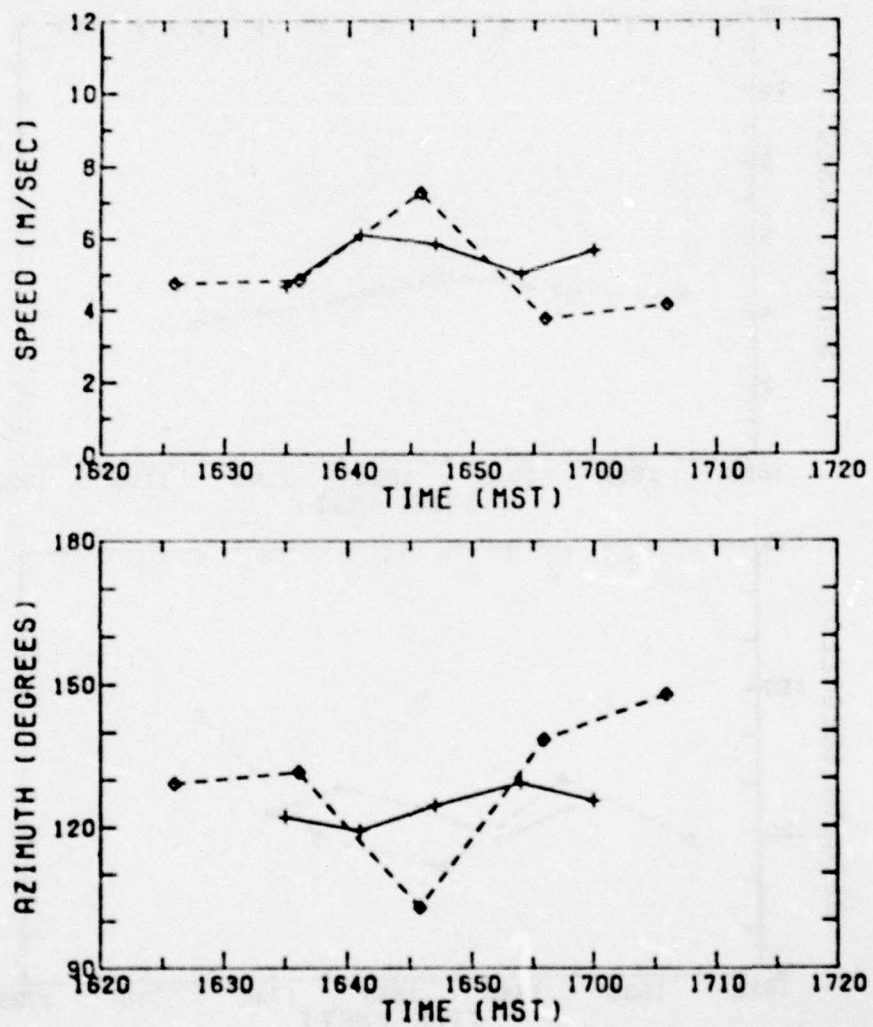


Figure 29: Similar graph for the 320m level.

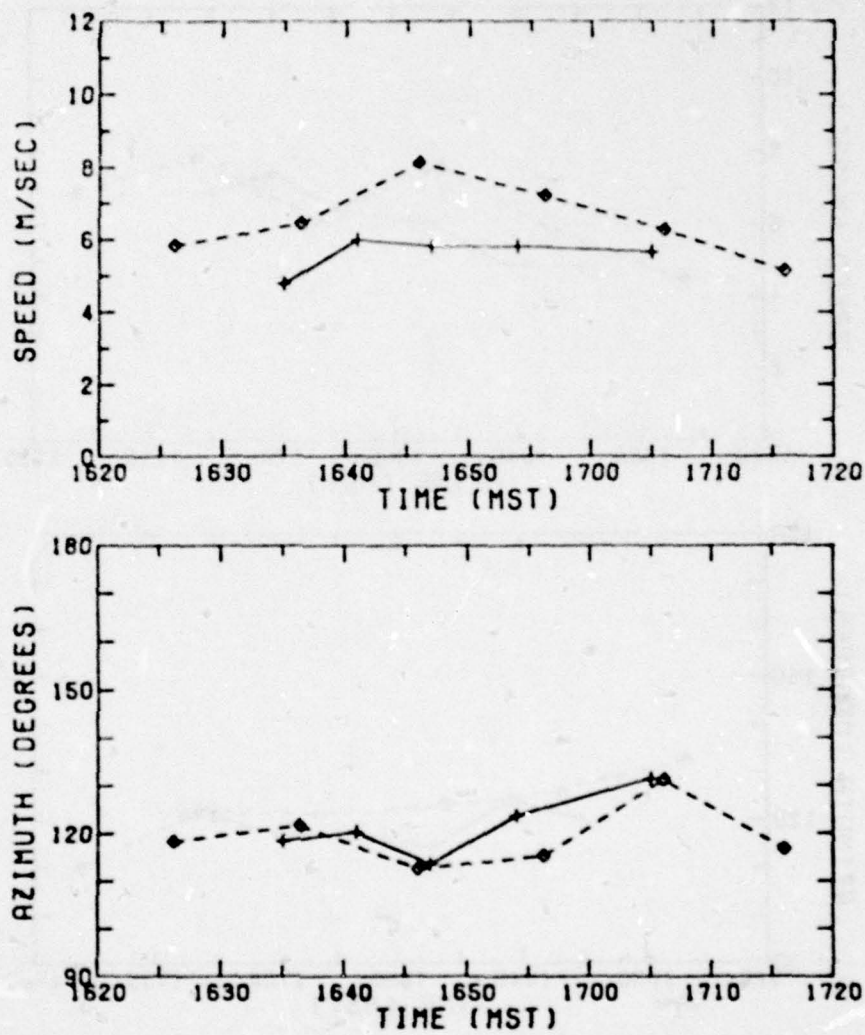


Figure 30: Same as Figure 29 for the 410m level.

AD-A078 678

WISCONSIN UNIV-MADISON
REMOTE MEASUREMENTS OF BOUNDARY LAYER VELOCITY PARAMETERS BY MO--ETC(U)
OCT 79 J T SROGA

DAAG29-76-C-0136

F/G 17/8

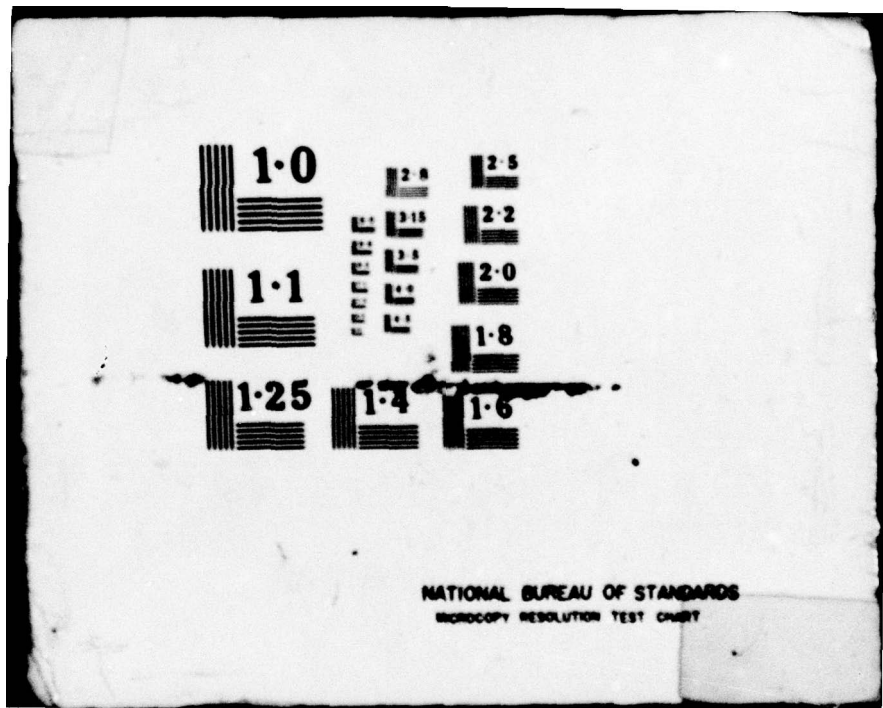
ERADCOM/ASL-CR-79-0136-1 NL

UNCLASSIFIED

2 OF 2
AD-A078678



END
DATE
FILMED
I - 80
DOC



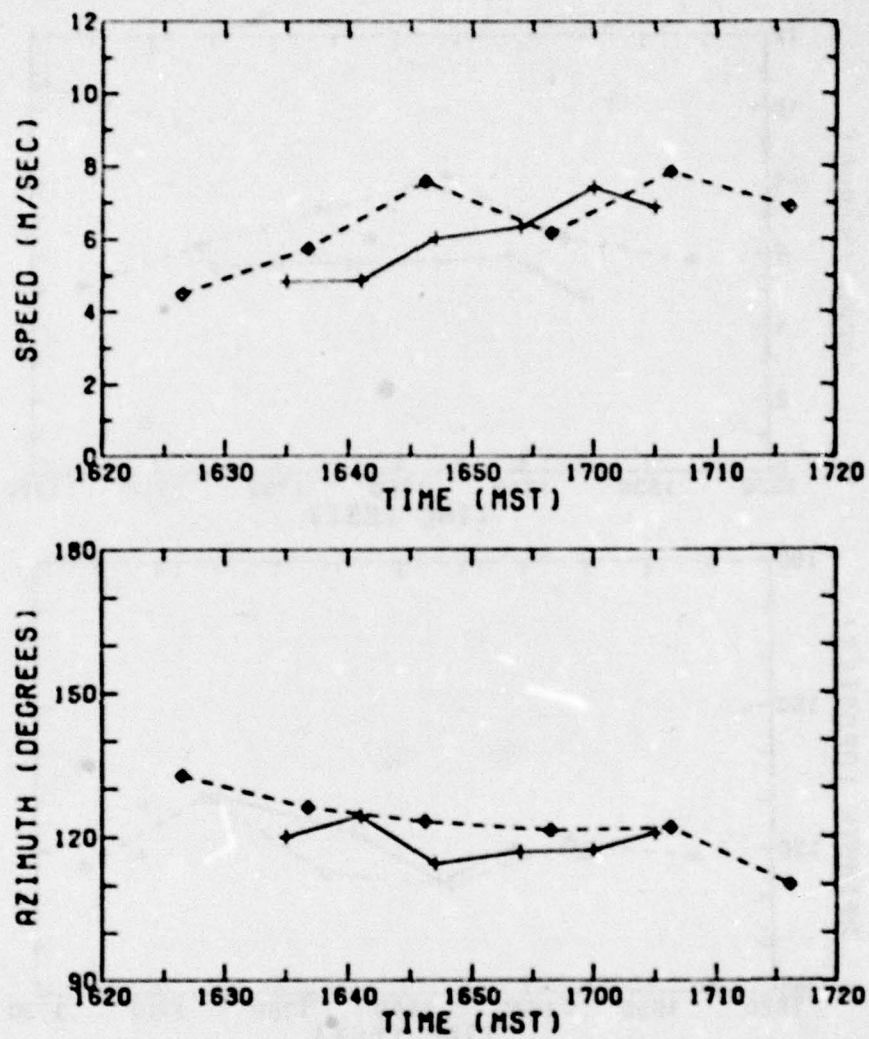


Figure 31: Same for the 501m level.

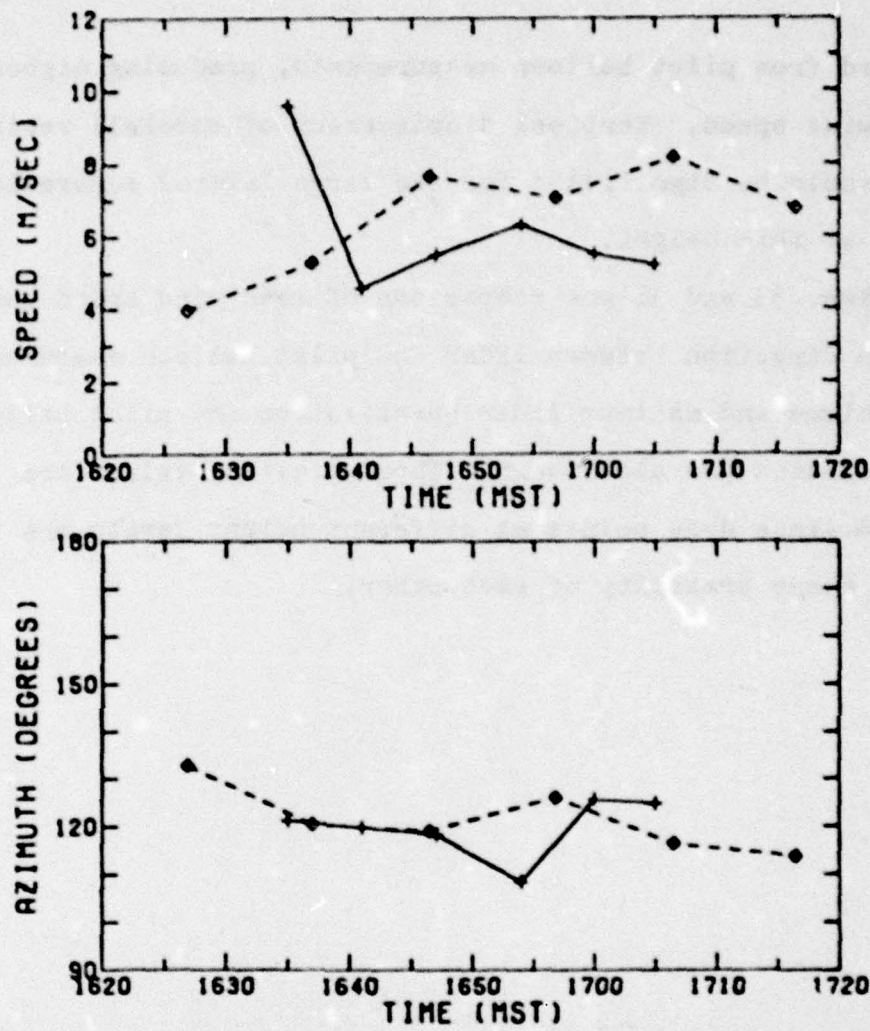


Figure 32: Similar graph of Figure 27 for the 594μm level. The first data point exhibited broad coherence peaks with multiple maxima. High wind speed corresponded to a shorter time lag than expected, see page 74.

expected from pilot balloon measurements, producing higher lidar wind speed. Vertical displacement of snowfall variations could be significant for the large lateral separation (99 m) at this height.

Figs. 33 and 34 are comparison of mean wind speed and azimuth direction between lidar and pilot balloon measurements. The minimum and maximum lidar quantization and pilot balloon uncertainties are also shown. These limiting values are graphed since data points at different height levels are within close proximity of each other.

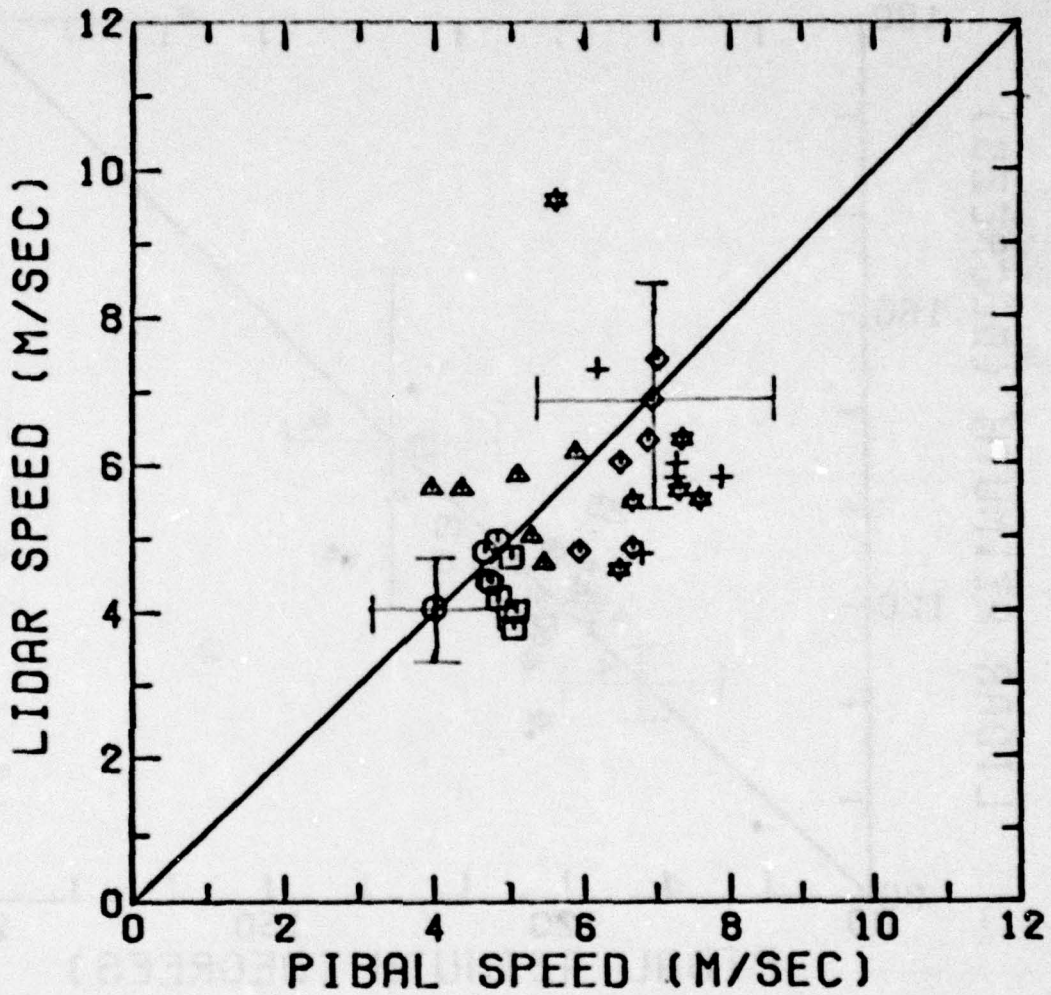


Figure 33: Comparisons of lidar and average pilot balloons speed (m/s) for each height level computed (\square -127m, \circ -227m, \triangle -320m, $+$ -410m, \diamond 501m, \ast 594m). These results are from data obtained on January 19, 1978 at White Sands Missile Range. Minimum and maximum lidar quantization and pilot balloon uncertainties from Table 3 are plotted since measurements are in close proximity with each other.

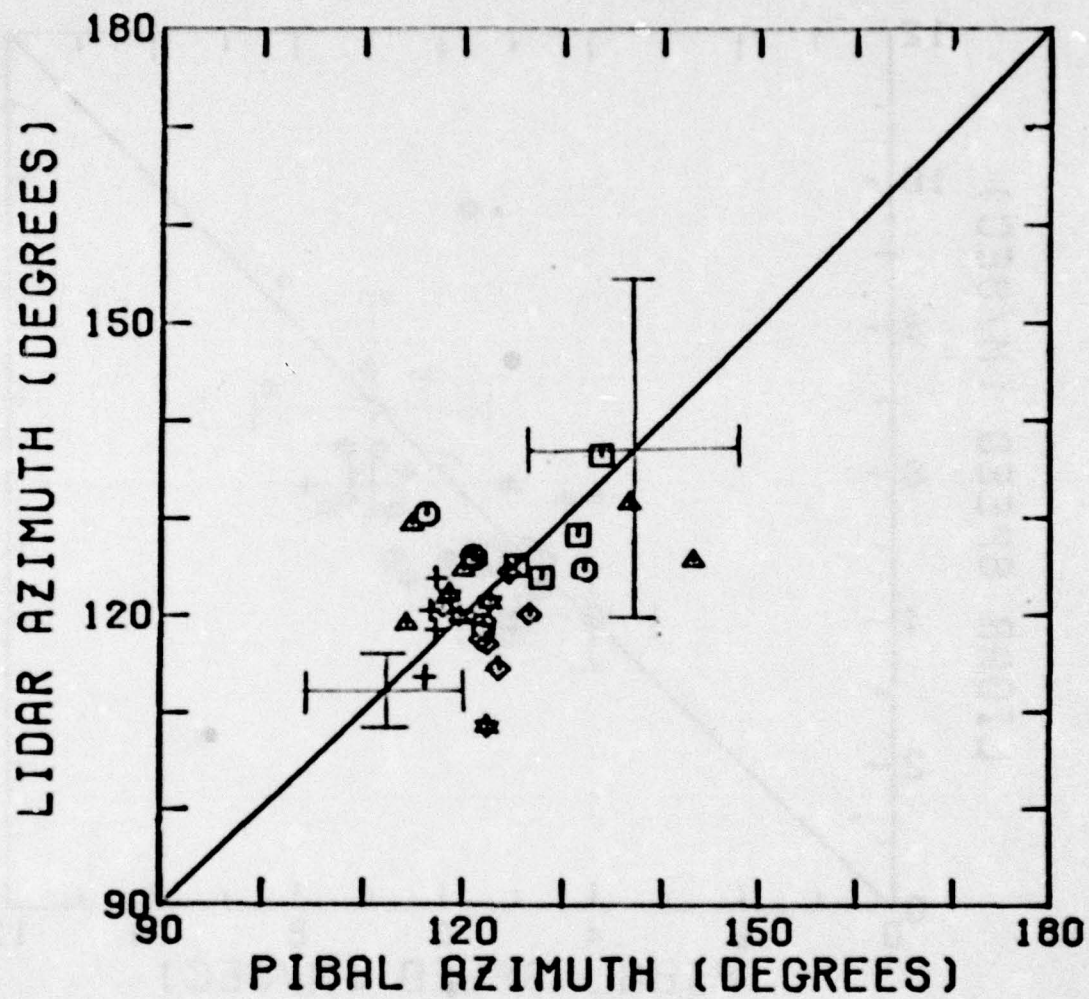


Figure 34: Similar plot to Figure 32 for the azimuth directions of all levels (same symbols) for January 19 data. Minimum and maximum uncertainties from Table 3 are also shown.

5.0 Conclusions

A procedure has been developed for remote measurements of the wind velocity. The motion of naturally occurring aerosol density inhomogeneities are measured by lidar to obtain average wind speed, direction and rms speed estimates. The Fast Fourier Transform (FFT) has been implemented in this procedure to increase computational efficiency.

An improvement in spatial filtering of lidar data has also been developed. The ratio of the signal to noise spectral characteristics are used to design an optimal linear filter based upon the lidar measurements themselves. Spectral components where the background noise is large compared to the aerosol inhomogeneity signal are suppressed one to two orders of magnitude with respect to those with large signal components (see Fig. 5). Aerosol inhomogeneity scale sizes seen from this figure range from 60 m to 1 km. These scale sizes carry wind information detectable with the present system. The ratio of the signal spectrum to the noise spectrum (Fig. 4) show high variability between successive spectral components for values smaller than approximately 0.5. Lidar aerosol inhomogeneity profiles with SNR less than 0.5 are therefore dominated by the background noise of the present system. Wind information in these instances are not recoverable.

Estimation of the mean wind velocity in the turbulent

planetary boundary layer has been improved by including a correction for the spatial and temporal coherence decay. Results from lidar wind measurements follow the temporal and spatial characteristics of the boundary layer flow. Comparisons of lidar wind measurements with independent wind measurements shown in Figs. 18, 19, 33, and 34 are generally within the estimated experimental uncertainties.

A measure of the turbulent dispersal of the aerosol inhomogeneities can be estimated from the coherence decay with increasing spatial and temporal separation. The model described in Section 2.3 is used to estimate the turbulent rms wind speed which cause the aerosol inhomogeneities to change in time. Kunkel (1978) has used similar measurements to estimate the turbulent energy dissipation rate for all scales.

Lidar rms wind speed measurements are shown in Fig. 20 to be consistent with concurrent tower anemometer estimates.

A measure of the reliability of lidar wind measurements can be obtained from the ratio of the measured error between lidar and independent measurements to the uncertainty in these measurements. This is expressed by the following formulas.

$$\epsilon_v = 14v_1/SV_{rms}$$

5.1

$$\epsilon_p = 14\phi_1/S\phi_{rms}$$

5.2

where ΔV is the wind speed difference between the lidar and independent wind measurements defined in Eq. 4.1.2.

$\Delta\phi$ is the azimuth direction difference between lidar and independent wind measurements defined in Eq. 4.1.3.

$S_{\Delta_{rms}} = (\Delta V_g^2 + \Delta \phi_{rf}^2)^{1/2}$ is the rms value of the lidar and independent wind direction uncertainties.

$S_{\Delta V_{rms}} = (\Delta V_g^2 + \Delta V_{rf}^2)^{1/2}$ is the rms value of the lidar and independent wind speed uncertainties.

ϵ_v is the ratio of the magnitude of the speed difference to the rms speed uncertainties.

ϵ_ϕ is the ratio of the magnitude of the azimuth difference to the rms azimuth uncertainties.

Graphs of these ratios (ϵ_v , ϵ_ϕ) are shown in Fig. 35 as a function of the SNR estimate (Eq. 2.2.5). The average values of ϵ_v and ϵ_ϕ along with the standard deviations are shown in the intervals $SNR \leq 1.5$, $1.5 < SNR \leq 2.5$, $SNR > 2.5$.

Values larger than one standard deviation from the mean represent a statistical probability (33%) that the error is larger than the uncertainty. This figure shows the average value of ϵ_v and ϵ_ϕ as well as the probability for larger errors than the uncertainties decreases with increasing SNR values.

Large discrepancies of some data points can be explained by the limitations of the method and equipment. The circled

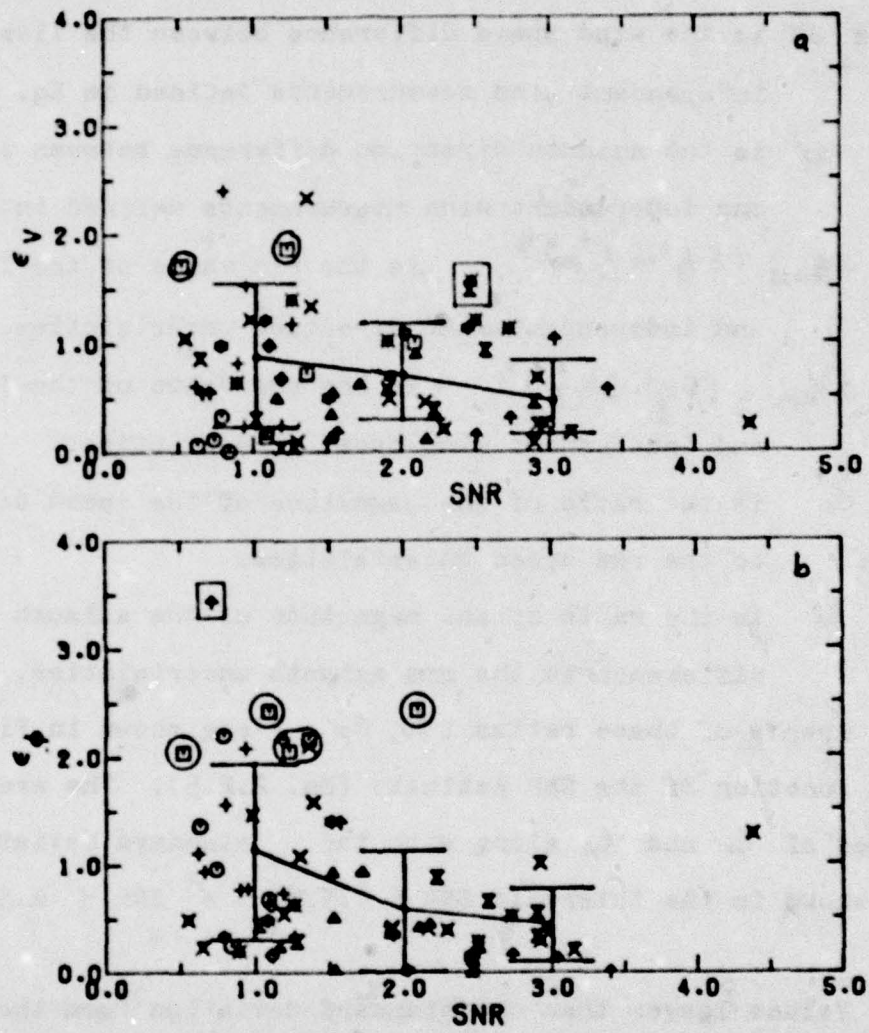


Figure 35: Graphs of ϵ_v , ϵ_d (see Eqs. 5.1 and 5.2) which are functions of the SNR (Eq. 2.2.5) calculated from Madison and White Sands data. Experimental days are April 22 (\circ), May 23 (\diamond), June 20 (Δ), June 23 (+), June 27 (\times) and July 26 (\square), 1977. White Sands data points are plotted for the height levels 127m (\dagger), 227m ($\overline{\times}$), 320m (\times), 410m (*), 501m (\overline{x}) and 594m (\ddagger). Circled and boxed data points are described in the text on page 97.

data points in Fig. 35b represent measurements where the radial wind speeds are small ($< 1\text{m/s}$). Large azimuth differences between lidar and tower measurements are due to larger lidar radial velocity estimates (see discussion on page 61). The boxed data points in Fig. 35b represent a segment where the nonlinear regression failed to converge due to low SNR values. The circled data points in Fig. 35a are measurements with low wind speeds ($2\text{-}3\text{m/s}$) and small speed differences ($< 0.5\text{m/s}$). These data points have small speed uncertainties ($\delta V_{\text{avg}} \leq 0.2\text{m/s}$) which cause large values of ϵ_r . The boxed data points in Fig. 35a exhibited very broad coherence peaks due to large lateral separation and significant changes in the light snow inhomogeneities during vertical displacements. Some discrepancies must be expected in these comparisons since lidar measurements are averaged differently than conventional wind measurements.

Measurement of wind velocity parameters shown in this thesis prove that lidar can become a useful tool in remote studies of the boundary layer. The reliability in lidar wind measurements can be increased by improvements in lidar instrumentation to decrease the noise contributions in lidar returns and would allow wind measurements to be obtained under a greater variety of atmospheric conditions.

Appendix A Calculation of Spectra and Coherence

A.1 Calculation of Spectra and Cross Spectra by the Fast Fourier Transform

The Fast Fourier Transform (FFT) is used to estimate the power and cross spectral densities of discrete, finite length series (Bingham et al., 1967; Cooley, et al., 1970; and Otness and Enochson, 1972). The FFT has the advantage over previous methods of spectral estimation in computational speed, especially for data segment lengths that are integer powers of two.

The finite size of the data segment introduces the problem of leakage in spectral estimates. Leakage is the effect that frequencies or wavenumbers outside a particular interval have on the spectral estimate over that interval. Leakage is reduced by application of a data window on the segment. Two common data windows are the Hann window and the cosine taper (Otness and Enochson, 1972). Both windows decrease the side lobe characteristics of the bandpass. The cosine taper window is used in this study in order to balance the problems of statistical stability and leakage of the spectral estimates.

The cosine taper window consists of tapering ten percent of the data segment length on each end with a cosine bell given by the formula (Bingham, et al., 1967),

$$D(x) = \begin{cases} \cos^2(5\pi x/L) & -L/2 \leq x < -4L/10 \\ 1 & -4L/10 \leq x \leq 4L/10 \\ \cos^2(5\pi x/L) & 4L/10 < x \leq L/2 \end{cases} \quad A.1.1$$

for a data segment extending from $-L/2$ to $L/2$.

The data window is applied on a spatial series, $f(x)$, in the following manner.

$$\hat{f}(x) = f(x) \cdot D(x) \quad A.1.2$$

$\hat{f}(x)$ is the modified spatial series.

The raw spectral estimates of the modified series \hat{f}_1 , \hat{f}_2 are calculated from the FFT of each series $\mathcal{F}_{\hat{f}_1}, \mathcal{F}_{\hat{f}_2}$, respectively.

$$\begin{aligned} S_1(k) &= \mathcal{F}_{\hat{f}_1}^*(k) \cdot \mathcal{F}_{\hat{f}_1}(k) \\ S_2(k) &= \mathcal{F}_{\hat{f}_2}^*(k) \cdot \mathcal{F}_{\hat{f}_2}(k) \\ S_{12}(k) &= \mathcal{F}_{\hat{f}_1}^*(k) \cdot \mathcal{F}_{\hat{f}_2}(k) \end{aligned} \quad A.1.3$$

Where the Fast Fourier Transform is defined as

$$\mathcal{F}_f(k) = \frac{2\delta}{N} \sum_{i=1}^N \hat{f}(x_i) e^{-j2\pi k x_i}$$

δ is the incremental separation of N data points ($L=N\delta$) and * denotes complex conjugation. S_1, S_2, S_{12} are the respective power and cross spectral estimates. The raw spectral estimates must be smoothed in order to decrease the

mean square error and increase the statistical significance of the spectral estimates. Smoothing can be accomplished by a weighted average over adjacent wavenumbers, (Cooley, et al., 1970), or by time averaging over a number of modified segments (Welsh, 1967). Time averaging was chosen for this study because of the small lengths of the data segments. The smoothed spectral estimates averaged over J time segments are

$$\begin{aligned}\tilde{s}_1(k) &= \frac{1}{J} \sum_{i=1}^J s_{1i}(k) \\ \tilde{s}_2(k) &= \frac{1}{J} \sum_{i=1}^J s_{2i}(k) \\ \tilde{s}_{12}(k) &= \frac{1}{J} \sum_{i=1}^J s_{12i}(k)\end{aligned}\quad \text{A.1.4}$$

Application of a data window decreases the variance because unequal weighting is given to various parts of the segment. The normalization factor (d) due to data window application is (Otness and Enochson, 1972)

$$d^{-1} = \frac{1}{L} \int_{-\gamma_2}^{\gamma_2} D^2(x) \cdot dx \quad \text{A.1.5}$$

Spectral values are scaled to maintain the true variance estimate.

$$\begin{aligned}\tilde{s}_1(k) &= d \cdot \tilde{s}'_1(k) \\ \tilde{s}_2(k) &= d \cdot \tilde{s}'_2(k) \\ \tilde{s}_{12}(k) &= d \cdot \tilde{s}'_{12}(k)\end{aligned}\quad \text{A.1.6}$$

For the cosine taper window, d has the value of 1/0.875.

A.2 Calculation of the Coherence

The coherence between two time or spatial series describe their relationship at various frequencies or wave-numbers. Calculation of the coherence between two series (subscripted 1, 2) is (Otness and Enochson, 1972)

$$\text{Coh}(k) = \frac{\tilde{S}_{12}^*(k) \cdot \tilde{S}_{12}(k)}{\tilde{S}_1(k) \cdot \tilde{S}_2(k)} \quad \text{A.2.1}$$

where $\tilde{S}_1(k)$, $\tilde{S}_2(k)$ are the smoothed spectral estimates and $\tilde{S}_{12}(k)$ is the smoothed cross spectral estimate. The asterisk (*) is complex conjugation. The calculation of smoothed spectral estimates are described in Appendix A.1. Smoothing of the spectral estimates increases the degrees of freedom, therefore decreasing the statistical uncertainty in spectral estimates and coherence measurements. The value of the coherence (Γ), for which there is a probability (P) of a coherence between random series exceeding this value is (Panofsky and Brier, 1968)

$$\Gamma = (1 - P^{1/(edf-2)})^{\frac{1}{2}} \quad \text{A.2.2}$$

where edf is the equivalent number of degrees of freedom. For a chi-square distribution, this number is twice the number of averaging segments. In this study, the edf is 198 for coherences calculated between azimuth angle ϕ and ϕ_a (see Fig. 2) and in filter estimations (99 segments averaged

over). The five percent probability value of \bar{P} is .12. Because coherence values calculated between ϕ_1 and ϕ_3 (see Fig. 2) are averaged over a small number of segments (50), the five percent probability value of \bar{P} is .17.

Appendix B Calculation of Signal Spectrum to Noise Spectrum Ratio, Signal to Noise Ratio (SNR) and Optimal Linear Filter.

An estimation of the ratio of the signal spectrum to the noise spectrum can be obtained from the coherence between different spatial series separated in time. The spectra of the series are functions of wavenumber and time lag only. The smoothed spectral estimate composed of signal and noise is (Wainstein and Zubokov, 1962)

$$\tilde{S}(k, \Delta t) = \tilde{S}_s(k, \Delta t) + \tilde{S}_n(k, \Delta t) + \tilde{S}_{sn}(k, \Delta t) \quad B1$$

where $\tilde{S}(k, \Delta t)$ is the smoothed spectral estimate of the spatial series, $\tilde{S}_s(k, \Delta t)$ is the signal spectrum, $\tilde{S}_n(k, \Delta t)$ is the noise spectrum, and $\tilde{S}_{sn}(k, \Delta t)$ is the "interference" spectrum of the signal and noise. The interference term is zero for no correlation between the signal and noise. Normal, random noise is not correlated between spatial series at different times. The smoothed cross spectrum between different, spatial series is the cross spectrum of the signal for normal, random noise, i.e.,

$$\tilde{S}_{12}(k, \Delta t) = \tilde{S}_{s12}(k, \Delta t) \quad B2$$

The coherence between the two series as defined in

Appendix A.2 is

$$\text{Coh}(k, \Delta t) = \frac{\tilde{S}_{s12}^*(k, \Delta t) \cdot \tilde{S}_{s12}(k, \Delta t)}{\tilde{S}_1(k, 0) \cdot \tilde{S}_2(k, \Delta t)} \quad B3$$

where * denotes complex conjugation and the subscripts 1, 2 refer to the two separate series. In the limit as the time lag (Δt) approaches zero, the cross spectral estimates limiting value is the signal spectrum. The individual spectra of each series approach the smoothed spectral estimate for zero time lag,

$$\begin{aligned} \lim_{\Delta t \rightarrow 0} \tilde{S}_{s12}(k, \Delta t) &= \tilde{S}_{s1}(k, 0) \\ \lim_{\Delta t \rightarrow 0} \tilde{S}_2(k, \Delta t) &= \tilde{S}_1(k, 0) \end{aligned} \quad B4$$

The limit of the coherence as Δt approaches zero is therefore:

$$\begin{aligned} \lim_{\Delta t \rightarrow 0} \text{Coh}(k, \Delta t) &= \frac{\tilde{S}_{s1}^*(k, 0) \cdot \tilde{S}_{s1}(k, 0)}{\tilde{S}_1(k, 0) \cdot \tilde{S}_1(k, 0)} \\ &= \left[\frac{\tilde{S}_{s1}(k, 0)}{\tilde{S}_{s1}(k, 0) + \tilde{S}_{n1}(k, 0)} \right]^2 \end{aligned} \quad B5$$

Solving for the ratio of the signal spectrum to the noise spectrum yields

$$\frac{S_{sl}(k,0)}{S_{nl}(k,0)} = \left[\lim_{\Delta t \rightarrow 0} \text{Coh}(k, \Delta t) \right]^{-\frac{1}{2}} - 1 \quad B6$$

Filtering a series suppresses the noise component in order to reproduce the signal with the least amount of error. The filtered series is the convolution of a linear filter (h) with the original series (f):

$$\tilde{f}(x) = \int_{-\infty}^{\infty} h(x-x') \cdot f(x') \cdot dx' \quad B7$$

The optimal linear filter that minimizes the quantity

$$\overline{\epsilon^2} = \overline{[\tilde{f}(x)-f(x)]^2} \quad (\text{overbar denotes ensemble averages})$$

is calculated from the knowledge of the ratio of the signal spectrum to the noise spectrum. The transfer function ($H(k)$) of the optimal linear filter is shown by Wainstein and Zubakov (1962) to be

$$H(k) = \frac{\tilde{S}_{sl}(k,0)}{\tilde{S}_{sl}(k,0) + \tilde{S}_{nl}(k,0)} \quad B7$$

where $H(k)$ is defined as the Fourier transform of the optimal linear filter

$$H(k) = \int_{-\infty}^{\infty} h(x') \cdot \exp(-i 2 \pi k x') \cdot dx' = \tilde{f}_h(k) \quad B8$$

The application of a filter changes the spectral estimates of the series. The Fourier transform of the

filtered series ($\tilde{f}_f(k)$) is the product of the transforms of the original series ($f_f(k)$) and the filter ($H(k)$).

$$\tilde{f}_f(k) = f_f(k) \cdot H(k)$$

The filtered spectrum $\hat{\tilde{S}}_{sl}(k,0)$ is the conjugate multiplication of the Fourier transform with itself.

$$\begin{aligned} \hat{\tilde{S}}_{sl}(k,0) &= [H(k) \cdot \tilde{f}_f(k)] * [H(k) \cdot \tilde{f}_f(k)] \\ &= (H(k))^2 \cdot \tilde{S}(k) \end{aligned}$$
B9

The variance of the series is the integral over all wavenumbers of the spectrum.

$$\tilde{\sigma}_s^2 = \int_0^\infty \tilde{S}(k) \cdot dk$$

The variance of the filtered series is therefore:

$$\hat{\tilde{\sigma}}_s^2 = \int_0^\infty \hat{\tilde{S}}(k) \cdot dk = \int_0^\infty (H(k))^2 \cdot \tilde{S}(k) \cdot dk$$

For white, gaussian noise, the noise spectrum is constant over the bandpass of the filter. The noise variance of the filtered series is given by:

$$\hat{\tilde{\sigma}}_{an}^2 = \int_0^\infty \hat{\tilde{S}}_n(k) \cdot dk = \tilde{S}_n \int_0^\infty (H(k))^2 \cdot dk$$

\tilde{S}_n being the constant value of the noise spectrum.

The weighted integration of the signal spectrum to noise spectrum ratio by the square of the transfer function

100

is the ratio of the filtered signal variance to the noise variance (SNR).

$$\text{SNR} = \int_0^{\infty} (H(k))^2 \cdot \frac{\tilde{S}_s(k)}{\tilde{S}_n(k)} \cdot dk$$
$$= \frac{\int_0^{\infty} (H(k))^2 \cdot [H(k)^{-1} - 1]^{-1} dk}{\int_0^{\infty} (H(k))^2 \cdot dk}$$

B10

Appendix C Derivation of an Analytical Form for Coherence
Decay

This analysis shows that the mean and rms wind speed can be recovered from the decay of coherence between lidar measurements of aerosol inhomogeneities separated in time and space. These measurements are assumed to extend to infinity in the presence of no attenuation in order to describe a simple analytical model for this decay. For the purpose of this analysis, the velocity distribution is assumed to be homogeneous and isotropic in both time and space. The aerosol inhomogeneities are assumed to be described as three dimensional Gaussian structures being advected by the wind.

The functional form of the inhomogeneities is

$$f(\vec{g}, \vec{g}, t) = \exp\left[-\sum_i^3 (g_i - g_{i0} - \dot{g}_i t)^2 / 2\sigma_i^2\right] \quad C1$$

where t refers to time and the positions are described in terms of generalized coordinates, q_i 's. The initial position of the centroid of the inhomogeneity in the i th direction is q_{i0} with a rms width of the structure, σ_i . The motion of the inhomogeneity are the generalized velocities in each direction, \dot{q}_i .

The lag-cross covariance function, C_{12} , between two

lidar profiles separated in space and time is used to infer motion. The geometry of the experiment is shown in Fig. C1 for covariance in the q_2 direction. One lidar profile has q_1, q_3 coordinates, Q_1, Q_3 . The second profile is separated from the first in time by Δt and in the q_1, q_3 directions by $\Delta q_1, \Delta q_3$. The lag-cross covariance averaged over all possible initial positions and time is

$$C_{12}(\bar{q}, \bar{g}, \Delta t) = \int_{-\infty}^{\infty} dt \int_{-\infty}^{\infty} dq_1 \int_{-\infty}^{\infty} dq_3 \int_{-\infty}^{\infty} dg_1 \int_{-\infty}^{\infty} dg_3 \exp \left\{ - \sum_{i=1}^3 [(g_i - g_{i0} - g_{i2})^2 / 2\sigma_i^2 + (g_i - g_{i0} - g_{i2} + \Delta g_i)^2 / 2\sigma_i^2] \right\} C_2$$

The variances (C_1, C_2) of the profile along each line are averaged in a similar manner.

$$C_1 = \int_{-\infty}^{\infty} dt \int_{-\infty}^{\infty} dq_1 \int_{-\infty}^{\infty} dq_3 \int_{-\infty}^{\infty} dg_1 \int_{-\infty}^{\infty} dg_3 \exp \left\{ - \sum_{i=1}^3 (g_i - g_{i0} - g_{i2})^2 / 2\sigma_i^2 \right\} C_{3a}$$

$$C_2 = \int_{-\infty}^{\infty} dt \int_{-\infty}^{\infty} dq_1 \int_{-\infty}^{\infty} dq_3 \int_{-\infty}^{\infty} dg_1 \int_{-\infty}^{\infty} dg_3 \exp \left\{ - \sum_{i=1}^3 (g_i + \Delta g_i - g_{i0} - g_{i2} + \Delta g_i)^2 / 2\sigma_i^2 \right\} C_{3b}$$

The integrals above can be reduced by substitution to the form

$$\int_{-\infty}^{\infty} e^{-ax^2 + bx} dx = \sqrt{\frac{\pi}{a}} e^{b^2/4a} C_4$$

since the integrals are Gaussian and products of Gaussians.

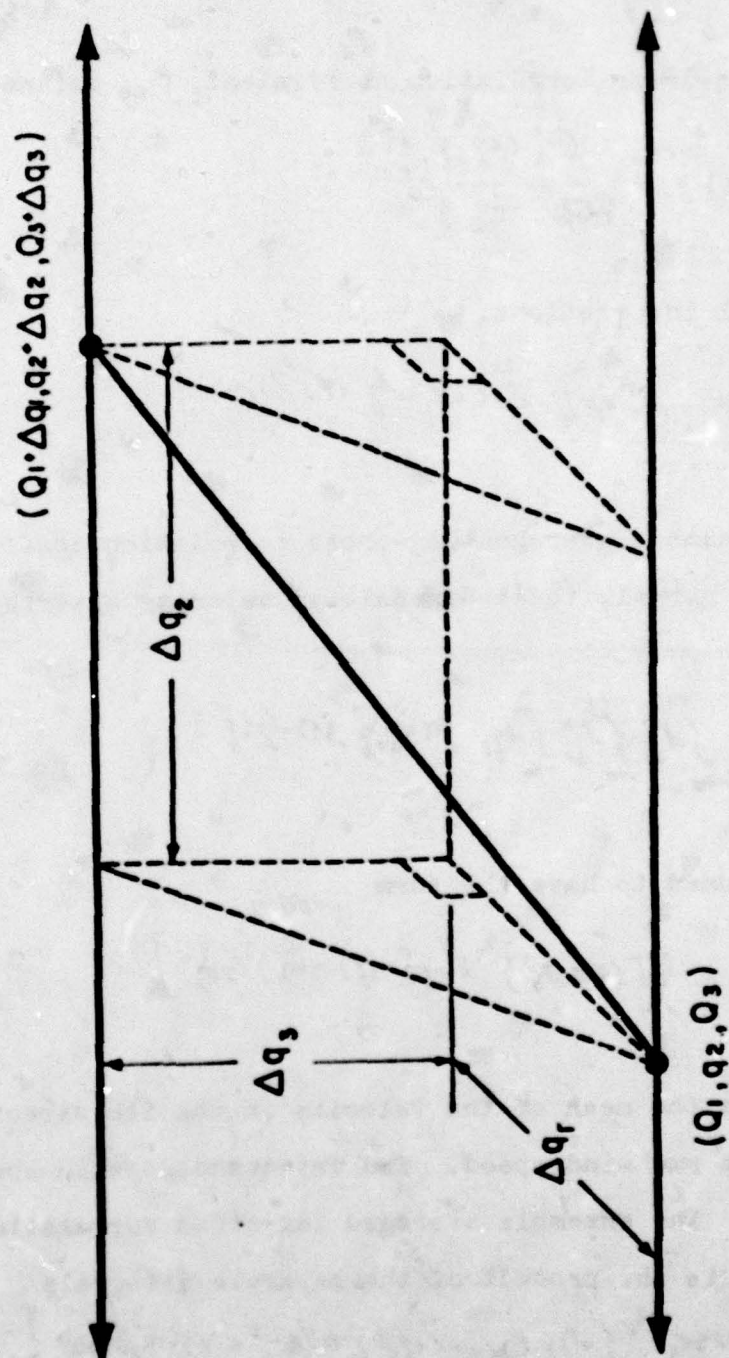


Figure C-11: Geometry of cross correlation in q_2 for two spatial series by q_1 , q_2 , q_3 . q_2 is the lag value in q_2 .

The lag-cross correlation coefficient, ρ , defined as

$$\rho(\vec{q}, \vec{g}, \Delta t) = \frac{C_{12}(\vec{q}\vec{g}, \Delta t)}{(C_1 \cdot C_2)^{1/2}} \quad (5a)$$

is after all integrations.

$$\rho(\vec{q}, \vec{g}, \Delta t) = \exp\left[-\sum_{i=1}^3 (\vec{q}_i - \vec{g}_i \Delta t)^2 / 4C_i^2\right] \quad (5b)$$

The ensemble averaged lag-cross correlation coefficient, $\hat{\rho}$, over a normal, three-dimensional velocity distribution, $G(\vec{q})$ is

$$\hat{\rho}(\vec{q}, \vec{u}, \Delta t) = \int_{-\infty}^{\infty} d\vec{q}_1 \int_{-\infty}^{\infty} d\vec{q}_2 \int_{-\infty}^{\infty} d\vec{q}_3 \rho(\vec{q}, \vec{q}, \Delta t) G(\vec{q}) \quad (6)$$

$G(\vec{q})$ is assumed to have the form

$$G(\vec{q}) = \frac{1}{(2\pi C_s)^3} \exp\left[-(\vec{q}_1 - \vec{u}_1)^2 / 2C_1^2\right] \quad (7)$$

where \vec{u}_i is the mean of the velocity in the i th direction and C_s is the rms wind speed. The integrands are independent in each \vec{q}_i . The ensemble averaged lag-cross correlation coefficient is the product of the separate integrals

$$\hat{\rho}_{\vec{q}, \vec{u}, \Delta t} = \frac{1}{(2\pi C_s)^3} \int d\vec{q}_1 \exp\left[-(\vec{q}_1 - \vec{u}_1)^2 / 2C_1^2 + (\vec{q}_1 - \vec{u}_1)^2 / 2C_1^2\right] \quad (8a)$$

C8a

The integral is reduced by substitution to the form of Eq. C4, resulting in

$$\hat{\rho}(q_1, \bar{u}, \bar{v}, t) = \frac{1}{\pi} \left[\frac{2\sigma_a^2}{2\sigma_e^2 + 2\sigma_s^2 \alpha^2} \right]^{1/2} \exp \left\{ - \frac{(4q_1 - \bar{u}_1 \alpha)^2}{(4\sigma_e^2 + 2\sigma_s^2 \alpha^2)} \right\} \quad \text{C8b}$$

This equation is similar to one used by Kunkel (1978).

To simplify the functional form, the aerosol inhomogeneities are assumed to be isotropic ($\sigma_e = \sigma_s = \sigma_a$) and measurements are made in the q_1, q_2 plane ($\Delta q_3 = 0$). The final form of the ensemble averaged, lag-cross correlation coefficient used in this analysis is

$$\hat{\rho}(q_1, q_2, \bar{u}, \bar{v}, t) = \left[\frac{2\sigma_a^2}{2\sigma_e^2 + 2\sigma_s^2 \alpha^2} \right]^{1/2} \cdot$$

$$\exp \left\{ - \frac{[(4q_1 - \bar{u})\alpha]^2 + [(4q_2 - \bar{v})\alpha]^2}{(4\sigma_a^2 + 2\sigma_s^2 \alpha^2)} \right\}$$

C9

where $\Delta q_1 = \Delta x$, $\Delta q_2 = \Delta y$, $\bar{u}_1 = \bar{u}$, $\bar{u}_2 = \bar{v}$, $\bar{u}_3 = 0$

The Fourier transform of the lag-cross correlation coefficient in Δy is the lag-cross spectrum, $\tilde{S}_{12}(k, \Delta x, u, v, \Delta t)$.

The integration over spatial lag, Δy , is

$$\int_{-\infty}^{\infty} \exp \left\{ - \frac{(4q_2 - \bar{v} \alpha)^2}{(4\sigma_a^2 + 2\sigma_s^2 \alpha^2)} - i 2\pi k q_2 \right\} dq_2$$

which can be reduced to the same form as Eq. C4. The resulting lag-cross spectrum is

$$\tilde{S}_{12}(k, \alpha, \bar{u}, \bar{v}, \alpha t) = \left[\frac{\omega \sigma_a^2}{(\omega \sigma_e^2 + \sigma_s^2 \alpha t^2)} \right]^{\frac{1}{2}} \cdot \left[\frac{\omega \sigma_a^2 + \sigma_s^2 \alpha t^2}{\omega \sigma_e^2 + \sigma_s^2 \alpha t^2} \right]^{\frac{1}{2}}$$

$$\times \sqrt{- (4x - \bar{u} \alpha t)^2 / (\omega \sigma_e^2 + \sigma_s^2 \alpha t^2) - 2 \bar{v}^2 k^2 (\omega \sigma_a^2 + \sigma_s^2 \alpha t^2) + 4 \bar{v}^2 k^2 \sigma_s^2 \alpha t^2}$$

C10

The coherence function, Coh , is proportional to the square of the absolute magnitude of the lag-cross spectrum;

$$Coh(k, \alpha, \bar{u}, \alpha t) \propto |S_{12}(k, \alpha, \bar{u}, \bar{v}, \alpha t)|^2$$

$$= \frac{(\omega \sigma_a^2)^2}{(\omega \sigma_e^2 + \sigma_s^2 \alpha t^2)^2} \cdot \sqrt{- (4x - \bar{u} \alpha t)^2 / (\omega \sigma_e^2 + \sigma_s^2 \alpha t^2) - 4 \bar{v}^2 k^2 (\omega \sigma_a^2 + \sigma_s^2 \alpha t^2)}$$

The value of the coherence for the quantity ($x - \bar{u} \alpha t = 0$) and $\sigma_s = 0$, is identically one. Therefore, the ratio

$$\frac{Coh(k, \alpha, \bar{u}, \alpha t)}{1} = \frac{\omega \sigma_a^2}{\omega \sigma_e^2 + \sigma_s^2 \alpha t^2} \cdot \sqrt{- (4x - \bar{u} \alpha t)^2 / (\omega \sigma_e^2 + \sigma_s^2 \alpha t^2) - 4 \bar{v}^2 k^2 \sigma_s^2 \alpha t^2}$$

C11

is the decay of the coherence with spatial and temporal separations due to velocity fluctuations. Note that for $\sigma_s = 0$, the coherence is Gaussian, as expected from the assumptions of the model.

Appendix D Error Analysis of Pilot Balloon and Tower
Anemometer Wind Measurements

D.1 Errors in Pilot Balloon Measurements Due to Position
Errors

Pilot balloon winds are derived from position changes of the balloon in small time intervals, therefore the errors in determining the position of the balloon are translated into speed errors. The geometry of the balloon's position in spherical coordinates is shown in Fig. D-1. For radar tracking of the balloon, the slant range, R , azimuth and elevation angles, θ, ϕ , are measured. The horizontal components of the pibal are, (Middleton and Spilhaus, 1953)

$$x = R \cos(\theta) \sin(\phi)$$

D1

$$y = R \cos(\theta) \cos(\phi)$$

The differential element of each component is

$$dx = \cos(\theta) \sin(\phi) dR - R (\sin(\theta) \sin(\phi)) d\theta - \cos(\theta) \cos(\phi) d\phi$$

$$dy = \cos(\theta) \cos(\phi) dR - R (\sin(\theta) \cos(\phi)) d\theta + \cos(\theta) \sin(\phi) d\phi$$

D2

The distance the balloon has traveled in a time δt for the x component is

$$(u + \delta u) \cdot \delta t = (x + \delta x)_{2} - (x + \delta x)_{1}$$

replacing exact differentials by the small variations,

The maximum velocity error in the x component is

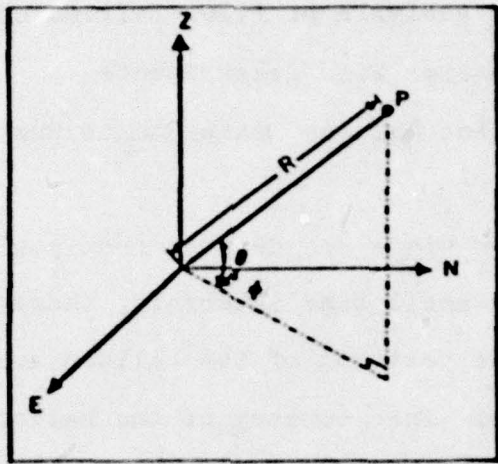


Fig. D-1 Geometry for determining the position of the pilot balloon in spherical coordinates.

$$\begin{aligned}
 \delta U_{max} &\leq (1\delta x_1 + 1\delta y_1)/\delta t \\
 &\leq \frac{\delta R}{\delta t} |\cos \theta_1 \sin \phi_1 + \cos \theta_1 \sin \phi_1| + \\
 &\quad \frac{\delta \theta}{\delta t} |R_2 \sin \theta_2 \sin \phi_2 + R_1 \sin \theta_1 \sin \phi_1| + \\
 &\quad \frac{\delta \phi}{\delta t} |R_2 \cos \theta_2 \cos \phi_2 + R_1 \cos \theta_1 \cos \phi_1|
 \end{aligned}
 \tag{D3}$$

The trigonometric values are in absolute value less than one. Therefore, the maximum error in the x component of velocity is

$$\delta U_{max} \leq 2 \frac{\delta R}{\delta t} + 2 \bar{R} \left(\frac{\delta \theta}{\delta t} + \frac{\delta \phi}{\delta t} \right)$$

where $\bar{R} = \frac{1}{2}(R_1 + R_2)$.

A similar expression can be derived for the y component of the velocity. The maximum error for the y component is

$$\delta V_{max} \leq 2 \frac{\delta R}{\delta t} + 2 \bar{R} \left(\frac{\delta \theta}{\delta t} + \frac{\delta \phi}{\delta t} \right)
 \tag{D4}$$

Estimation of the errors in terms of speed and azimuth can be obtained in the same manner as lidar error estimations.

D.2 Statistical Uncertainty of Tower Anemometer Measurements

Uncertainties in measurements of mean quantities by an anemometer depends on the number of independent measurements made. Measurements of this kind are time averaged at a single point. The Eulerian time scale, $\bar{\tau}_e$, measures the time period of statistically independent samples to drift past the anemometer. For stationary flows, the Eulerian time scale is defined as

$$\bar{\tau}_e = \int_0^{\infty} \rho(\tau) d\tau \quad D.2.1$$

where ρ is the auto correlation function and $d\tau$ is the time lag. The number of independent samples in a time period of length T is

$$N_T = T/\bar{\tau}_e \quad D.2.2$$

The uncertainty, $\bar{\sigma}$, in determining the mean value of a parent population with a standard deviation, σ , and N_0 independent measurements is (Bevington, 1969)

$$\bar{\sigma} = \sigma / \sqrt{N_0} \quad D.2.3$$

The uncertainty in measurements of mean quantities by an anemometer is

$$\bar{\sigma} = \sigma / \sqrt{N_T} = \sigma \sqrt{\bar{\tau}_e / T} \quad D.2.4$$

BIBLIOGRAPHY

- Angell, J.K., and A.B. Bernstein (1976): Evidence for a Reduction in Wind Speed on the Upwind Side of a Tower. JAM, 15, 186-188.
- Armstrong, R.L., J.B. Mason and T. Barber (1976): Detection of Atmospheric Aerosol Flow using a Transit Time Lidar Velocimeter. Appl. Opt., 15, 2891-2895.
- Benedetti-Michelangeli, G., F. Congeduti and G. Fiocco (1972): Measurements of Aerosol Motion and Wind Velocity in the Lower Troposphere by Doppler Optical Radar. JAS, 29, 906-910.
- Bevington, P.R. (1969): Data Reduction and Error Analysis for the Physical Sciences. McGraw-Hill, Inc., New York, 336 pp.
- Bingham, C., M.D. Godfrey and J.W. Tukey (1967): Modern Techniques of Power Spectrum Estimation. IEE Trans. on Audio and Electac. 15, 56-66.
- Blackman, R.B. and J.W. Tukey (1958): The Measurement of Power Spectra. Dover Publications, Inc., New York, 190 pp.
- Briggs, B.H. (1968a): On the Analysis of Moving Patterns in Geophysics-I. Correlation Analysis. J. of Atmos. and Terr. Physics. 30, 1777-1788.

- (1968b): On the Analysis of Moving Patterns in Geophysics-II. Dispersion Analysis. J. of Atmos. and Terr. Physics. 30, 1789-1794.
- Briggs, B.H., G.J. Phillips and D.H. Shinn (1950): The Analysis of Observations on Spaced Receivers of the Fading of Radio Signals. Proc. of the Phys. Soc. 62, 106-121.
- Collis, R.T. (1969): Lidar Advances in Geophysics. H.E. Landsberg, and J.S. Mieghem, Eds. Academic Press, New York, 13, 113-139.
- Cooley, J.W., P.A. Lewis and P.D. Welsh (1970): The Application of the Fast Fourier Transform Algorithm to the Estimation of Spectra and Cross-Spectra. J. of Sound Vib. 12, 339-352.
- Drinkow, R. (1972): A Solution to the Paired Gill Anemometer Response Function. JAM., 11, 76-80.
- Eloranta, E.W., J.M. King and J.A. Weinman (1975): The Determination of Wind Speeds in the Boundary Layer by Monostatic Lidar. JAM., 14, 1485-1489.
- Gentleman, W.M. and G. Sande (1966): Fast Fourier Transform - for Fun and Profit. AFIPS Fall Joint Com. Conf., 29, 563-578.
- Gossard, E.E. (1967): The Apparent Movement of Spectral Components in Fading Records of Ionospherically Reflected Radio Waves. J. of Geophys. Res., 72, 1563-1569.

- _____(1969): The Effects of Bandwidth on the Interpretation of the Cross Spectra of Wave Recordings from Spatially Separated Sites. J. of Geophys. Res., 74, 325-337.
- Izumi, Y. and M.L. Barad (1970): Wind Speeds as Measured by Cup and Sonic Anemometers and Influenced by Tower Structure. JAM, 9, 851-856.
- King, J.M. (1975): The Determination of Wind Speeds by Lidar. M.S. Thesis, University of Wisconsin-Madison.
- Kjelaas, A.G. and G.R. Ochs (1974): Study of Divergence in the Boundary Layer using Optical Propagation Techniques. JAM, 13, 242-248.
- Kunkel, K.K. (1978): Measurement of Upper Convective Boundary Layer Parameters by Means of Lidar. Ph.D. Thesis, University of Wisconsin, Madison.
- Lawrence, T.R., D.J. Wilson, C.E. Raven, I.P. Jones, R.M. Huffaker and J.A. Thomas (1972): A Laser Velocimeter for Remote Wind Sensing. Rev. of Sci. Inst., 43, 512-518.
- Leuthner, T.G. (1976): Remote Measurements of Wind Velocities by Monostatic Lidar. M.S. Thesis, University of Wisconsin, Madison.
- Marquardt, D. (1963): An Algorithm for the Least Squares Estimation of Nonlinear Models. J. of SIAM, 2, 431-441.

- Middleton, W.E. and A.F. Spilhaus (1953): Meteorological Instruments. University of Toronto Press. Toronto, 286 pp.
- Otnes, R.K. and L.D. Enochson (1972): Digital Time Series Analysis. John Wiley and Sons. New York, 476 pp.
- Panofsky, H.A. and G.W. Beier (1968): Some Applications of Statistics to Meteorology. The Pennsylvania State University Press, University Park, 224 pp.
- Pendergast, M.M. (1975): A Cautionary Note Concerning Aerodynamic Flying of Bivane Wind Direction Indicators. JAM, 14, 626-627.
- Rider, L.S. and M. Armendariz (1968): A Comparison of Simultaneous Wind Profiles Derived from Smooth and Rough-end Spheres. JAM, 7, 293-296.
- Rodgers, R.R. and H.G. Camnitz (1966): An Additional Note on Erratic Balloon Motions. JAM, 5, 370-373.
- Schaefer, J.T. and C.A. Doswell III (1978): The Inherent Position Errors in Double Theodolite Pibal Measurements. JAM, 17, 911-915.
- Sethuraman, S. and R.M. Brown (1976): A Comparison of Turbulence Measurements made by a Hot Film Probe, a Bivane and Directional Vane in the Atmospheric Surface Layer. JAM, 15, 138-144.

Wainstein, L.A. and V.D. Zubakov (1962): Extraction of Signals from Noise. Dover Publications, Inc., New York, 382 pp.

Welch, P.D. (1967): The Use of Fast Fourier Transforms for Estimation of Power Spectra: A Method Based on Time Averaging Over Short, Modified Periodograms. IEEE Trans. on Audio and Electroac., 15, 70-73.

Zuev, V.E., Yu. M. Vorenvodin, G.G. Matvienko and I.V. Sanokhvolov (1977): Investigation of Structure and Dynamics of Aerosol Inhomogeneities in the Ground Layer of the Atmosphere. Appl. Opt., 16, 2231-2235.